ABSTRACT

Title of Document: NONINVASIVE OPTICAL IMAGING TECHNIQUES AS A QUANTITATIVE ANALYSIS OF KAPOSI'S SARCOMA SKIN LESIONS

Abby Jeanne Vogel, Doctor of Philosophy, 2007

Directed By: Professor Yang Tao, Fischell Department of Bioengineering

The visible inspection and palpation of skin lesions have long been used to assess the course of cutaneous disease in individuals with Kaposi's sarcoma (KS). Assessing the KS lesions requires a highly trained evaluator and evaluations made by different observers or by the same observer at different times can be inconsistent. Since lesions can grow from slow to explosively fast, and be associated with mortality and morbidity, reliable assessment of the lesions is important.

Optical imaging techniques are quantitative methods that potentially offer a more objective means of assessing skin health that can supplement visual clinical observations. In this dissertation, the first paper describes using thermography and laser Doppler imaging (LDI) to monitor the temperature and vasculature, respectively, of KS lesions undergoing experimental therapy. Results showed that the median temperature elevation of lesions compared to the surrounding tissue was 1.1 ºC (range -0.68 to 3.43 ºC). In addition, 12 of the 16 lesions studied had increased

blood perfusion as assessed by LDI (median 66 arbitrary units (AU), range -44 to 451 AU).

The second paper describes the use of near-infrared (NIR) multi-spectral imaging to provide functional information about the lesions and surrounding tissue. Multi-spectral images were input to a mathematical optical skin model based on the absorption and scattering properties of skin, including the effects of melanin, blood, and oxygenated and deoxygenated hemoglobin. Functional information about the lesions before and after treatment with experimental therapies was determined.

The third paper describes Monte-Carlo simulations of tissue conducted to determine the detection limits of a typical multi-spectral imaging system. The results showed that biological information contained in a typical spectral image reflected a small volume of tissue situated vertically under each pixel from a depth less than 2-3 mm. The objects appearing on a spectral image reasonably reproduce the correct geometrical shape and size of underlying inclusions of pathological tissue.

Based on the three papers included in this dissertation, these three imaging techniques were found to be objective, easy to perform, and appear to be very sensitive in quantitatively assessing KS lesion progress upon administration of therapy.

NONINVASIVE IMAGING TECHNIQUES AS A QUANTITATIVE ANALYSIS OF KAPOSI'S SARCOMA SKIN LESIONS

By

Abby Jeanne Vogel

Dissertation submitted to the Faculty of the Graduate School of the
University of Maryland, College Park, in partial fulfillment
of the requirements for the degree of
Doctor of Philosophy
2007

Advisory Committee:
Professor Yang Tao, Chair
Adjunct Professor Amir Gandjbakhche
Professor Fredrick Wheaton
Professor Adel Shirmohammadi
Associate Professor Nam Sun Wang

Acknowledgements

I am extremely grateful to both of my advisors, Yang Tao at the University of Maryland (UMD) and Amir Gandjbakhche at the National Institutes of Health (NIH), for seeing my research potential and pushing me to attempt and complete my PhD degree. Without their motivation and guidance, I would never have earned my master's or PhD degrees. Working at the NIH to conduct my research allowed me to collaborate on this project with many intelligent scientists, including Robert Yarchoan of the National Cancer Institute, Randall Pursley of the Center for Information Technology, Stavros Demos of the Lawrence Livermore National Laboratory, and Tiziano Binzoni of the University of Geneva in Switzerland. I would also like to thank Karen Aleman and Kathleen Wyvill, who scheduled the weekly patient visits and collected the clinical examination data.

I want to express my appreciation to all of the members of my laboratory at the NIH for their constant suggestions and contributions to this work, including Franck Amyot, Victor Chernomordik, Israel Gannot, Moinuddin Hassan, David Hattery, Jason Riley, and Alex Small. I also want to thank the other members of my laboratory at UMD, including Xin Chen, Lu Jiang, Fenghua Jin, Hansong Jing, Lei Qin, Angela Vargas, and Bin Zhu, for their endless advice and friendship. I would also like to thank my other committee members, Adel Shirmohammadi, Nam Sun Wang, and Fredrick Wheaton, who have known me for several years now (Dr. Shirmohammadi and Dr. Wheaton since I joined the Department of Biological Resources Engineering after the fall of 1998 as an undergraduate) and have never wavered in their support of me.

Finally, I would like to extend my deepest gratitude to my parents, who have always believed in me and knew I could accomplish the goal of being the first PhD in my family. And to Jeff, who started dating me just one week after I decided to pursue my PhD, thanks for understanding how important earning this PhD was to me and for supporting me, even when the light at the end of the tunnel was dim and I thought I'd never graduate.

Table of Contents

List of Tables

List of Figures

List of Symbols

A	Absorbance
A_{dermis}	Attenuation of light intensity after passing through dermis
A_{epi}	Attenuation of light intensity after passing through epidermis
B	Stefan Boltzmann constant
c	Concentration of the chromophore
d	Pathlength or distance light travels
E	Emissivity
g	Anisotropy factor
$\bar{I}$	Average intensity
$I_{calibration}$	Calibration factor
I_{det}	Detected intensity
n	Refractive index
N	Number of photon packets
$N_{\lambda}^{\det ect}$	Total weight of photon packets that reach detector at end of simulation
$\overline{N}_{\lambda}^{\det ect}$	Mean pixel intensities between two regions
$N_{\lambda}^{\%}$	Number of photon packets that visit given pixel before reaching detector
r_{mean}	Mean radius
R	Spectral radiant excitance
Rc	Reflectance spectrum
R_o	Diffuse reflectivity
s	Step
$s_{\lambda}^{\max}$	Maximum surface
S	Scaling factor
t	Thickness of epidermis
T	Temperature
V_{blood}	Volume fraction of blood in tissue
V_{fat}	Volume fraction of fat
V_{Hbtot}	Volume fraction of erythrocytes
V_{water}	Volume fraction of water
V_{mel}	Volume fraction of melanin
V_{oxy}	Volume fraction of oxygenated hemoglobin
V_{rbc}	Volume fraction of hemoglobin in erythrocytes
W	Spectral radiant excitance
z_{max}	Maximum depth
γ	Volume fraction of hemoglobin in blood
$\Delta\overline{N}_{\lambda}^{\det ect}$	Percent difference in intensity between two regions
λ	Wavelength
μ	Ratio of absorption and reduced scattering coefficients
μ_a	Absorption coefficient

$\mu_a^{corneum}$	Absorption coefficient of stratum corneum
μ_a^{deoxy}	Absorption coefficient of deoxygenated hemoglobin
μ_a^{dermis}	Absorption coefficient of the dermis layer
μ_a^{epil}	Absorption coefficient of the epidermis layer
μ_a^{fat}	Absorption coefficient of fat
μ_a^{water}	Absorption coefficient of water
μ_a^{mel}	Absorption coefficient of melanin
μ_a^{oxy}	Absorption coefficient of oxygenated hemoglobin
μ_a^{skin}	Absorption coefficient of baseline skin
μ_s	Scattering coefficient
μ_s'	Reduced scattering coefficient
$\mu_s'^{hypodermmis}$	Hypodermis scattering coefficient
$\mu_s'^{mie}$	Mie scattering coefficient
$\mu_s'^{rayleigh}$	Rayleigh scattering coefficient

List of Abbreviations

ACTG	AIDS Clinical Treatment Group
AIDS	Acquired immunodeficiency syndrome
AU	Arbitrary units
bFGF	Basic fibroblast growth factor
C	Celsius
CCD	Charge-coupled device
CIE	Commission Internationale de l'Eclairage
cm	Centimeter
CPU	Central processing unit
CT	Computed tomography
FPA	Focal plane array
FWHM	Full width at half maximum
g	Gram
GHz	Gigahertz
HAART	Highly active anti-retroviral therapy
Hb	Deoxygenated hemoglobin
HbO_2	Oxygenated hemoglobin
Hct	Hematocrit
He-Ne	Helium-neon
HHV-8	Human herpesvirus-8
HIF	Hypoxia inducible factor
HIV	Human immunodeficiency virus
IL-12	Interleukin-12
in	Inch
IR	Infrared
K	Kelvin
kg	Kilogram
KS	Kaposi's sarcoma
KSHV	Kaposi's sarcoma associated herpesvirus
L	Liter
LDI	Laser Doppler imaging
m	Meter
MC	Monte-Carlo
mg	Milligram
min	Minutes
mm	Millimeter
MR	Magnetic resonance
MRI	Magnetic resonance imaging
NCI	National Cancer Institute
Nd:YAG	Neodymium-doped yttrium aluminium garnet ($Nd:Y_3Al_5O_{12}$)
ng	Nanogram
NICHD	National Institute of Child Health and Human Development
NIH	National Institutes of Health

NIR	Near-infrared
NIRS	Near-infrared spectroscopy
nm	Nanometer
OCT	Optical coherence tomography
p	Probability
PET	Positron emission tomography
ROI	Region of interest
SD	Standard deviation
SO_2	Oxygen saturation
UMD	University of Maryland
μm	Micrometer
US	Ultrasound
VEGF	Vascular endothelial growth factor
W	Watts
W	Weight

Chapter 1: Overall Introduction

An impressive array of imaging techniques, such as X-ray imaging, computed tomography, magnetic resonance imaging, ultrasound, and radioisotope imaging yield useful information, but there are important limitations on safety, resolution, cost, and lack or limited specificity to key chemicals necessary for functional tissue monitoring. The objectives of this research were to develop a means of optically and noninvasively quantifying the progress and/or change in Kaposi's sarcoma (KS) lesions while the clinical subjects underwent experimental therapies. Clinical progress of the lesions according to clinician assessment was documented, but was decided mainly from qualitative measurements. The clinical studies in this dissertation have shown therapy-induced changes in temperature, vasculature, tissue oxygenation, and tissue blood volume of individuals with KS lesions (Hassan, et al., 2004; Vogel, et al., 2007).

The goal of this collaboration between the University of Maryland (Bioimaging and Machine Vision Laboratory) and the National Institutes of Health, both the National Institute of Child Health and Human Development (NICHD) (Laboratory of Integrative and Medical Biophysics, Section on Biomedical Stochastic Physics) and the National Cancer Institute (NCI) (HIV and AIDS Malignancy Branch), was to quantitatively assess KS lesions before, during and after experimental drug therapies. The quantitative assessments were made using three noninvasive techniques: thermography, laser Doppler imaging (LDI), and near-infrared (NIR) multi-spectral imaging. Clinical trials were approved by the NIH and UMD. With these three imaging techniques, temperature, vasculature, oxygenated hemoglobin

(HbO_2), and blood volume could be quantified inside the lesion and in the surrounding tissue and tracked during treatment.

This dissertation is organized into the following chapters. Chapter 2 details the overall objectives of this dissertation research and Chapter 3 provides a detailed introduction and literature review. Three journal articles are presented in Chapters 4, 5, and 6. The first paper describes the use of thermography and LDI to study KS lesions undergoing experimental therapy. The second paper describes the design of a NIR multi-spectral imaging system and a reconstruction algorithm used to study functional characteristics of KS lesions. The third paper describes Monte-Carlo simulations of tissue conducted to determine the detection limits of the multi-spectral imaging system. Chapter 7 follows with overall conclusions and Chapter 8 describes suggestions for future studies.

Chapter 2: Overall Objectives

The major goal of this research was to quantitatively analyze the changes in tissue vasculature of individuals with KS using noninvasive imaging techniques. This research utilized three noninvasive imaging techniques: thermography, LDI, and NIR multi-spectral imaging. Each imaging technique monitored a different functional aspect of the skin and vasculature. Thermography measured the temperature, LDI monitored the blood flow, and multi-spectral imaging monitored changes in HbO_2 and blood volume in the lesion and normal skin while the patient received experimental therapy. The specific objectives of Chapters 4, 5, and 6 were to:

1. Determine with thermography and LDI if the temperature and blood flux differences between the lesion and surrounding skin changed during experimental therapy.
2. Determine if multi-spectral imaging could be used to quantitatively analyze the functional characteristics of tissue during experimental drug therapy and investigate progression of disease.
3. Investigate the use of the Monte Carlo method to simulate a virtual spectral imager and study the behavior of the photons at different wavelengths traveling inside human skin tissue and the possible influence of this behavior on the resulting spectral images.

Thermography, LDI, and multi-spectral imaging techniques have the potential to establish quantitative methods to assess KS lesions undergoing therapy and to teach clinicians about the effects of such therapy on the vascularity of the lesions. Moreover, such approaches can be used to provide early markers for tumor responses

and to learn about the pathophysiology of the disease and its changes in response to treatment. Ultimately, quantitative imaging methods can be applied to other tumors or lesions involving the skin or other easily accessible tissues.

Chapter 3: Review of Literature

This chapter first provides background information on the structure of skin, including the epidermis and dermis layers, followed by a description of KS.

Sections 3.3 and 3.4 describe thermography and LDI imaging, respectively. Since the major portion of this dissertation is focused on the multi-spectral imaging technique, details describing this technique are broken down into several subtopics in Sections 3.5-3.9.

First, Section 3.5 describes applications of NIR spectroscopy in medicine. Then, since analyzing a set of multi-spectral images requires a mathematical skin model, Section 3.6 describes previously developed models and Section 3.7 discusses the absorption and scattering properties necessary for the models. Sections 3.8 and 3.9 describe how light travels through the epidermis and dermis layers of skin, respectively. These sections also detail what analytes are present in each layer and what factors must be taken into consideration in the model.

3.1 Skin Structure

Skin is the flexible tissue enclosing the body of vertebrate animals while providing vital protective and metabolic functions. The skin provides a barrier against invasion by outside organisms, protects underlying tissues and organs from abrasion and other injury, and shields the body from the dangerous ultraviolet rays in sunlight. It also waterproofs the body, preventing excessive loss or gain of bodily moisture.

At the human/environment interface, heat is carried away from the body by conduction, convection, radiation, and evaporation. The human thermoregulatory

system maintains a reasonably constant body temperature against a wide range of environmental conditions. This is possible because the body's numerous sweat glands excrete waste products along with salty moisture; its fat cells act as insulation against cold; and when the body overheats, its extensive small blood vessels carry warm blood near the surface to be cooled.

The skin is lubricated by its own oil glands, which keep both the outside layer of the epidermis and the hair from drying to brittleness. The body uses several physiological processes to increase or decrease heat transfer with the environment. The mechanism controlling thermal emission and dermal microcirculation is driven by the sympathetic nervous system. In the presence of a disease affecting the local thermoregulatory system, there may be an altered sympathetic function and a change in the local metabolic rate (Merla, 2002). The structure of skin, shown in Figure 1, contains two main layers of cells: a thin outer layer, the epidermis; and a thicker inner layer, the dermis. The dermis is bonded to a subcutaneous fat layer which may be several centimeters thick (Archambeau, et al., 1995). Optically, the human skin is simply described in terms of two different absorbing and scattering layers on top of a nearly totally reflecting collagen layer in the dermis (Anderson and Parrish, 1981; Dawson, et al., 1980; Wan, et al., 1981).

3.1.1 Epidermis

The epidermis ranges from 27-300 microns thick (Anderson and Parrish, 1981; Archambeau, et al., 1995; Meglinsky and Matcher, 2001) and is composed of five layers: stratum corneum, stratum basale, stratum spinosum, stratum granulosum, and stratum lucidum. The epidermis is shown in Figure 1 on the surface of the skin.

The outermost epidermis skin layer, the stratum corneum, is about 10-20 microns thick (Anderson and Parrish, 1981; Meglinsky and Matcher, 2001). It's composed mainly of dead cells, called corneocytes, embedded in a particular lipid matrix.

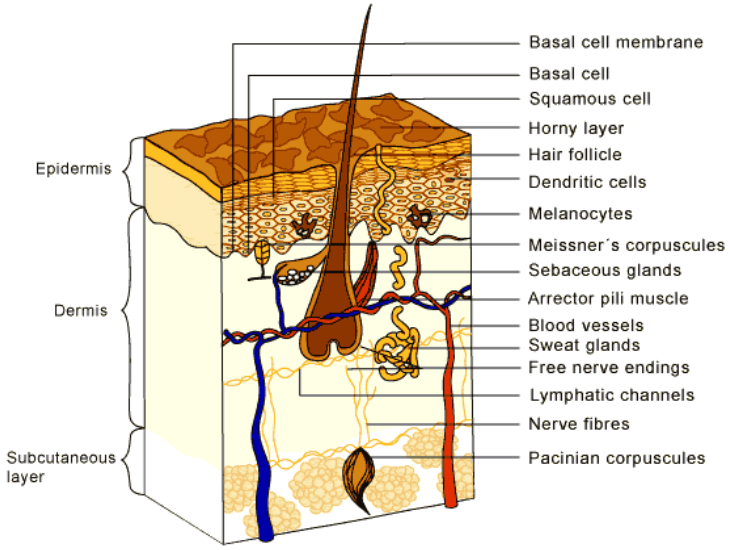

Figure 1. Structure of epidermis, dermis, and subcutaneous layers of the skin (http://skincancer.dermis.net/content/e01geninfo/e7/index_eng.html).

The outer stratum corneum, which mainly induces diffuse forward scattering, influences total skin reflectance approximately 8%, which for all practical purposes is negligible (Anderson and Parrish, 1981; Wan, et al., 1981). All light penetrating the stratum corneum is heavily absorbed by the epidermal melanin. The stratum corneum is equally thick in African and European skin (Freeman, et al., 1962; Thomson, 1955). However, Weigand et al. demonstrated that the stratum corneum in African skin contains more cell layers, but weighs the same as European skin (Weigand, et al., 1974). This may be because the lipid content of the stratum corneum is higher for black persons (Reinertson and Wheatley, 1959). Despite structural differences in the stratum corneum, the total reflectance of light is between 4-7% for both blacks and whites (Anderson and Parrish, 1981). The stratum corneum plays an important role as

a barrier between the environment and the body because it retains moisture in skin. The water content in the stratum corneum is not uniform; however, skin becomes more hydrated at deeper sites.

The epidermis has no blood vessels, but does contain blood cells, keratinocytes, melanocytes, dendritic cells, and basal cells. Circulating blood cells appear as either numerous small disks of diameter 5-9 microns or occasional large ovals of size 9-18 microns (Rajadhyaksha, et al., 1995). From their relative shapes, sizes, and concentrations, cells are erythrocytes or leukocytes. Other features include bright spiral- or crescent-shaped substructures inside nuclei, collagen fibers surrounding the capillaries, sweat ducts spiraling down into the dermis, and hair follicles.

Along the internal surface of the epidermis, keratinocytes are stacked on top of each other, forming sublayers. The keratinocytes develop at the bottom and rise to the top, where they flatten and overlap to form a tough membrane, and gradually shed as calluses or collections of dead skin. Melanocytes, located in the lower basal cell layer of the epidermis, produce a dark pigment called melanin which contributes to skin color and provides ultraviolet protection. Dendritic (Langerhans) cells are involved in the epidermal immune system. They engulf foreign material that invades the epidermis and migrate out of the skin to stimulate an immune response. Basal cells are found at the bottom of the epidermis.

Cell proliferation occurs in the basal cell monolayer with a generation time of 2.6 days. About 4% of the cells move into and out of the layer daily, maintaining constant population densities (Archambeau, et al., 1995). The layers of the epidermis

work together to continually rebuild the surface of the skin from within while maintaining the skin's epidermal strength.

The epidermis propagates and absorbs light. The absorption property comes mostly from a natural chromophore called melanin. Melanin is produced by cells called melanocytes occurring in the stratum basale and found in membranous particles called melanosomes. Melanosomes are secreted by melanocytes and into adjacent keratiepidermis nocytes via dendritic processes. The keratinocytes containing the melanin-carrying melanosomes move up through the epidermal layers as part of the constant regeneration process. Thus, melanin is formed in the lower layers of the skin, attaches to the keratinocytes in the form of melanosomes, and slowly moves to the outer layers of skin until it reaches the stratum corneum (Angelopoulou, 2001). Melanosomes have relatively high refractive indices (1.55–1.65) compared to the surrounding skin tissue (1.35–1.4) and are therefore important epidermal scatterers.

3.1.2 Dermis

The underlying dermis, much thicker than the epidermis, consists of connective tissues that contain embedded blood vessels, nerve endings, sebaceous glands, collagen, hair follicles, sweat glands, and fat cells (Figure 1). The dermis is 0.6-3 mm thick where the upper 350 micron portion is the papillary layer, which contains microvessels that supply the epidermis, and the lower layer is the reticular dermis (Anderson and Parrish, 1981; Meglinsky and Matcher, 2001). These layers are primarily composed of dense, irregular connective tissue with nerves and blood vessels (smaller ones in the papillary and larger ones in the reticular dermis).

The vascular supply to the dermis is largely from segmental arteries, each of which supplies a relatively small area of the epidermis with nutrients. The volume fraction of blood in tissue can vary, but typically range from 0.2-7% (Jacques, 1996). The fluence rate of blood decreases with depth, following an almost linear pattern in the dermis (Van Gemert, et al., 1989). The dermal vasculature includes arteries and veins from the subcutaneous layer that pass through the dermis with minimal branching. Tufts containing arterioles, venules, and capillaries extend through the papillary dermis up to the epidermal basal lamina. These vessels are contained in a loose connective tissue (Archambeau, et al., 1985). They exist as separate folded and coiled geographically isolated tufts, or bunches, with no interconnection to adjacent tufts except by arteries and veins (Archambeau, et al., 1995). Since the human skin has a rich blood supply, it has remarkable self-healing properties, particularly when only the epidermis is damaged. Deeper wounds, penetrating to the underlying tissue, heal by scar formation.

Nerve endings respond to various stimuli, including contact, heat, and cold. Meissner's corpuscle is effective in detecting light touch and soft, fleeting movements. Pacinian corpuscles function as receptors for deep pressure and vibration. Response to cold activates the erector muscles, causing hair or fur to stand erect. From the outer surface of the dermis extend numerous projections (papillae) that fit into pits on the inner surface of the epidermis so that the two layers are firmly locked together.

Sebaceous (oil) glands are small, sacculated organs that secrete sebum. This oily substance is a natural moisturizer that conditions the hair and skin. Sebaceous

glands are found all over the body, but they are more numerous in the scalp area and around the forehead, chin, cheeks, and nose.

The dermis tissues are composed largely of collagen fibers, approximately 75% by dry weight (Hopewell, 1990). Collagen is responsible for the skin's pliability and mechanical resistance and is also involved in the regulation of the body temperature.

3.2 Kaposi's Sarcoma

KS represents a useful model to study anti-angiogenesis approaches and the imaging of such therapies (Little, et al., 2000; Yarchoan, 1999a). KS is a frequent cause of morbidity and mortality among individuals infected with human immunodeficiency virus (HIV) (Beral, et al., 1990). Figure 2 shows a photograph of a typical KS lesion. KS lesions may be red, purple, brown, or black, and are usually raised above the skin. Growth can range from very slow to explosively fast, and be associated with significant mortality and morbidity.

Figure 2. Photograph of a typical KS lesion.

KS lesions are characterized pathologically by spindle cells and vascular slits (Antman and Chang, 2000). KS is caused in part by a gammaherpesvirus called

Kaposi's sarcoma associated herpesvirus (KSHV) or human herpesvirus-8 (HHV-8) (Chang, et al., 1994). This virus encodes for several factors with angiogenic activity, and KS spindle cells have been shown to produce and respond to a number of proangiogenic factors including basic fibroblast growth factor (bFGF) and vascular endothelial growth factor (VEGF) (Boshoff, et al., 1997; Ensoli, et al., 1992; Moore, et al., 1996). Also, KSHV induces a proangiogenic state and upregulates VEGF production in part through activating hypoxia inducible factor (HIF) (Bais, et al., 1998; Sodhi, et al., 2000). Cutaneous KS lesions are easily accessible for noninvasive techniques that involve imaging of tumor vasculature, and they may thus represent a model tumor in which to assess certain parameters of angiogenesis.

3.3 Thermography

3.3.1 Thermal Energy

Thermography is the use of an infrared camera to visualize and measure thermal energy emitted from an object. Thermal, or infrared (IR) energy, is light that is not visible because its wavelength is too long to be detected by the human eye. Under infrared light, everything with a temperature above absolute zero emits heat. The higher the object's temperature, the greater the IR radiation emitted (FLIR, 2002).

The amount of radiated power is proportional to the body's temperature, raised to the fourth power and determined by the following equation (Kelch, 1998):

$$R = E * B * T^4 \qquad (1)$$

where R is the spectral radiant excitance [Watt * cm^{-2}], E is the emissivity, B is the Stefan Boltzmann constant (5.67×10^{-12} Watt $cm^{-2} K^{-4}$), and T is the temperature in

Kelvin. Many scanners and cameras have been designed and produced to visualize light in the IR range.

3.3.2 Thermal Camera

A thermal camera is a noninvasive device that detects IR energy and converts it to an electronic signal, which is then processed to produce a thermal image on a video monitor where temperature calculations can be performed (FLIR, 2002). Heat sensed by an IR camera can be very precisely quantified. IR thermal imagers capture a portion of the radiated energy and are calibrated to indicate specific temperatures. Thermal cameras are popular because they are completely non-contact, quantify temperature precisely, acquire images quickly (resolution and speed independent), and allow for a large imaging area.

There are currently two types of focal plane array (FPA) imagers: cooled and uncooled. Cooled FPA systems operate in the 3-5 micron or NIR range and generally provide excellent sensitivity. The newest FPA imaging systems use uncooled detectors. Unlike previous IR systems that sensed photons, these microbolometer systems operate by sensing changes in electrical resistance across the detector, produce high-resolution images, but do not require cryogenic cooling systems. Currently, all microbolometers operate in the 8-12 micron or mid-IR range. The increased resolution found on FPA microbolometer systems enables users to discern minute temperature variations and provides highly accurate temperature readings (FLIR, 2002). Commercial infrared imagers are not manufactured in the 5-8 micron range due to atmospheric absorption of infrared energy at these wavelengths.

3.3.3 Thermal Images

Thermography graphically depicts temperature gradients over a given body surface area at a given time. It has the ability to study biological thermoregulatory abnormalities that directly or indirectly influence skin temperature (Anbar, 1998; Head and Elliott, 2002; Maxwell-Cade, 1968; Usuki, et al., 1998). A spatial map of temperatures called a thermograph or thermogram is created, as shown in Figure 3. Regions of higher temperature are seen as dark red and white shades, while regions of cooler temperatures appear as blue and black.

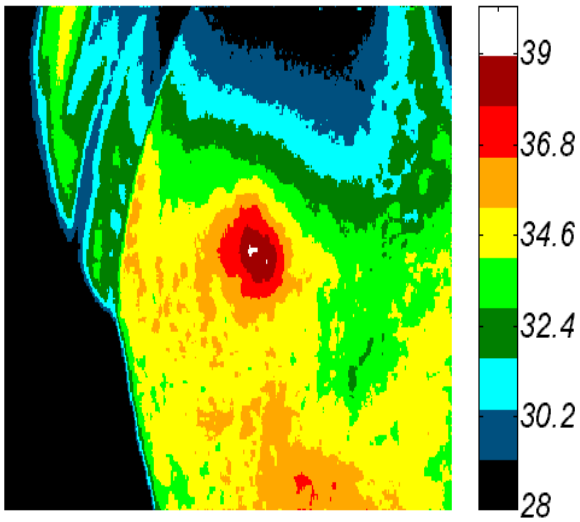

Figure 3. Thermogram showing temperature in degrees Celsius of left shoulder and back of individual in Figure 2 with KS lesion.

Thermography provides an integrated thermal signature that combines deep and surface sources and in general can be related to increased blood flow associated with increased metabolic activity (Bornmyr, et al., 1997; Draper and Boag, 1971; Love, 1980; Stoner, et al., 1991). Skin temperature is only an indirect measure of skin blood flow (Love, 1980). In fact, the superficial thermal signature of skin is related to metabolism and vascularization within the underlying tissues. It may therefore change

significantly as a result of pathological processes. Temperature measurement is the most widely used technique for the evaluation of skin circulation (Usuki, et al., 1998). Thus, this approach is best used in conjunction with other imaging techniques. Since radiation has been shown to cause vascular changes in the skin, thermography should be evaluated as a noninvasive analysis tool.

3.4 Laser Doppler Imaging

LDI can more directly measure the blood perfusion of small blood vessels in tissue, which generally increases as the blood supply increases during angiogenesis (Rivard, et al., 1999; Sorensen, et al., 1996). By combining thermography with LDI, it may be possible to differentiate the near surface sources from the deeper infrared sources, thus providing a useful means to assess local changes in tissue vascularization. The tissue sampled is typically 1 mm thick, capillary diameters are 10 microns, and the velocity spectrum measurement is typically 0.01 to 10 mm/s. The theory of the Doppler technique, shown in Figure 4, begins when low power light from a monochromatic stable laser, such as a 5-mW Helium-Neon (He-Ne) laser, incident on tissue, is scattered by moving red blood cells. LDI measures the Doppler shift due to the movement of red blood cells and produces a 2D image of tissue blood perfusion (Figure 5). The term commonly used to describe blood flow measured by the laser Doppler technique is flux. Flux is expressed in arbitrary perfusion units and is a quantity proportional to the product of the average speed of the blood cells and their number concentration, often referred to as blood volume. Figure 5 shows that highly vascular areas can be detected from the surroundings. It can register flow in a variety of vessels including arterioles, capillaries, and venules.

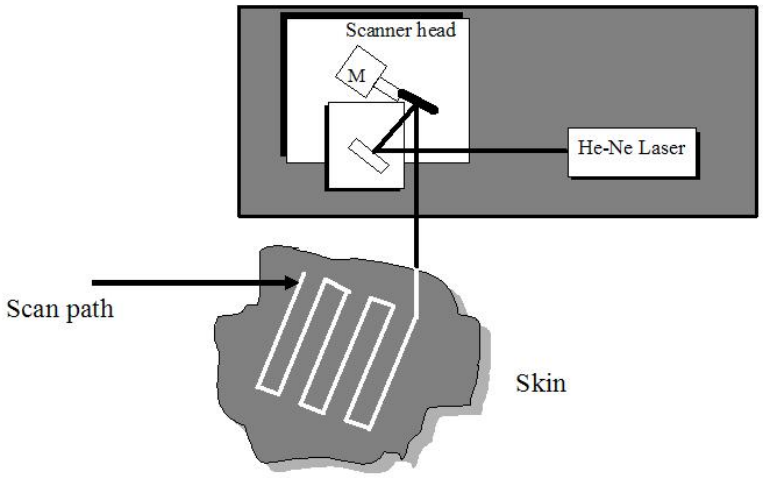

Figure 4. Laser Doppler imaging technique. The He-Ne laser scans in a raster pattern over the skin measuring the velocity and concentration of red blood cells.

Laser Doppler imaging visualizes diseased states that exhibit highly vascular areas, such as tumors. Regions of interest can be defined and statistical data can be calculated and recorded.

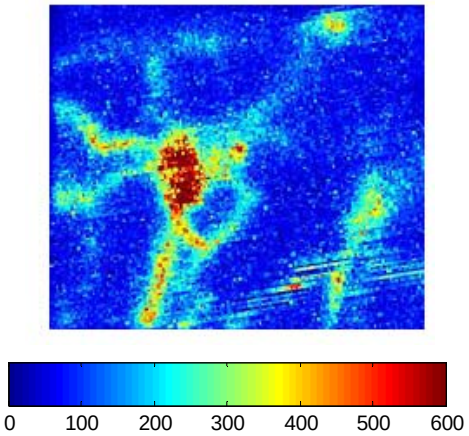

Figure 5. Laser Doppler image showing vasculature. Note that the color bar is in arbitrary perfusion units.

3.5 Reflectance Spectroscopy

Optical imaging modalities are being pursued to achieve diagnostic ability through the exploitation of the spectroscopic characteristics of tissues (Hattery, 2002). By changing the wavelength of light, one can obtain multiple spectral images that

highlight various molecular components. In addition, light interacts with biological tissues in a number of different ways providing different means to probe the body. However, because of scattering and absorption, quantification has been limited to surface imaging. Optical reflectance imaging of tissues, a novel concept in diagnostic medicine and the basis of Chapters 5 and 6, can be used to determine the variation in tissue physiology.

NIR spectroscopy (NIRS) tells what's going on at the body's surface and below, since light penetrates tissue to a certain extent. *In vivo* spectral reflectance measurements of human skin have been performed since 1939, but the early data were not analyzed in terms of chromophore content until 1951 (Andersen and Bjerring, 1990; Goldzieher, et al., 1951). In contrast to *in vitro* absorbance measurements in chemistry, *in vivo* reflectance spectroscopic data analysis is very complex (Anderson and Parrish, 1981). NIRS interrogates blood in the capillaries, arterioles, and venules of tissue and enables direct and noninvasive measurements of the tissue oxygen saturation by examining absorption differences in the spectra of oxygen carriers, such as oxygenated hemoglobin (HbO_2), deoxygenated hemoglobin (Hb), myoglobin, and cytochrome aa3 (Taylor and Simonson, 1996). The concentrations of these analytes in tissue may be used to diagnose disease and to monitor changes in various conditions (Kollias, et al., 1995; Shah, et al., 2001; Wagnieres, et al., 1997). Assessing these analytes is complicated by other pigments in the skin, i.e. melanin and hemosiderin, but it is possible to correct for such pigments with NIRS. Several researchers have used NIRS to study physiological changes in tissue.

3.5.1 Measuring Tissue Oxygenation

For years, light has been used as an indicator of oxygenation. The ear oximeter, devised by Millikan in 1942, was the first successful clinical device to determine oxygenation. The differential absorption of light by HbO_2 and Hb forms the basis of pulse oximetry and has been exploited clinically for some time. However, pulse oximetry has been primarily concerned with systemic blood oxygenation and not with local oxygenation in cutaneous tissues. Reports on a variety of human and animal tissues, both *in vivo* and *in vitro*, have been published (Zonios, et al., 1999).

The NIRS method is not limited to measurements of blood oxygenation in arteries (e.g. pulse oximetry) or in veins, but interrogates blood in the entire vascular compartment, including capillaries, arterioles, and venules, i.e. the vascular bed. NIRS was introduced as a technique to determine the degree of tissue oxygenation several decades ago (Jobsis, 1977). NIRS is also being more aggressively investigated and now marketed clinically as a noninvasive means to assess tissue oxygenation in trauma patients at the end organ level (Ward, et al., 2006).

New and advanced methods, including pulsed reflectance spectroscopy, have made it possible to estimate oxygen saturation of hemoglobin transcutaneously in specific body areas (Feather, et al., 1988). HbO_2 saturation in subcutaneous rat mammary tumors was measured using NIRS *in vivo* and in rapidly frozen sections from the same tumors using cryospectrophotometry, which reported oxygen saturation in individual blood vessels to depths of 4 mm from the tissue surface. Sensitivity and specificity analysis suggested that NIRS may identify clinically

relevant hypoxia, even when its spatial extent was below the resolution limit of the NIRS technique (Conover, et al., 2000).

Laufer et al. used pulsed photoacoustic spectroscopy to measure blood oxygen saturation *in vitro* (Laufer, et al., 2005). An optical parametric oscillator laser system provided nanosecond excitation pulses over the wavelength range 740–1040 nm that were used to generate photoacoustic signals in a cuvette through which a saline suspension of red blood cells was circulated. The signal amplitude and effective attenuation coefficient were extracted from the photoacoustic signals as a function of wavelength to provide photoacoustic spectra of the blood. From these, the relative concentrations of HbO_2 and Hb, and therefore blood oxygen saturation (SO_2), were determined using forward models of the absorbed energy distribution based on diffusion theory. A standard linear model of the dependence of absorbance on the concentration of chromophores was also used to calculate SO_2 from the signal amplitude spectra. The diffusion approximation model was shown to produce the highest accuracy in blood SO_2. Payette et al. used NIRS and laser Doppler imaging to study the oxygenation of skin flaps (Payette, et al., 2005).

Semi-empirical models have been used to measure blood content and HbO_2 saturation in rat gastric mucosa (Sato, et al., 1979) and rat pancreas (Knoefel, et al., 1996). Differences in the diffuse reflectance of rat brain were characterized empirically (Ikeda and Matsushita, 1980), and empirical analysis was also employed to study human tissues *in vivo*, such as skin (Marchesini, et al., 1991), bladder (Mourant, et al., 1995), and colon (Ge, et al., 1998; Mourant, et al., 1996). The results

confirm that tissue reflectance provides valuable information, but the qualitative nature of the analyses limits the information obtained.

Quantitative results have been obtained in blood oximetry (Schmitt, 1991; Takatani and Ling, 1994) and in the study of the optical properties of various animal tissues such as rat prostrate (Arnfield, et al., 1988), chicken breast (Kienle, et al., 1996), and canine gut (Zonios, et al., 1996). However, these models are mathematically complicated, making difficult the inversion of the measured spectra, which is needed to obtain the tissue optical parameters (Zonios, et al., 1999).

3.5.2 Measuring Tissue Blood Volume

Port-wine stains, a congenital birthmark consisting of an abnormal density of blood vessels in the upper dermis, have also been studied with NIR spectroscopy (Svaasand, et al., 1995). The enlarged blood volume gives the lesion a red to purple color. The aim of treatments is to destroy the vessels to the extent necessary for obtaining normal skin coloration. NIRS can follow port-wine stains through laser treatment.

NIRS has also been applied to study the pathophysiology of skeletal muscle metabolism during exercise (Colier, et al., 1995; Comerota, et al., 2003), in patients with diabetes or compartmental syndrome (Giannotti, et al., 2000; Scheuermann-Freestone, et al., 2003), and to monitor perfusion during carotid endarterectomy (Kragsterman, et al., 2004; Mille, et al., 2004; Williams, et al., 1996).

Ryatt et al. (1983) used reflectance spectrophotometry to obtain indices of hemoglobin and melanin content of psoriatic lesions and adjacent clinically normal

skin. Results showed that hemoglobin in the lesion was 2.8 times greater than that of adjacent uninvolved skin (Ryatt, et al., 1983).

3.5.3 Measuring Tissue Moisture

Although the condition of skin can be felt to some extent, it is somewhat difficult to measure the moisture content quantitatively. A quantitative measurement of skin tissue water content is required in a wide variety of fields such as evaluating the effects of cosmetic products and medical diagnostics. Many researchers have developed instrumentation and techniques for infrared spectroscopic imaging to visualize skin hemodynamics and tissue water content to test tissue viability of skin flaps (Attas, et al., 2001; Stranc, et al., 1998). Attas et al. (2001) mounted a liquid-crystal tunable filter on the front of the objective lens of an IR-sensitive charge-coupled device digital camera. Sets of narrow-band images of skin were acquired *in vivo* at wavelength intervals of 10 nm from 650 to 1050 nm.

Mansfield et al. used NIRS to diagnose acute maxillary rhinosinusitis (Mansfield, et al., 2005) and Canvin et al. used NIRS to characterize the synovium of the small finger joints in both early and late rheumatoid arthritis. The study demonstrated relationships between the specific sources of spectral variation and joint tenderness or swelling as well as radiographic damage. Further use of multivariate analysis allowed recognition of the spectral patterns seen in early disease versus late rheumatoid arthritis and correct classification of over 74% of the joints (Canvin, et al., 2003).

3.6 Mathematical Optical Skin Models

The rosy glow of someone's cheeks and the tan on someone's arms reflect the presence of colored chemicals in the skin (hemoglobin and melanin, respectively). Light spectroscopic methods are critical to advances in molecular characterization of disease processes. Chapters 5 and 6 in this dissertation require a mathematical optical skin model to analyze the NIR spectroscopic images. Researchers have created multiple layer models that include different chromophores in each layer allowing for a reconstructed spatial map of those constituents. The construction of a simplified optical model allows the introduction of pigment indexes as a measure for pigment content in the skin (Dawson, et al., 1980), resulting in widespread use of spectral reflectance for *in vivo* measurements (Ryatt, et al., 1983). Studies of skin inflammation, effects of dermatological treatment modalities, and skin physiology have now become objective because of modern methods, but the intriguing optical properties of human skin make data analysis very complicated (Ryatt, et al., 1983). Models range from simple ones with two layers (i.e. epidermis and dermis layers) to complex ones with up to seven layers.

A three-layer model of epidermis, papillary upper dermis, and reticular dermis was used to study the independent effects of 13 parameters' independent effects on the reflectance spectra (Zhang, et al., 2005). A three-layer optical skin model was proposed to perform computerized multiple regression analysis of *in vivo* skin reflectance measurements (Andersen and Bjerring, 1990).

More complicated models include multiple layers, each layer containing different concentrations of blood and pigments. One example is a five-layer skin

model: epidermis, capillary blood plexus, dermis, deep blood plexus, and hypodermis (Douven and Lucassen, 2000). The dermis layer consisted of three distinct layers that could contain different concentrations of blood. The first layer of the dermis accounted for the superficial blood plexus and the capillary loops located in the upper dermis, and the third layer of the dermis accounted for the deep blood plexus in the lower dermis. To account for the irregular shape of the epidermal-dermal interface, a small concentration of blood was taken into account for the bloodless epidermis. Other researchers introduced calibration factors to simplify homogeneously distributed blood (Douven and Lucassen, 2000). Since blood is discretely distributed in vessels, there are consequences for the effective absorption of light. The effective absorption of blood is reduced when the penetration depth of light in blood becomes small compared to the vessel radius, when blood in the center of the vessel does not contribute to absorption. Douven and Lucassen (2000) used Verkruysse's correction factor that depended on the product of the blood absorption coefficient and vessel radius to characterize chromophore concentrations in port-wine stains and highly pigmented human skin.

A five-layer model of the skin was used for numerical simulations (Sinichkin, et al., 1996). The layers included the epidermis, papillary derma, upper vessel plexus, reticular derma, and deep vessel plexus. Other researchers extended the simple epidermis and dermis model by adding a layer of oil on the outside of the skin (Ng and Li, 2001). Another researcher extended previous work (Stamnes and Conklin, 1984) to model a skin layer bounded by rough surfaces (Stam, 2001).

A new seven-layer bio-optical skin model was developed and computations were carried out with rigorous radiative transfer theory (Nielsen, et al., 2004). It was found that the observed reflectance could be simulated if the scattering from melanosomes was included in the bio-optical skin model and the different size distributions of melanosomes of lightly and darkly pigmented skin were taken into account. To focus on the importance of the melanosome depth distribution, Nielson et al. (2004) have simulated the light distribution in and above the skin. In these simulations, the size and depth distribution of melanosomes varied, but the volume concentration of melanosomes in the epidermis and all other input parameters were fixed.

A tissue model of complexity sufficient to approximate mammalian skin tissue with pulsatile blood flow requires multiple layers with unique optical properties, reflecting the heterogeneous distribution of blood in tissue. A four-layer tissue model was used to study laser dosimetry incorporated a layer representing a blood plexus (van Gemert and Henning, 1981), but an analytical solution was not published. Another researcher employed Monte Carlo simulations of light traveling through a homogeneous, single-layer tissue model to demonstrate the importance of light scattering in understanding reflectance pulse oximetry (Graaff, et al., 1996).

3.7 Absorption and Scattering

In any optical skin model, each layer contains major chromophores that determine absorption in the corresponding layer and the layers together determine the total reflectance of the skin. When light interacts with a medium such as tissue, some of it is reflected from the surface, some absorbed, some scattered within the tissue,

and some transmitted through to the other side (Figure 6). All of these interactions can provide information about the medium. The sum of the light intensities reflected, absorbed, scattered, and transmitted equals the total light intensity impinging on the medium. What is seen and measured is the light returning from the surface of the tissue back to a detector (Firbank, et al., 1995).

The extent to which light energy is absorbed by each of the chromophores in the tissue, in particular by HbO_2, Hb, and water, is described by the Beer-Lambert law:

$$A(\lambda) = \sum_{i=1}^{N} a(\lambda_i) dc_i \qquad (2)$$

where the overall absorbance at wavelength λ, $A(\lambda)$, is the sum of the absorbances of each of the N chromophores present. For each chromophore i, the absorbance is the product of its absorptivity at wavelength λ, $a(\lambda_i)$, times the path length, or the distance the light travels, d, times the concentration, c_i, of the chromophore.

Since some of the light penetrates the tissue, information about its absorption and scattering by the tissue at different wavelengths is also obtained as part of what is normally considered reflected light. In other words, the reflectance measured from the surface has contributions from singly scattered (reflected) photons at or near the surface of the tissue, as well as from photons that have traveled through a significant volume of the tissue via a series of scattering events. This spectral information can be obtained for each location in the tissue.

Within any skin layer, 93-96% of the incident radiation not returned by regular reflectance may be absorbed or scattered (Anderson and Parrish, 1981). Scattering is the form of interaction of light with a medium where only the light's

direction of travel is changed. Lucas demonstrated the presence of epidermal scattering in skin in 1931 by placing a sample of epidermis in front of the entrance slit of a monochromator, thereby creating a detector with a very limited aperture, and in this way measured direct transmission (Lucas, 1931).

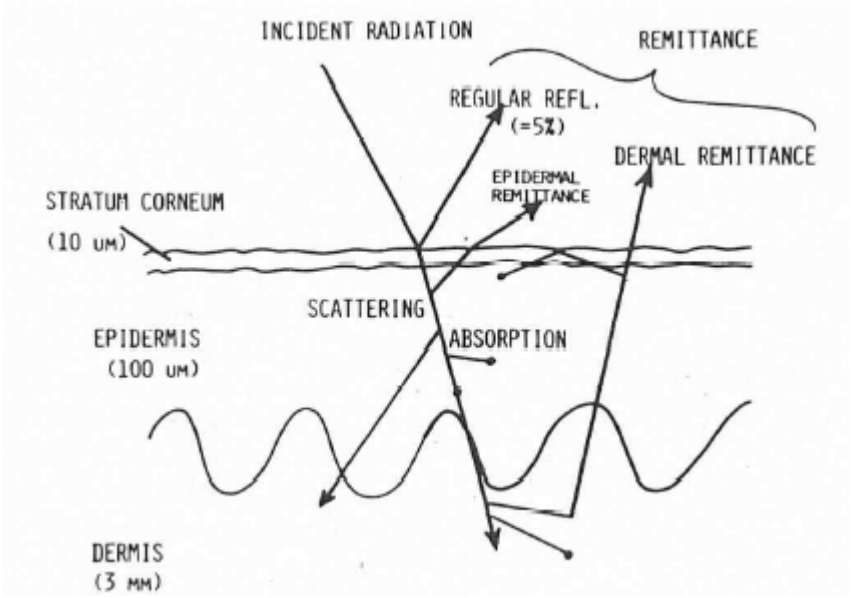

Figure 6. Schematic diagram of optical pathways in skin (Anderson and Parrish, 1981).

The degree of scattering is wavelength dependent and is also dependent on the size distribution and refractive indices of the scattering particles constituting the medium (Arnfield, et al., 1988). Candidates for scattering centers in mammalian cells are the cell itself, the nucleus, other organelles, and structures within organelles. Mammalian cells are typically of the order of 10–30 μm in diameter, with nuclei on the order of 3–10 μm in diameter (Mourant, et al., 1998). Mitochondria are approximately 1–4 μm in length and approximately 0.3–0.7 μm in diameter. Lysosomes and peroxisomes are roughly spherical in shape and approximately 0.2–0.5 μm in diameter. Other organelles from which light may scatter are the Golgi apparatus and the endoplasmic reticulum, both of which have complicated shapes

containing a large proportion of lipid membranes. To address the issue of what cell features are responsible for light scattering, the wavelength dependence of the reduced scattering coefficient, μ_s', must be measured.

For molecules or small particles with dimensions less than roughly 1/10 of the light wavelength, scattering is generally weak, nearly isotropic (equally distributed spatially) and polarized, and varies inversely with the fourth power of wavelength – this is called Rayleigh scattering (Anderson and Parrish, 1981; Jacques, 1998). For particles with dimensions on the same order as the wavelength, scattering is much stronger, more forward-directed, and, while varying inversely with wavelength, is not such a strong inverse function. When the particle size greatly exceeds the wavelength, scattering is again diminished and becomes highly forward-directed – known as Mie scattering (Kerker, 1969). Within the skin, all of these general types of scattering occur, but quantitatively, scattering by structures with dimensions on the order of optical wavelengths or somewhat larger (Mie) must dominate over Rayleigh scattering.

In tissue, the probability of a given photon being scattered varies gradually as a function of wavelength, so a linear scattering approximation is valid over limited ranges in the NIR region (Schmitt and Kumar, 1998). Multiple scattering events result in a complex pattern of photon flux in tissue. It is believed that the difference in the scattering coefficient between the epidermis and dermis layers of skin is not large, although there actually is some (Jacques, 1996; Van Gemert, et al., 1989). Experimental evidence supports the hypothesis that light scattering in tissue is anisotropic with significant forward scattering. Bruls and van der Leun (Bruls and

van der Leun, 1984) demonstrated forward-peaked scattering functions for human stratum corneum and epidermis at ultraviolet and visible wavelengths.

The reduced scattering coefficient depends on the wavelength of light. In the NIR region, the absorption mean free path is much longer (on the order of 10-100 microns) than the scattering mean free path. Thus, the scattering coefficient of the tissue is always larger than the absorption coefficient of the tissue. It is difficult to determine the path length with accuracy to correctly apply the Lambert–Beer law, which relates absorbance to concentration (van der Zee, et al., 1992; Wyatt, et al., 1990). This allows NIR light to noninvasively detect physiological changes in tissues.

3.8 Modeling the Epidermis

In order to determine the properties of the epidermis, the absorption coefficients of its common constituents: melanin, baseline skin, and water must be considered. Researchers have used different methods to calculate these absorption coefficients.

3.8.1 Melanin

Melanin absorption in the epidermis depends on how many melanosomes per unit volume are in the epidermis. In untanned skin, melanin pigments are found only in the basal layer of the epidermis, while in tanned skin they are distributed throughout the epidermis. Melanin gives skin a brown color, since more green than blue light and more red than green light is backscattered from it.

In Caucasian skin, the melanosomes are smaller and dispersed in groups inside keratinocytes, whereas in darker skin, melanosomes are larger and dispersed

individually inside the keratinocytes. Dark black skin has the greatest density of pigment and the largest melanosomes, but the number of melanocytes is the same compared to Caucasian skin. The size of melanosomes determines the distribution pattern, but this pattern alone does not correlate with the intensity of pigmentation (Andersen and Bjerring, 1990).

According to Jacques (1996), it is estimated that in light-skinned adults, 1.6-6.3% of the epidermis volume is occupied by melanosomes; in moderately pigmented adults, 11-16% of the epidermis volume is occupied by melanosomes; and in darkly pigmented adults, 18-43% of the epidermis volume is occupied by melanosomes (Jacques, 1996). Researchers concluded through experiments with different race populations that melanin must be accounted for, especially if darker skinned people are being used (Matas, et al., 2002). The most common method of accounting for the absorbance of melanin has been to develop a melanin index (Dawson, et al., 1980; Kollias, 1986; Ryatt, et al., 1983).

Many groups have proposed using the difference (slope) in mean absorption between 650 and 700 nm as a melanin index even though the absorption between 650-660 nm is affected by blood oxygenation because the influence of HbO_2 on the absorption spectrum is relatively small at wavelengths greater than 620 nm (Dawson, et al., 1980; Hajizadeh-Saffar, et al., 1990). A melanin index based on the slope of the absorption spectrum between 620 and 720 nm has also been developed (Kollias and Baqer, 1988). A melanin index of $(1/slope_{365\text{-}395nm})*100$ was proposed as a because melanin is a major absorbing component in the range of wavelengths at 365-395 nm (Andersen and Bjerring, 1990).

Another approach has been to develop a melanin index from the "bloodless" absorption spectra. A three step process was used to adjust for the effects of melanin on the skin absorption spectrum (Ferguson-Pell and Hagisawa, 1995). These "bloodless" spectra were obtained by exerting pressure on the skin until all blood was displaced from that region. The resulting spectra were then assumed to result primarily from the absorbance of melanin. The first step determined the bloodless absorption spectrum and subtracted it from the measured spectrum. Then a melanin index for the skin was determined for each individual measured. The third step adjusted for the attenuation in the absorption spectrum produced by melanin, using a multiplication factor to normalize the spectrum to an amplitude that was independent of the melanin index. Linear regression was performed on the spectrum in the region of 500-600 nm to produce a melanin index. Clinically there exist situations in which it was not feasible to exert the pressure on patients required to obtain a "bloodless" spectrum. These techniques required that a separate melanin index had to be developed for each individual. An additional issue with having a single index of epidermal melanin content was that pigmentation was not constant over the entire surface of an individual's skin. Birthmarks, freckles, and accumulated sun exposure could make a difference and the skin over certain body parts was generally much lighter or darker in color than the rest of the body.

Although epidermal melanin content has been quantified noninvasively using visible reflectance spectroscopy, there are currently not many methods to determine melanin distribution in the epidermis. A photoacoustic probe was developed using a Nd:YAG laser operating at 532 nm to generate acoustic pulses in skin *in vivo* (Viator,

et al., 2004). The probe contained a piezoelectric element that detected photoacoustic waves that were then analyzed for epidermal melanin content using a photoacoustic melanin index.

Instead of a melanin index, other researchers have published wavelength-dependent equations on the absorption coefficient of melanin in the epidermis. Jacques published the following equations for the melanin absorption coefficient [mm^{-1}] (Jacques, 1998):

$$\mu_a^{mel}(\lambda) = 6.6 * 10^{10} * \lambda^{-3.33} \quad (3)$$

$$\mu_a^{mel}(\lambda) = 1.7 * 10^{11} * \lambda^{-3.48} \quad (4)$$

where λ was the wavelength [nm]. These equations yield the blue and black curves in Figure 7, respectively. The red melanin absorption coefficient [mm^{-1}] curve in Figure 7 is (Meglinski and Matcher, 2002):

$$\mu_a^{mel}(\lambda) = 5 * 10^{9} * \lambda^{-3.33} \quad (5)$$

The average absorption coefficient at λ=694 nm was used by another researcher and multiplied it by the ratio of the wavelength used to 694 nm (Svaasand, et al., 1995). In addition, the melanin absorption coefficient was different for different races (colors of skin). For example, $\mu_{a,694}^{mel}$ = 0.3 mm^{-1} corresponded to very fair North European skin, $\mu_{a,694}^{mel}$ = 0.8 mm^{-1} corresponded to Middle East and moderately pigmented Asian skin, and $\mu_{a,694}^{mel}$ = 2.0 mm^{-1} corresponded to African skin. The curve for fair North European skin is shown in Figure 7 as the green curve using:

$$\mu_a^{mel}(\lambda) = \mu_{a,694}^{mel}(694/\lambda) \quad (6)$$

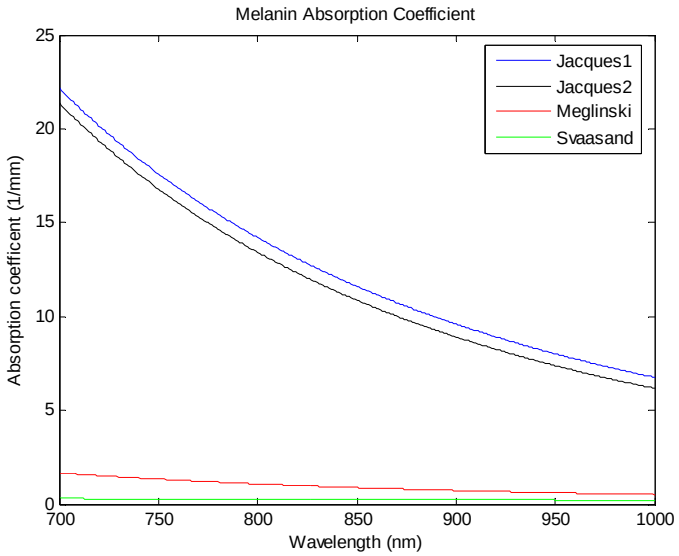

Figure 7. Melanin absorption coefficient curves for equations by Jacques (1998) (blue and black), Meglinski and Matcher (2002) (red), and Svaasand, et al. (2005) (green).

3.8.2 Baseline Skin

In addition to the melanin absorption, the skin baseline absorption coefficient must be taken into account. Researchers have also studied different approaches for determining this wavelength-dependent value. The following equation was used for the baseline skin absorption coefficient [mm^{-1}] (Jacques, 1998):

$$\mu_a^{skin}(\lambda) = .0244 + 8.53e^{\frac{-(\lambda - 154)}{66.2}} \qquad (7)$$

where λ was the wavelength [nm]. The absorption curve for this equation can be seen below in Figure 8 as the solid curve. The following equation was proposed (Saidi, 1992) and used to calculate the skin baseline absorption coefficient as seen as the dotted curve in Figure 8 (Meglinski and Matcher, 2002; Zhang, et al., 2005) [mm^{-1}]:

$$\mu_a^{skin}(\lambda) = 7.84 * 10^7 * \lambda^{-3.255} \qquad (8)$$

Skin absorption coefficient values of 0.0158 and 0.0134 mm^{-1} were previously reported (Douven and Lucassen, 2000). A value of 0.025 mm^{-1} was reported for the wavelength range of 600 to 900 nm (Svaasand, et al., 1995).

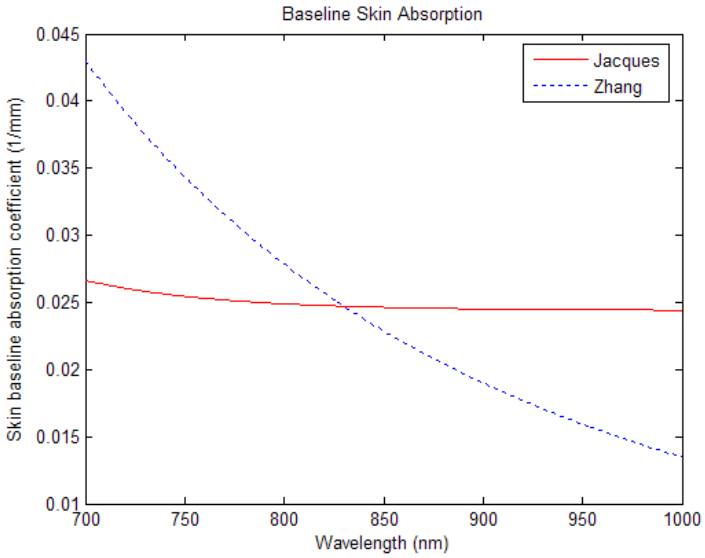

Figure 8. Skin baseline absorption coefficient curve for equations by Jacques (1998) (red solid) and Zhang, et al. (2005) (blue dotted).

3.9 Modeling the Dermis

The major component of the dermis that must be considered for the optical skin model is blood. Blood vessels in the dermis contain hemoglobin, a protein contained in red blood cells (95% of the dry mass of red cells is hemoglobin) that absorbs light and gives blood its reddish color (Anderson and Parrish, 1981). Normally, the hemoglobin concentration in whole blood is between 134 and 173 g/L and from 299 to 357 g/L for red blood cells (Roggan, et al., 1999). Hemoglobin binds very easily to oxygen, making it the ideal vehicle for transporting oxygen from the lungs to the tissue.

The majority of hemoglobin in the human blood vessels is oxygenated. More specifically, in the arteries, 90-95% of the hemoglobin is oxygenated; while 5-10% of

the hemoglobin is deoxygenated. In the veins, more than 47% of the hemoglobin is oxygenated (Angelopoulou, 2001). Skin color might vary from pink to almost bluish depending on the degree of blood oxygenation. This phenomenon occurs when oxygen-rich blood absorbs less red light and more blue light than deoxygenated blood.

Unlike the hemoglobin spectrum in the visible wavelengths, Figure 9 shows that the NIR spectrum is fairly broad and lacks sharply defined peaks, depending on whether the heme group is carrying an oxygen molecule or not (Rendell, et al., 2003). The difference in the NIR absorption spectra of HbO_2 and Hb constitutes the basis for the noninvasive determination of the relative concentrations of HbO_2 and Hb using spectroscopic measurements of the NIR reflectance of skin. The point of equal light absorbance, the isobestic point of hemoglobin, is at approximately 810 nm. At wavelengths above this point, HbO_2 has greater light absorption. Therefore, by selecting wavelengths within the NIR range, one can determine the relative contribution of HbO_2 and Hb to total light absorbance. *In vivo* NIR spectroscopic imaging provides an opportunity to examine spatial and temporal variability in cutaneous oxygenation.

Single wavelengths have been used to determine the oxygen saturation of hemoglobin in tissue (Dawson, et al., 1980; Egley, et al., 1987; Ono, et al., 1991; Takatani and Ling, 1994). Light at the wavelengths 805 and 660 nm was used by other researchers to take optimum advantage of differences in the absorption characteristics of HbO_2 and Hb. The oxygen saturation level was related to a ratio of the reflectance at the two wavelengths (Polanyi and Hehir, 1962). The fact that HbO_2

and Hb absorbed light equally at 800 nm, whereas at 760 nm absorption was primarily from Hb has also been used (Mancini, et al., 1994). Therefore, monitoring these two wavelengths provided an index of deoxygenation.

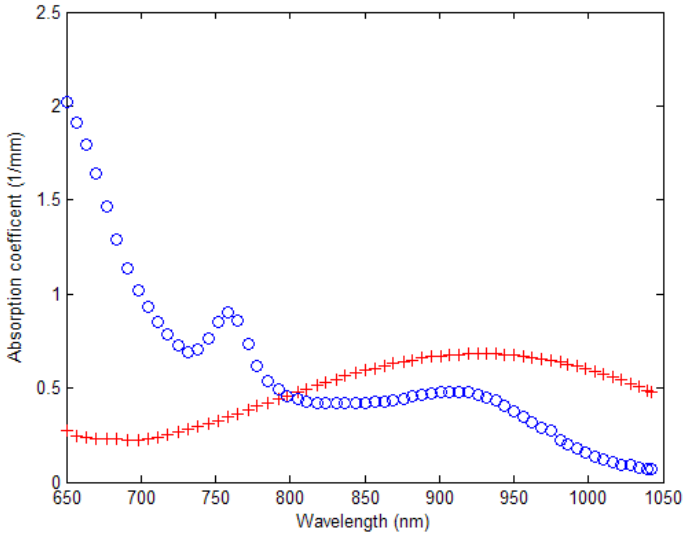

Figure 9. Oxygenated hemoglobin (red plus) and deoxygenated hemoglobin (blue circle) absorption curves.

Chapter 4: Quantitative Assessment of Tumor Vasculature and Response to Therapy in Kaposi's Sarcoma Using Functional Noninvasive Imaging

4.1 Introduction

It is now well recognized that new vessel formation is an essential component in tumorigenesis, and there is currently a substantial interest in developing therapies to treat cancer through inhibition of this process (Carmeliet and Jain, 2000; Folkman, 2002). To monitor such therapy, it is desirable to establish techniques to assess tumor vasculature and changes with therapy (McDonald and Choyke, 2003). Several imaging techniques such as dynamic contrast-enhanced magnetic resonance (MR) imaging (Taylor, et al., 1999; Verstraete, et al., 1994), positron emission tomography (PET) (Fredriksson and Stone-Elander, 2003; Jerusalem, et al., 2002), computed tomography (CT) (Hopper, et al., 2000; Rockoff, 1977), color Doppler ultrasound (US) (Ferrara, et al., 2000; Goertz, et al., 2000), and fluorescence imaging (Gill, et al., 2003; Svanberg, et al., 1998) have been used in angiogenesis-related research. However, techniques that measure such phenomena can be invasive, expensive, and/or require the application of the probe directly onto the tissue being studied. There are currently no standard noninvasive techniques to assess parameters of angiogenesis in lesions of interest or monitor changes in these parameters with therapy. This chapter describes the use of thermography and LDI to monitor KS patients undergoing an experimental anti-KS therapy.

4.2 Materials and Methods

4.2.1 Individuals With Kaposi's Sarcoma

The patients in this study all had biopsy-proven acquired immunodeficiency syndrome (AIDS)-associated KS with easily accessible cutaneous lesions. Sixteen male patients, 21 to 45 years of age, who had not received a specific KS therapy during the previous three weeks were studied. Ten patients had imaging studies done at entry and week 18 as part of a treatment protocol for the study of liposomal doxorubicin and interleukin-12 (IL-12) (Little, et al., 2003). All of the patients were receiving highly active anti-retroviral therapy (HAART) at the time of the study. Protocols for the study of these patients were approved by the Institutional Review Boards of the National Cancer Institute (NCI) and the University of Maryland and written informed consent was obtained from all patients. Relevant clinical information including the therapeutic regimens, overall response to therapy, and lesion measurements were extracted from the clinical and treatment protocol records.

4.2.2 Experimental Therapy and Clinical Assessment

Ten patients were studied at entry onto a treatment protocol of IL-12 and liposomal doxorubicin and after 18 weeks of therapy (Little, et al., 2003). The treatment regimen and preliminary clinical data for this experimental regimen have been previously described (Little, et al., 2000). Patients entered onto this study all had advanced KS, and during the first 18 weeks of therapy, they were administered liposomal doxorubicin, 20 mg/m^2 by intravenous bolus every three weeks plus IL-12, 300 ng/kg by subcutaneous injection twice weekly. After this induction phase, the

patients maintained a regimen of IL-12, 500 ng/kg by subcutaneous injection twice weekly. The overall clinical response of KS to this treatment regimen was assessed using a minor modification of the AIDS Clinical Treatment Group (ACTG) KS parameters previously published (Krown, et al., 1997; Little, et al., 2000). In short, responses were based on changes in the total number of KS lesions, the number of nodular KS lesions, the sum of the products of the larger perpendicular diameters of five representative "marker" lesions selected at entry onto the protocol, tumor associated edema or effusions, and visceral disease. A complete response was defined as the absence of all detectable disease for at least four weeks with a biopsy of at least one previous representative lesion showing the absence of malignant cells. Criteria for a partial response included a 50% or greater decrease in the number of lesions, complete flattening of at least 50% of nodular lesions, a 50% decrease in the sum of the products of the diameters of the marker lesions, or a 50% decrease in radiologically measurable visceral disease lasting at least four weeks. Criteria for progression were in short a 25% increase in the parameters noted above. A patient not meeting any of the criteria above was considered as having stable disease. Assessment of the clinical response of individual imaged lesions was by the ACTG criteria as they apply to individual lesions (Krown, et al., 1997). In particular, a partial response was defined as a 50% or greater reduction in lesion area or a complete flattening of a previously raised lesion.

4.2.3 Thermography and Laser Doppler Imaging

Most KS patients had multiple lesions on their bodies. For the study, one lesion of each patient that was at least 0.2 cm in diameter was selected. Prior to the

study, the size of each lesion was measured with a ruler in two perpendicular axes, and the size calculated as the product of these two axes. Lesion nodularity was assessed by touch as previously described (Little, et al., 2000).

Immediately prior to imaging, each patient removed sufficient garments and accessories to expose the lesion area, and an approximately 5 cm × 5 cm square mask was placed around the lesion to assist in providing orientation as to the area studied. Prior to, and during imaging, the subjects were seated at rest, in a closed room with temperature of approximately 23 ºC and humidity of approximately 50%. Thermal patterns were recorded using an infrared camera (Thermovision Alert, FLIR Systems, USA) with a uniform sensitivity in the wavelength range of 8-12 microns and temperature resolution less than 0.05 ºC. Each thermogram comprised 320 by 240 pixels and output of each pixel consisted of a 12-bit digital signal. The instrument utilized was sensitive enough to measure temperature changes resulting from variations in blood flow. Thermal images of the lesion area, the area surrounding the lesion, and the contralateral site were assessed. The mean values and standard deviation (SD) of the temperatures were calculated by averaging pixel values over a region of interest (ROI), corresponding to the visible lesion, and comparing that to the surrounding area 3-4 cm from the edge of the lesion or to the contralateral site. The position of the lesion was located by matching the mask in the images with color digital photographs of the lesion area obtained prior to the measurement.

Blood perfusion was subsequently assessed in the lesion and adjacent area of the lesion including the contralateral site using LDI. A dual wavelength (MoorLDI, Moor Instrument, Inc, UK) imager was used for simultaneous scanning at two

wavelengths, 690 nm (visible red) and 780 nm (NIR) with spatial resolution of approximately 100 microns for assessing blood flow from differing microvascular beds (Wardell, et al., 1993). The LDI images were acquired by scanning the marked lesion area. The LDI value (flux) in the lesions was quantified in arbitrary units (AU). The mean values and SD of the LDI images were calculated by averaging pixel values over a ROI at the center of the lesion and comparing this to the surrounding area 3-4 cm from the edge of the lesion or to the contralateral site. The experiments were repeated on two separate occasions to assess the reproducibility of the results and averaged the values.

In preliminary studies, temperature and flux in the ROI were compared to the uninvolved surrounding area 3-4 cm from the edge of the marked region and to an equivalent area on the contralateral appendage. We also compared uninvolved areas on both arms and legs of the same patient. These preliminary studies indicated that there was some variation between the different appendages with respect to the temperature in uninvolved areas and that the uninvolved area surrounding the ROI but within the marked area was most suitable for an uninvolved control region. Quantitative studies were thus performed comparing the ROI with the uninvolved surrounding area.

The reproducibility of temperature of the thermography and flux of the LDI systems were verified by imaging the left arm of three control subjects. The day-to-day variations in temperature and flux values were studied during three consecutive days and three times per day. The interval between the consecutive measurements within a day was 10 min. After 15-20 min of acclimatization to the room, each

subject sat comfortably with their left forearm support on an arm rest at the level of the heart. Before the experiment, the position of the forearm used for the measurement was marked, and the measurement was repeated at the same position on every subsequent occasion. The temperature and LDI values were estimated by a ROI at a marked position. Data are expressed as mean ± SD.

For the statistical analysis, data are expressed as median and interquartile ranges. The correlation between temperature and LDI value (flux) was assessed using a Spearman rank correlation coefficient (nonparametric) (Spearman, 1904). The significance of the changes in temperature and flux during therapy was determined using the Wilcoxon signed rank test (Wilcoxon, 1945).

4.3 Results and Discussion

4.3.1 Results

Table 1 shows the age of the 16 patients examined, along with the site, nodularity and size of one lesion on each person's body. All but one of the lesions were nodular and they had a median area of 124 mm^2 (range 6-336 mm^2). An example of the images obtained from a typical KS nodular lesion using different modalities is shown in Figure 10. As can be seen in the thermal image, the temperature of the lesion was approximately 2 ºC higher than that of the normal tissue adjacent to the lesion. As was the case in a number of lesions studied, the area of increased temperature extended beyond the area of the visible lesion. In some cases, the area of increased temperature followed the course of a superficial vein and was attributable to the blood in the vein. In other cases, such as the lesion depicted here, this was not associated with a superficial vein, suggesting that it was related to the

tumor process. As can be seen in the LDI image of the same lesion, there was increased blood flow in the area of the lesion compared to the surrounding tissue, with a maximum increase of over 900 AU. Unlike the thermal image, the increased blood velocity extends only slightly beyond the area of this visible lesion.

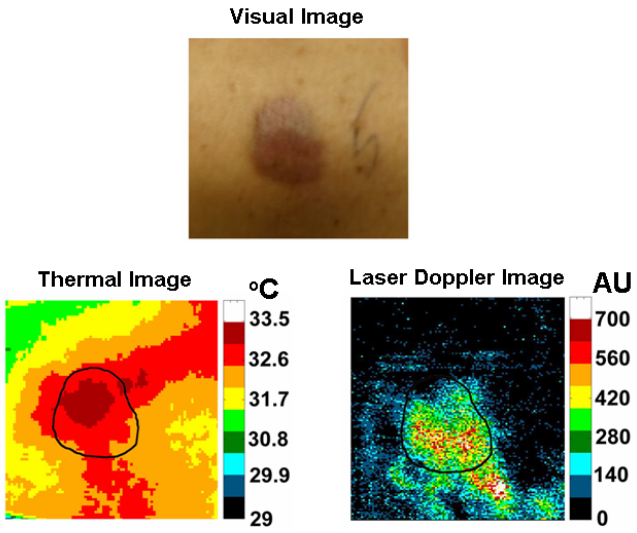

Figure 10. Typical multi-modality images obtained from a patient with a KS lesion. The number '5' in the visual image was written on the skin to identify the lesion for tumor measurement. The size of the lesion was 21 × 16 mm^2. The solid line in the thermal image and LDI demarks the border of the visible KS lesion.

Eleven of the 16 untreated lesions had a greater than 0.5 ºC elevated temperature compared to the control area (Figure 11). The median temperature elevation of the ROI compared to the surrounding area was 1.1 ºC (range -0.68 to 3.43 ºC). In addition, 12 of the 16 lesions had increased blood velocity as assessed by LDI (median 66 AU, range -44 to 451 AU). As can be seen in Figure 11, there was a strong correlation between the temperature elevation and the LDI value in these 16 lesions (R^2=0.81, p=0.0001).

Similar results were also obtained when comparing temperature and LDI values of the lesion to uninvolved contralateral sites. However, in a few cases, the contralateral appendage was also affected with a lesion. We excluded such cases from our analysis. However, there was no significant correlation in this sample set between lesion size and either temperature (R^2=0.46) or LDI value (R^2=0.39). To assess the reproducibility of the methodology, a subject was measured at the same site in the same environment on nine different occasions. Over the nine measurements, the temperature and LDI values ranged between 31.02-32.35 ºC (31.57±0.5 ºC, coefficient of variation 2%) and 132 to 154 AU (143±10 AU, coefficient of variation 7%) respectively.

Table 1. Kaposi's sarcoma patient information.

Patient no.	Age (yrs.)	Site of lesion studied	Lesion size (mm^2)	Nodularity
1	38	Right leg	350	Yes
2	44	Right chest	266	No
3	36	Right leg	357	Yes
4	38	Right knee	42	Yes
5	25	Left arm near wrist	117	Yes
6	37	Right leg	100	Yes
7	34	Right chest	48	Yes
8	38	Left shoulder	130	Yes
9	34	Right arm	130	Yes
10	45	Right shin	40	Yes
11	45	Left arm	50	Yes
12	21	Right forearm	63	Yes
13	39	Left shoulder	336	Yes
14	34	Left leg	6	Yes
15	35	Left arm near wrist	165	Yes
16	43	Left calf	336	Yes

These data provide evidence that these techniques are capable of reproducible results. The same reproducibility of the methodology was observed on two additional

subjects. Ten patients were studied at entry and week 18 of treatment with an experimental regimen combining a cytotoxic chemotherapeutic agent (liposomal doxorubicin) and an immunologic agent with anti-angiogenic activity (IL-12). One of the five representative "marker" lesions was assessed at entry onto the protocol and the same lesion was assessed 18 weeks later. Clinical parameters for the lesions are given in Table 2.

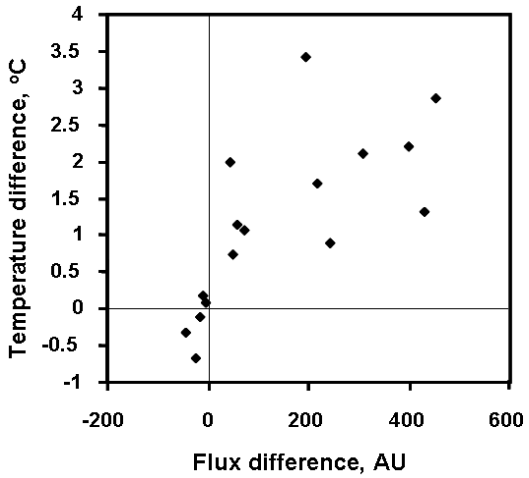

Figure 11. Relationship between the difference in temperature and flux between the lesion and area surrounding the lesion of each subject. A positive correlation was observed between these two methods (R^2=0.8, $p<0.001$).

Assessments of a typical lesion at entry and at week 18 are given in Figure 12. As can be seen, the lesion has increased temperature and blood velocity prior to therapy. However, although the lesion looks only minimally different by visual inspection at week 18, the temperature and flux are no longer increased compared to the surrounding skin.

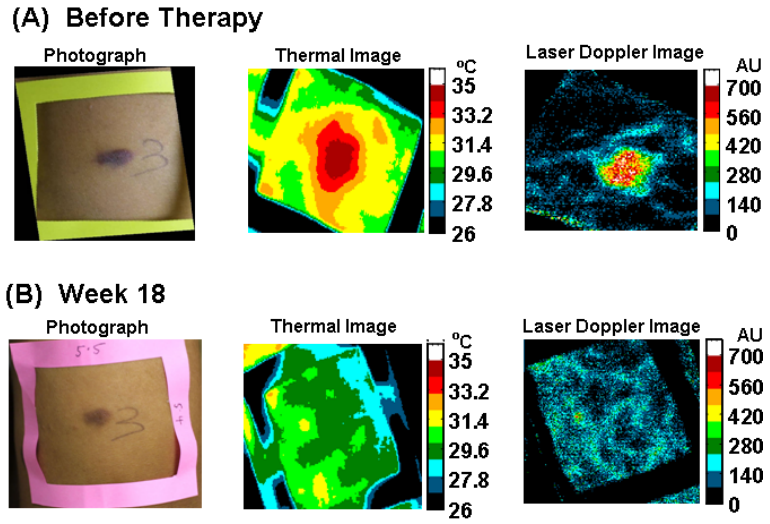

Figure 12. Typical example of KS lesion obtained (A) before, and (B) after 18 weeks of therapy. The lesion becomes normal as assessed by the thermal and laser Doppler images after 18 weeks.

In nine of the 10 patients on this regimen, the lesion studied had a decrease in temperature at week 18 of therapy (median decrease 0.99 ºC, p=0.0039) as shown in Figure 13A. In addition, the flux of the lesion assessed by LDI decreased in each of the 10 patients (median decrease 115 AU, p=0.002) (Figure 13B).

Table 2. Patient response to therapy.

Patient no.	Before Therapy		Week 18		
	Area of lesion (mm^2)	Nodularity	% reduction in area	Nodularity	KS Clinical Response
1	42	Nodular	71	Flat	PR
2	117	Nodular	70	Flat	PR
3	100	Nodular	96	Flat	PR
4	48	Nodular	69	Flat	PR
5	130	Nodular	3	Nodular	SD
6	40	Nodular	-25	Nodular	SD
7	50	Nodular	10	Nodular	SD
8	63	Nodular	24	Flat	PR
9	336	Nodular	-6	Nodular	SD
10	6	Nodular	0	Flat	PR

PR=Partial Response, SD=Stable Disease

There was a trend toward a decrease in the area of the lesions (median area was 57 mm^2 at entry and 40 mm^2 at week 18), but the change was not statistically significant (p=0.098). As noted, six of the lesions met the clinical criteria for a partial response when re-imaged at week 18, while four had stable disease. It is worth noting that the temperature and LDI values decreased at week 18 both in the lesions that met the clinical criteria for a partial response at that time as well as those that did not.

With regard to the overall KS response to therapy, all patients except for patient 7 met the criteria for a partial response at week 18; patient 7 subsequently met criteria for a partial response at week 30 while receiving maintenance therapy with IL-12 alone.

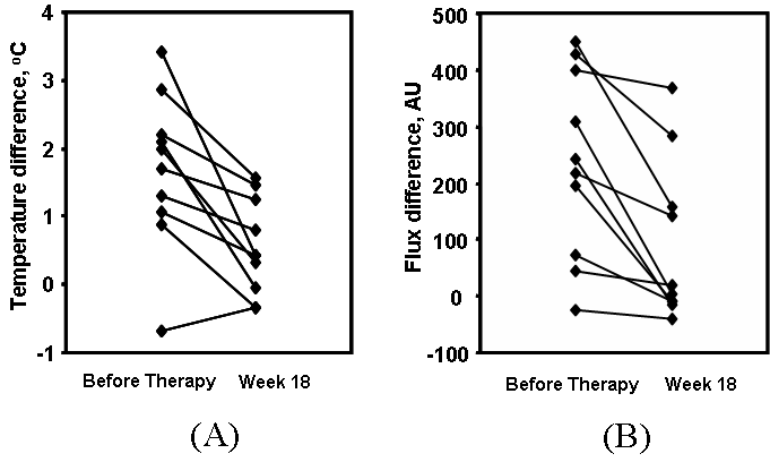

Figure 13. Differences in ten lesions compared to the surrounding tissue before and after treatment with liposomal doxorubicin and IL-12 show (A) temperature differences decrease significantly after the treatment (p=0.003) and (B) blood flow decreases significantly after the treatment (p=0.002).

4.3.2 Discussion

There is currently an intense effort to develop novel targeted therapies such as anti-angiogenic therapy, anti-vascular therapy, immunotherapy, and gene therapy for use in a variety of cancers. There is also increasing interest in approaches to monitor

tumor responses that correlate or even predict the outcome of these approaches. With regard to tumor vasculature, it is desirable to develop and assess noninvasive and quantitative techniques that can not only monitor structural changes, but can also assess the functional characteristics or the metabolic status of the tumors. If successful, newly developed imaging modalities could potentially be used as tools to predict outcome and individualize therapeutic strategies. For anti-angiogenic therapies, factors associated with blood flow are of particular interest. In this context, KS represents an attractive tumor in which to assess novel imaging techniques and assess its response to therapy (Antman and Chang, 2000; Boshoff, et al., 1997; Mercie, et al., 1999). The lesions are cutaneous, and are thus amenable to techniques that assess superficial vasculature. Also, the lesions can be biopsied without undue risk to the patient, thus offering the potential for correlation with pathological assessment of microvessels (McDonald and Choyke, 2003). Two such potential imaging techniques were assessed in this chapter, infrared thermography and LDI. Both techniques are inexpensive, easy to use, and quick. Moreover, they are completely noninvasive and non-contact. Both of these techniques can be used to visualize KS lesions. Also, although each measures an independent parameter (temperature and blood flow), they are correlated with each other, and they revert toward normal when the KS lesions are treated with an effective regimen combining cytotoxic and anti-angiogenesis therapies. IR thermal imaging is used to assess the thermal signature in the skin surface (Jain, 1988). Measuring skin temperature is an indirect method of assessing thermal effects due to blood flow. However, the thermal

signature of skin not only reflects superficial vascularity, but also deep tissue metabolic activity (Draper and Boag, 1971).

In this study, the temperature in the lesions was a median of 1.1 ºC higher than the surrounding skin. Interestingly, in a number of lesions, the area of increased temperature extended beyond the lesion edges as assessed by visual inspection or palpation. The basis for this larger area of increased temperature is unclear at this time. It may reflect relatively deep involvement of the tumor in areas underlying skin that appears normal by visual assessment. Alternatively, it may reflect inflammation surrounding the KS lesion. LDI measures the Doppler shift due to the movement of red blood cells. Using the methodology in this study, LDI enables noninvasive analysis of blood flow patterns in skin up to an approximate depth of 1 mm (Wardell, et al., 1993). It can register flow in a variety of vessels including arterioles, capillaries, and venules. The average value of LDI (flux) in the KS lesions was significantly higher than the surrounding tissue. These results extend a previous report that found that KS lesions had increased flux compared to normal adjacent skin (Leu, et al., 1994). In the present study, the size and shape of each lesion was demarcated clearly in the LDI image, and this generally corresponded to the lesion outline as assessed by visual inspection. In a majority of the lesions, the flux was highest in the center of the lesion (e.g. Figure 10). However, in some, the area of greatest flux was at the edges. The parameters accounting for these different patterns were not readily apparent and require further study. Comparative image analysis between LDI and thermography in the present study showed a strong correlation between these two parameters for the ROI ($p=0.81$). However, there were some

differences in individual lesions. LDI measures blood flow distribution in the superficial layer of skin of the lesion area, whereas the thermal signature provides a combined response of superficial vascularity and metabolic activity inside the tissue. These occasional discrepancies are thus not surprising. Similar results were also obtained by considering the contralateral site of the lesion as a control. However, it was hard to pick the same area of the contralateral extremity on different days for the analysis. It could have affected the results.

The vasculature of most tumors is relatively disorganized and does not fit the conventional hierarchy of arterioles, capillaries, and venules (McDonald and Choyke, 2003). KS lesions can be viewed as being particularly disorganized; the signature tumor cell is a spindle cell that forms vascular slits filled with blood cells (Antman and Chang, 2000). For this reason, it seemed possible at the beginning of the study that the lesions might not manifest increased blood flow as assessed by thermography or LDI. The results here, however, suggest that in spite of the tendency of KS lesions to form disorganized vascular slits, there is increased overall blood flow compared to normal tissue. A number of techniques are now being developed to image the microvasculature of tumor biopsies (McDonald and Choyke, 2003) and it will be of interest to apply such approaches to KS and correlate the results with more functional tests as utilized here. In the patients treated with liposomal doxorubicin plus IL-12, there was a substantial decrease in temperature and flux during the initial 18-week treatment period, and in some lesions, the lesions essentially normalized. In some lesions, the extent of the changes in these two parameters was greater than that

assessed by measuring the tumor area, and in fact, there was no statistically significant decrease in tumor area in the lesions overall.

4.4 Conclusions

Assessing overall responses to KS therapy is now generally performed by visually measuring and palpating the numerous lesions and using rather complex response criteria (Krown, et al., 1997). However, the current tools are rather cumbersome. Also, the techniques are subject to observer variation and this can complicate the assessment of new therapies (Yarchoan, 1999b). As such, they may be worth exploring further to assess whether they have clinical utility in the assessment of KS and in particular, whether they may be more quantitative, sensitive, or reproducible than established techniques or even provide early information that could predict subsequent responses as assessed by more conventional parameters. In summary, the present study demonstrates that thermography and LDI can be used to detect functional vascular abnormalities in KS lesions. The techniques are objective, easy to perform, and can detect improvement in the lesions upon administration of anti-KS therapy. The approaches may thus have utility in monitoring trials of anti-angiogenesis therapy in KS patients and possibly in predicting tumor responses. Perhaps more importantly, thermography and LDI can teach us about angiogenesis parameters of this disease, especially when utilized along with other novel approaches to assess tumor vasculature.

Chapter 5: Using Noninvasive Multi-Spectral Imaging to Quantitatively Assess Tissue Vasculature

5.1 Introduction

Quantitative instrumental methods offer a potentially objective means of assessing skin health that can supplement the conventional visual clinical observations. Moreover, such approaches can be used to provide early markers for tumor responses and to learn about the pathophysiology of the disease and its changes in response to treatment. NIRS is a non-contact and noninvasive method of monitoring changes in tissue blood volume and the fractions of HbO_2 and Hb. Previous studies using NIRS have just shown relative changes in tissue oxygenation, hydration or blood volume (i.e. increase or decrease). This research presents instrumental and computational methods to determine quantitative changes in functional parameters to assess KS lesions. NIRS has the potential to add functional information such as tumor and tissue oxygenation and blood volume that may aid in assessing the pathogenesis of the status and changes of the tumors during drug therapy. Moreover, this approach may provide early markers for tumor responses to treatment and allow one to learn more about the pathophysiology of the disease.

5.2 Materials and Methods

5.2.1 Instrumentation

The multi-spectral imager used in this work contains a cooled charge-coupled device (CCD) (CCD-612-TKB, Roper Scientific, Trenton, NJ) with spatial resolution

512 by 512 pixels and each image comprises a 16-bit digital signal. This array detector captures sequentially six images after the image forming light is passed through a set of narrow-band interference filters (having bandwidth of 40 nm at full width at half maximum (FWHM)) centered at 700, 750, 800, 850, 900, and 1000 nm. This filter set is located on a computer-controlled rotating filter wheel positioned in front of the camera lens used to project the image into the CCD. The schematic diagram of the imaging system is shown in Figure 14a.

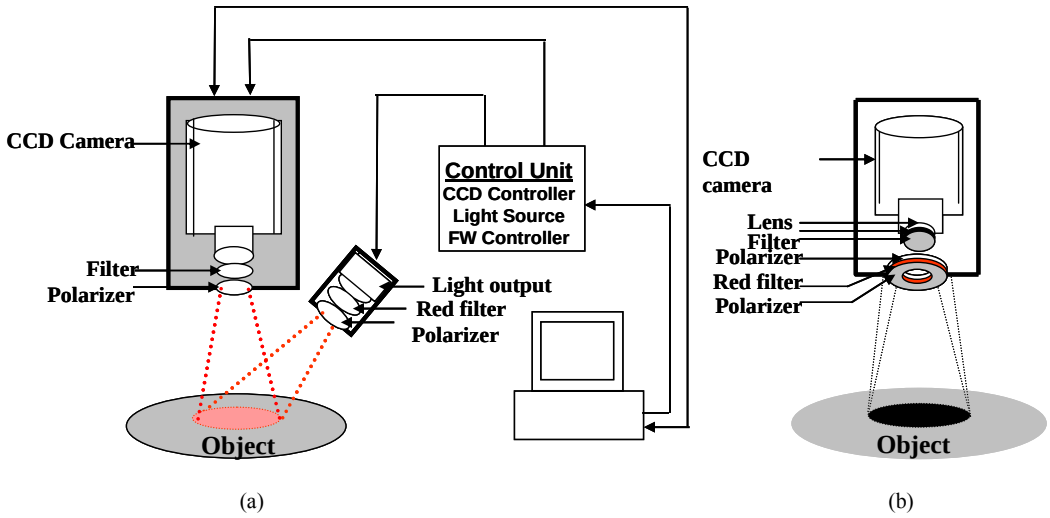

Figure 14. (a) Schematic of the original NIR multi-spectral imaging system. The filter wheel in front of the CCD camera contains six filters of 700, 750, 800, 850, 900, and 1000 nm. (b) Schematic of upgraded NIR spectroscopy system. The light source is projected directly in front of the CCD camera so that the light would shine perpendicular to the object surface.

The tissue is illuminated by a white light source (Dolan-Jenner Model 180, Edmund Optics, Barrington, NJ) that uses a 150 W EKE quartz halogen lamp. The illumination light is transported from the control unit via a 0.5 in-diameter optical fiber bundle. Polarization discrimination elements were used in order to remove the specular reflection component (which contains no functional information) from the

recorded image (Demos and Alfano, 1997). Specifically, a first linear polarizer was placed at the output of the light transporting fiber bundle after passing through a red filter (550 nm long wavelength pass) (FS40-NIR-I, CVI Laser, Albuquerque, NM) used to protect the polarizer from excessive heating. A second linear polarizer was positioned in front of the CCD camera with its polarization orientation orthogonal to that of the illumination. Both polarizers were sheet polarizers for wavelengths 740-2400 nm (Thermo Oriel (now Newport), Stratford, CT, Part #27361).

Since initially constructing the system, changes have been made in the illumination assembly to make calibration easier. The schematic of the new instrumentation is shown in Figure 14b. In the upgraded system, the light transporting fiber bundle was terminated with an o-ring arrangement of the fibers to achieve nearly perpendicular incidence of the light with respect to the tissue surface from the approximately 45^{o} angle in the original arrangement.

The system is operated using a personal computer running the Windows operating system (Microsoft, Seattle, WA) and incorporates a frame grabber card as the data acquisition hardware interface. Software has been developed to control the instrument driver routines for the CCD detector. The in-house software was written using LabVIEW (National Instruments, Austin, TX), an icon-based programming language designed for instrument control applications. The software allows the user to select experimental parameters such as the CCD detector shutter exposure time. An example of the six images collected by the CCD detector is shown in the top row of Figure 15. The grayscale bar shows the intensity of the reflected light, with white being a higher intensity. Images collected from the original and upgraded systems

were calibrated for the light intensity, light source, and camera, and curvature corrected, as described in the following section.

5.2.2 Calibration and Curvature Correction

The images collected from the system were calibrated to remove all elements of bias, including light intensity variations in space, wavelength-dependent camera sensitivity, and wavelength-dependent light intensity variations of the source. First, the light intensity variations in space were calibrated by normalizing the measured reflectance from the sample to the reflectance collected from a standard reference card (Eastman Kodak, Rochester, NY). This standard reference card provides 90% reflectance for unpolarized illumination and measurement conditions. However, it is not characterized for polarization sensitive images, which were used in these experiments. For this reason, only the spatial distribution of the intensity in the cross polarization image of the reference card was utilized (which was normalized assuming an average peak intensity equal to 1) to correct the images for the non-uniform illumination conditions. However, these images were not used as an absolute calibration standard. For this reason, the calibration procedure involved two additional steps.

The next calibration step involved the correction for the wavelength-dependent sensitivity of the camera. A standard source of spectral irradiance between 250-2400 nm (Oriel Part 63358, Spectra Physics Oriel, Stratford, CT) was used to determine the camera calibration curve including the CCD response and the optical elements attached. These values were then divided by the corresponding value at 750 nm resulting in a normalization factor of 1 at 750 nm. The results are summarized in

Table 3. The high value in Table 3 at 700 nm (2.3) is mainly due to the lower transmission of the polarizer at this wavelength. On the other hand, the high value at 1000 nm (3.8) is due to the low sensitivity of the CCD. After each set of spectral images were normalized for the spatial variation of the illumination, they were then multiplied by the corresponding wavelength-dependent camera calibration factor.

Finally, the images have undergone a third normalization process to account for the wavelength-dependent light intensity variations of the illumination source. Images of the 90% reflectance card (also used in the first calibration step) after they were corrected for the spectral response of the camera were then used to determine the average intensity at 700, 750, 800, 850, 900, and 1000 nm to extract the normalization factor for each wavelength (which is also normalized to 1 at 750 nm as shown in Table 3).

Table 3. Source and camera calibration factors by wavelength

Wavelength (nm)	Approximate Source Calibration Factor	Approximate Camera Calibration Factor	Approximate Source and Camera Calibration Factor
700	1.0	2.3	2.3
750	1.0	1.0	1.0
800	1.1	0.89	0.98
850	1.4	0.86	1.2
900	1.4	1.2	1.7
1000	2.3	3.8	8.7

The imaging system provides a field-of-view of 25 cm^2 (3.88 in^2). This differs from other approaches where point-like detectors are used to acquire information at multiple locations. However, such an image can be analyzed to individual pixels or sets of pixels and thus treated as equivalent to a multi-source, multi-detector system. A set of initial and three step calibration-corrected images are shown in Figure 15.

A major challenge when collecting images from human tissue including extremities such as arms and legs is the natural curvature. In order to remove the curvature effects in the multi-spectral images, we have developed a curvature removal algorithm was developed. After the three calibrations were performed on a set of images, the image was rotated to fit the primary curvature to the *x*- and *y*-axes. Then the average intensity for each column and each row was calculated, creating vertical and horizontal intensity curves, respectively. The vertical and horizontal intensity curves for each wavelength were then normalized and averaged over the utilized wavelengths. Then each pixel (*x,y*) in the image was divided by the normalized values of the corresponding *x* and *y* intensity curves. This allowed the effects of the curvature in the horizontal and vertical direction to be removed, without changing the underlying hemodynamic effects.

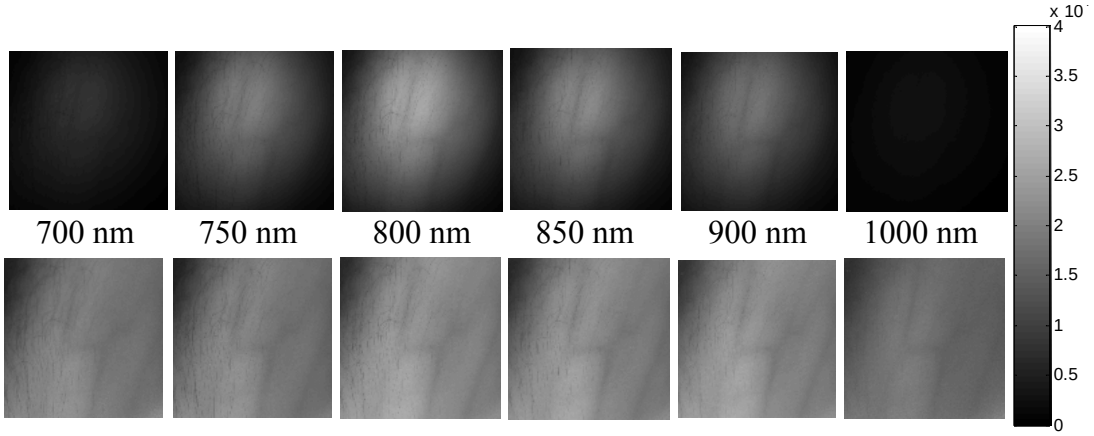

Figure 15. Spectral images of a healthy volunteer's arm at six NIR wavelengths (top row) before any calibrations and (bottom row) after intensity, source, and camera calibrations. The grayscale bar shows the intensity of the reflected light. Note that tissue image intensity is normalized after the calibrations.

This correction assumed the primary effect in intensity came from the curvature and averaging will simply removed the fluctuations caused by hemodynamic change. Averaging the utilized wavelengths should also improve the

model as any changes in intensity due to geometry should be wavelength independent. Visible lesion areas were disregarded for these calculations as they have intrinsically lower intensity than the surrounding tissue. In patients with non-visible tumors, including the tumor in the analysis did not strongly affect the results as the primary intensity effect was curvature.

5.2.3 Mathematical Optical Skin Model

This research uses a mathematical optical skin model to determine the physiological tissue parameters of interest through a best-fit multivariate analysis. The light passes through the epidermis layer, diffusely reflects through the dermis layer, passes again through the epidermis layer, and is detected by the CCD camera. This yields the following general mathematical optical skin model equation:

$$I_{\det}(\lambda) * I_{calibration}(\lambda) = S * A_{epi}(\lambda)^2 * A_{dermis}(\lambda) \qquad (9)$$

where λ is wavelength (i.e. 700, 750, 800, 850, 900, and 1000 nm), $I_{\det}(\lambda)$ is the detected intensity at each pixel for each wavelength, $I_{calibration}(\lambda)$ is the combined calibration factor described above for each wavelength (see column 4 in Table 3), S is the scaling factor (to be discussed in section 5.2.3.3), $A_{epi}(\lambda)$ is the attenuation of the light intensity after passing through the epidermis for each wavelength, and $A_{dermis}(\lambda)$ is the attenuation of the light intensity after diffusely reflecting through the dermis layer for each wavelength. The epidermis takes melanin into account and the dermis includes the contributions from blood volume and blood oxygenation.

5.2.3.1 Epidermis Layer

The effect of the thin epidermis layer on the intensity of the diffusely reflected light is based on the volume fraction of melanin in the epidermis and the epidermal thickness (Jacques, et al., 2000). The effective attenuation of light through the epidermis, A_{epi}, can be determined by Beer's Law giving:

$$A_{epi}(\lambda) = e^{-\mu_a^{epi}(\lambda)t} \tag{10}$$

where λ is the wavelength [nm], $\mu_a^{epi}(\lambda)$ is the epidermis absorption coefficient [mm^{-1}], and t is the thickness of the epidermis [mm]. The epidermis absorption coefficient, $\mu_a^{epi}(\lambda)$, depends on the percent of melanin in the skin and is given by:

$$\mu_a^{epi}(\lambda) = V_{mel}\mu_a^{mel}(\lambda) + (1 - V_{mel})\mu_a^{skin}(\lambda) \tag{11}$$

where V_{mel} is the volume fraction of melanin depending on the complexion of the skin, $\mu_a^{mel}(\lambda)$ is the melanin absorption coefficient [mm^{-1}], and $\mu_a^{skin}(\lambda)$ is the absorption coefficient of normal skin excluding melanin (baseline) [mm^{-1}]. For the results in this paper, previously reported values for $\mu_a^{mel}(\lambda)$ (Meglinski and Matcher, 2002; Zhang, et al., 2005) and $\mu_a^{skin}(\lambda)$ (Jacques, 1998) have been used (see Table 4).

Table 4. Optical properties used in the mathematical skin model.

Wavelength (nm)	$\mu_{a(deoxy)}$ [1/mm] (Jacques, 1998)	$\mu_{a(oxy)}$ [1/mm] (Jacques, 1998)	$\mu_{a(skin)}$ [1/mm] (Jacques, 1998)	$\mu_{a(mel)}$ [1/mm] (Meglinski and Matcher, 2002)	μ_s' [1/mm] (Jacques, 1996)
700	1.07	0.23	0.0266	1.68	0.93
750	0.79	0.33	0.0254	1.33	0.77
800	0.48	0.47	0.0249	1.08	0.65
850	0.43	0.58	0.0246	0.88	0.55

The remaining variable is the volume fraction of melanin in the epidermis, V_{mel}. The absorption coefficient for normal skin was considered the same for the epidermis and dermis layers. This model does not consider epidermal scattering because the probability of one scattering event in an epidermis of 0.06 mm is very small.

5.2.3.2 Dermis Layer

The influence of the much thicker, highly scattering dermis layer on the skin reflectance is estimated by a stochastic model of photon migration, e.g., random walk theory. Given the known random walk expression for diffuse reflectivity, R_o (Gandjbakhche, 1995):

$$R_o(\mu) = \frac{e^{-2\mu}}{\sqrt{24\mu}}\left[1 - \exp(-\sqrt{24\mu})\right] \qquad (12)$$

where μ is the ratio of absorption and scattering coefficients $\left(\frac{\mu_a}{\mu_s'}\right)$. To simplify computations, equation (12), as a function of μ, has been fitted by a power law plus constant. It was previously shown that for reasonable values of optical parameters of tissues in the red/near-infrared spectral range ($5\text{x}10^{-4}<\mu<0.1$), equation (12) is well approximated by:

$$R_o(\mu) = 1.06 - 1.45\mu^{0.35} \qquad (13)$$

In case of the dermis, $\mu = \frac{\mu_a^{dermis}(\lambda)}{\mu_s'(\lambda)}$ where $\mu_s'(\lambda)$ and $\mu_a^{dermis}(\lambda)$ are the reduced scattering and absorption coefficients of the dermis, respectively. Plugging μ into equation (13) yields the equation for the dermis attenuation used in equation (9):

$$A_{dermis}(\lambda) = 1.06 - 1.45\left[\frac{\mu_a^{dermis}(\lambda)}{\mu_s'(\lambda)}\right]^{0.35} \qquad (14)$$

The dermis absorption coefficient depends on the volume fraction of blood in the tissue (V_{blood}) and the percent of that blood that is oxygenated (V_{oxy}) (relative fractions of HbO_2 and Hb in the blood). The dermis absorption coefficient [mm^{-1}] is calculated by:

$$\mu_a^{dermis}(\lambda) = V_{blood}\mu_a^{blood}(\lambda) + (1 - V_{blood})\mu_a^{skin}(\lambda) \qquad (15)$$

where V_{blood} is the volume fraction of blood in the dermis layer and $\mu_a^{skin}(\lambda)$ is the absorption coefficient of skin [mm^{-1}]. The absorption coefficient of whole blood is calculated as [mm^{-1}]:

$$\mu_a^{blood}(\lambda) = V_{oxy}\mu_a^{oxy}(\lambda) + (1 - V_{oxy})\mu_a^{deoxy}(\lambda) \qquad (16)$$

where V_{oxy} is the fraction of blood that is oxygenated, $\mu_a^{oxy}(\lambda)$ is the absorption coefficient of HbO_2 and $\mu_a^{deoxy}(\lambda)$ is the absorption coefficient of Hb. For $\mu_a^{oxy}(\lambda)$ and $\mu_a^{deoxy}(\lambda)$, previously published values were used (Delpy, et al., 1988). The reduced scattering coefficient, $\mu_s'(\lambda)$, is calculated by combining 40% Mie and 60% Rayleigh scattering components given by (Jacques, 1996):

$$\mu_s'^{mie}(\lambda) = 2 \times 10^4 \lambda^{-1.5} \qquad (17)$$

$$\mu_s'^{rayleigh}(\lambda) = 2 \times 10^{11} \lambda^{-4} \qquad (18)$$

These percentages for Mie and Rayleigh scattering components gave reasonable results when analyzing tissue from normal subjects. The wavelength dependence of the reduced scattering coefficient obtained from equations (17-18) is shown in Table 4. This combination represents the distribution of sizes of different types of scatterers

in tissue, from granules to cells. Other analytes such as hemosiderin, iron deposits created after hemoglobin is degraded, may be added into the model in the future.

5.2.3.3 Analysis

The sampling volume, considered to be the area of tissue that affects the light absorption and reflectance, is larger than the individual pixel on the surface of the skin. Each image pixel is affected by the surrounding tissue and therefore the reconstructed images of blood volume and blood oxygenation are averages of the sampling volume and are influenced by the tissue surrounding that area. The sampling volume also depends on the penetration depth of the near-infrared light source.

Preliminary Monte-Carlo simulations of the multi-spectral system and skin model have been run to determine the maximum penetration depth. The volume visited by the photons depends on the wavelength. Moreover, ~2 mm seems to be the limit of the photon penetration for the theoretical instrumental setup i.e., the photons mainly remain in the epidermal and dermal layer. It is interesting to notice that the voxels "visited" by the photons appear to be situated vertically and symmetrically under the detection pixel. In practice, this means that an image formed at the skin surface should carry information concerning the tissue mainly situated under each pixel.

Equation (9) also contains a scaling factor required to balance the two sides of the equation. This scale factor varies between and among subjects, but a standardized equation has been developed:

$$S = 2.2382 * \bar{I} \qquad (19)$$

where S is the scaling factor and $\bar{I}$ is the average intensity of a region of interest from the wavelengths of interest. The scale factor has a linear relationship with the calibrated intensity averaged across the four wavelengths ($R^2 = 0.8839$) (Figure 16). This equation was developed by analyzing normal subject data where reasonable values of tissue oxygenation and blood volume based on published data were calculated (Jacques, 1996; Angelopoulou, 2001).

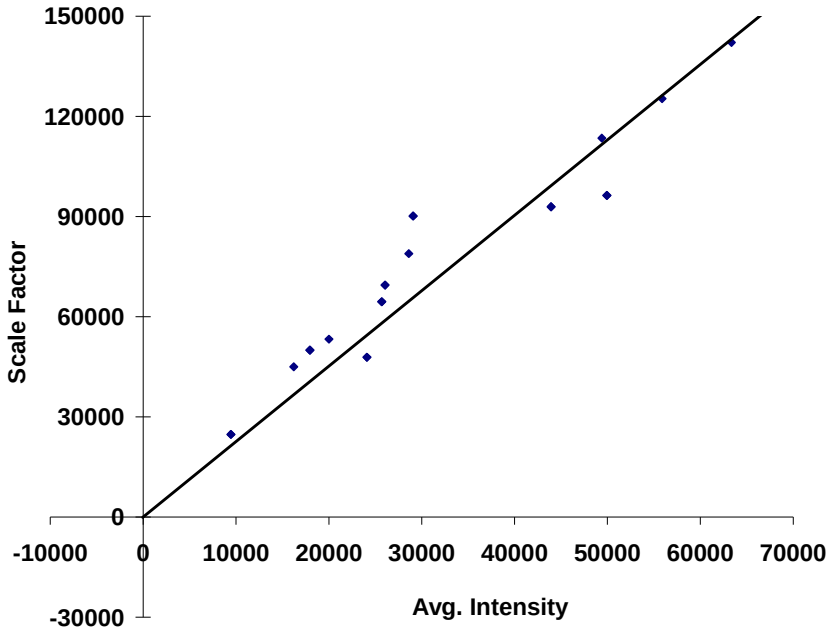

Figure 16. Fit of the standardized scaling factor used in Equation (9) (R^2=0.8839). This factor is different for each person and each visit. Each point on the graph indicates a healthy volunteer with reasonable values of HbO_2 and blood volume based on published data.

A nonlinear fit of the calibrated intensity of each pixel to the attenuation of light through both layers of the mathematical optical model is performed using the Levenberg-Marquardt algorithm (Levenberg, 1944; Marquardt, 1963). For each pixel, four equations are created, one per wavelength at 700, 750, 800 and 850 nm, of

equation (9). By inserting equations (10, 11, 14-18) into equation (9), four unknown physiological parameters can be solved for, V_{oxy}, V_{blood}, V_{mel}, and t.

The multi-spectral imaging system has the capability to use all six wavelength images and solve for two additional parameters. In future studies, when the 900 and 1000 nm images are used, one must account for the absorption of water and lipids in the model and consider their volumes as variables. For this research, t was considered to be 0.06 mm based on previous research (Nishidate, et al., 2003). The value of V_{mel} was considered constant for each subject based on the range published by Jacques for different skin types (Jacques, 1996). Performing a best-fit analysis of this set of equations allows HbO_2 and tissue blood volume to be solved for.

The spatial map of HbO_2 obtained from this analysis presents the fraction of blood in a given volume of tissue that is oxygenated. The values can range from zero to one. For example, a value of 0.80 means that the blood in a specific area of tissue is 80% oxygenated. Similarly, the spatial map of blood volume shows the fraction of blood in the tissue sampling volume (it can also vary between zero and one). For example, a value of 0.05 means that the sampled volume of tissue contains 5% blood.

5.2.4 Laser Doppler Imaging

This study combines multi-spectral imaging and laser Doppler imaging (LDI) to determine changes in blood volume, oxygenation state and blood velocity of the microvasculature. Using both imaging modalities provides a detailed analysis of tissue function that can be assessed as a possible predictive tool for the outcome and individualization of therapeutic strategies. LDI enables noninvasive analysis of blood flow patterns in skin up to an approximate depth of one millimeter. We used a dual

wavelength (MoorLDI, Moor Instrument, Inc, UK) imager for simultaneous scanning at two wavelengths, 690 nm (visible red) and 780 nm (NIR) with spatial resolution of approximately 100 μm for assessing blood flow from differing microvascular beds (Wardell, et al., 1993).

5.3 Results and Discussion

5.3.1 Healthy Volunteers

To quantify possible changes in physiological parameters due to disease presence/progression, a preliminary study of healthy volunteers was required. Twelve healthy subjects were studied during the following experiments. One of the first experiments we conducted compared a similar area on both arms of the same healthy subject. Figures 17 and 18 show the results from two different healthy volunteers. The first column of both figures shows two 700 nm images collected from the multi-spectral imaging system of the left and right forearm of the same subject. The second and third columns show the reconstructed images presenting the fractions of V_{oxy} and V_{blood}, respectively, of similar areas on the left and right forearm of one subject.

Observed values of HbO_2 in both figures are lower than 0.6, corresponding to blood oxygenation below 60%. Similarly, values of blood volume are lower than 0.2, corresponding to blood of less than 20% per sampling volume. Both figures shows an average value of 0.07 for the background skin blood volume, meaning that each tissue sampling volume contains an average of 7% blood, is close to agreement with the range given by Jacques of 0.2-5% (1996).

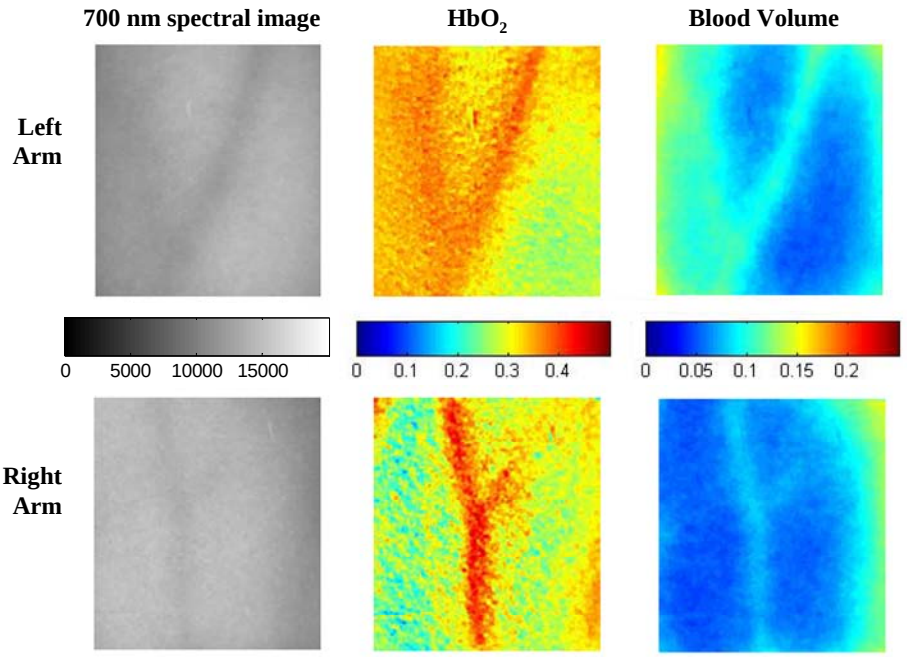

Figure 17. Set of typical images comparing a healthy volunteer's left and right forearm. Column 1 shows the calibrated 700 nm multi-spectral image. Column 2 shows the spatial maps of HbO_2 and Column 3 shows blood volume reconstructed from the set of NIR spectral images. Note that both arms show similar quantitative values for HbO_2 and blood volume.

Interestingly, a higher blood volume was observed in the vasculature compared to the surrounding tissue. The blood vessels detected by this technique are veins and arteries. Also, a higher percentage of HbO_2 appears in the vasculature compared to the surrounding tissue, showing an average of approximately 47% HbO_2 in the sampled tissue volume. The images also show consistent percentages of HbO_2 and blood volume in the vasculature and surrounding tissue on both arms.

The next study followed healthy subjects through reactive hyperemia. A pressure cuff was inflated around the subject's upper arm to induce temporary ischemia, which was relieved after several minutes. Spectroscopic image sets were

taken every 30 seconds at different time points: before the occlusion (0 min), during the occlusion (0.5-5 min), and after the occlusion was released (5.5-10 min).

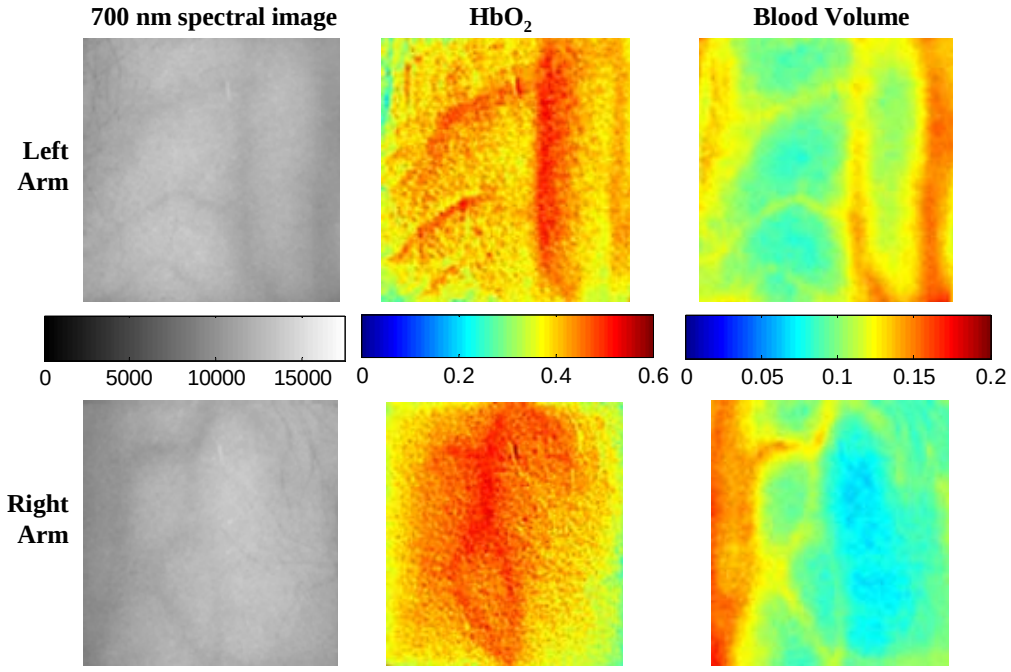

Figure 18. Set of typical images comparing a different healthy volunteer's left and right forearm. Column 1 shows the calibrated 700 nm multi-spectral image. Column 2 shows the spatial maps of HbO_2 and Column 3 shows blood volume reconstructed from the set of NIR spectral images. Note that both arms show similar quantitative values for HbO_2 and blood volume.

An example of these changes is presented in Figure 19 at three time points: before the occlusion, after five minutes of occlusion, and one minute after the occlusion was released. The pairs of spectroscopic images illustrate the changes in the distributions of HbO_2 and blood volume fractions, reconstructed from these data sets. The tissue around the vasculature appears substantially more deoxygenated during the occlusion episode than afterwards. In the bottom row of Figure 19, the skin shows a slight increase in background blood volume during the occlusion period. This follows previous results showing that during an occlusion, there will be an increase in blood

volume and a decrease in HbO_2 (Kooijman, et al., 1997; Kragelj, et al., 2001; Kragelj, et al., 2000). When the occlusion was released, the HbO_2 increased past the baseline and then returned to the baseline following several minutes.

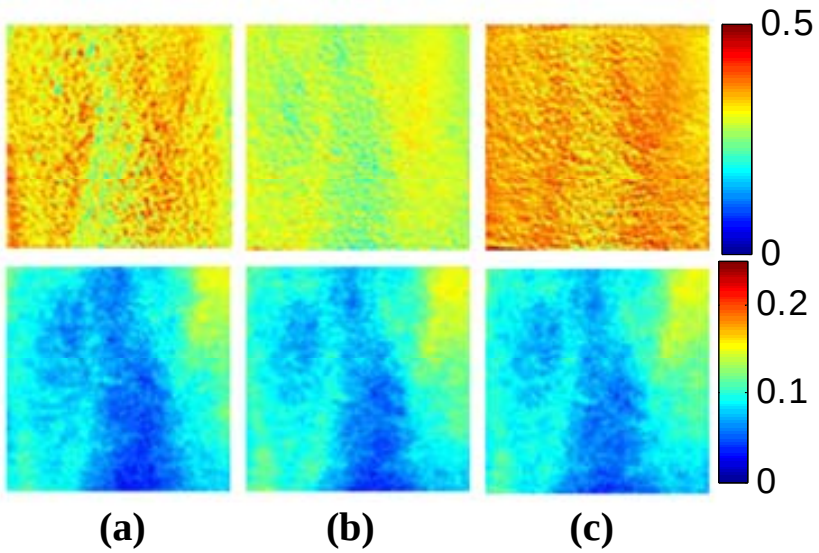

Figure 19. Reactive hyperemia experiment showing (top row) HbO_2 and (bottom row) blood volume at (a) 0 mins, (b) after 5 mins of occlusion, and (c) 1 min after releasing occlusion. During the occlusion, HbO_2 decreased and then when the occlusion was released, HbO_2 increased above the initial state. A slight increase in V_{blood} was seen after 5 min occlusion period.

Additional reactive hyperemia experiments were conducted on healthy subjects in a more longitudinal manner. Figure 20 shows the results of two visits by one healthy subject. Similar patterns of changes in V_{oxy} and V_{blood} during the experiments can be seen. In addition, similar values of initial blood volume and HbO_2 in the vasculature and surrounding tissue were observed. This experiment helps to show the stability of the system and the reconstruction algorithm. In general, spectroscopic images allow us to quantify circulatory changes of the skin in time to study physiological variations in different tissue locations.

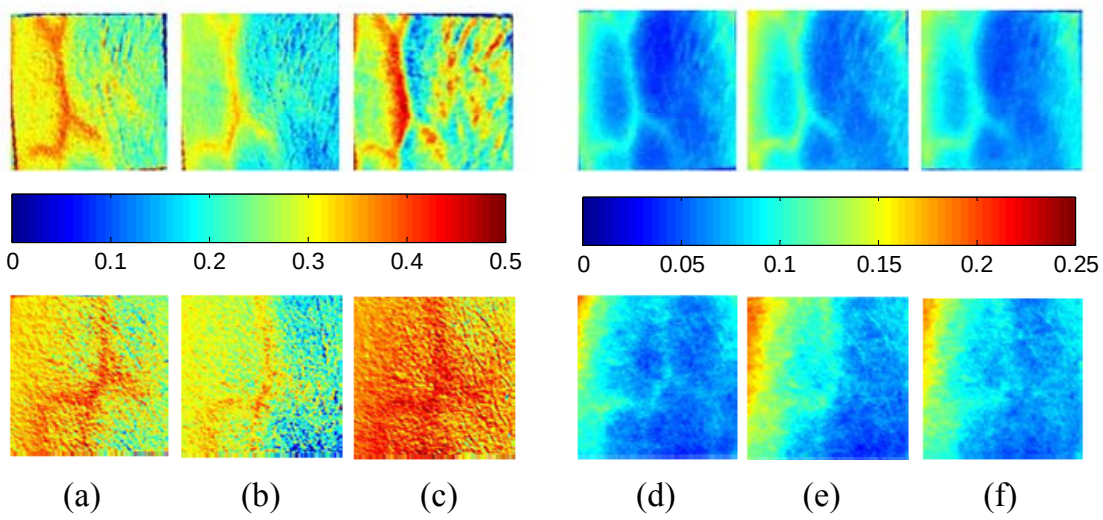

Figure 20. Reactive hyperemia experiment of the same subject on two visits showing HbO_2 and blood volume (top row is visit 1 and bottom row is visit 2). (a) HbO_2 at 0 mins, (b) HbO_2 after 5 mins of occlusion, (c) HbO_2 1 min after releasing occlusion, (d) V_{blood} at 0 mins, (e) V_{blood} after 5 mins of occlusion, and (f) V_{blood} 1 min after releasing occlusion. HbO_2 decreased during the occlusion and increased above the initial state when the occlusion was released. A slight increase in V_{blood} was seen during the 5 min occlusion period but a decrease toward the initial state was seen 1 min after releasing the occlusion.

5.3.2 Individuals With Kaposi's Sarcoma

To study diseased tissue, clinical protocols were approved by the institutional review board of the National Cancer Institute to study subjects with Kaposi's sarcoma lesions. Written consent was obtained from all subjects and lesions were considered for measurement if they were at least 0.2 cm in diameter. Immediately prior to imaging, each patient removed sufficient garments and accessories to expose the entire area to be recorded including the contralateral side. Prior to and during imaging, the subjects were seated at rest in a closed room around 23^{o}C.

Figure 21 shows a set of comparative images from one visit of a Kaposi's sarcoma subject. The digital image in the top left shows the visible location of the

surface lesion; however, the noninvasive imaging techniques show additional information about the lesion and its vasculature. To allow the visualization of the lesion in each modality image, a black line marks the location of the lesion based on the digital camera image.

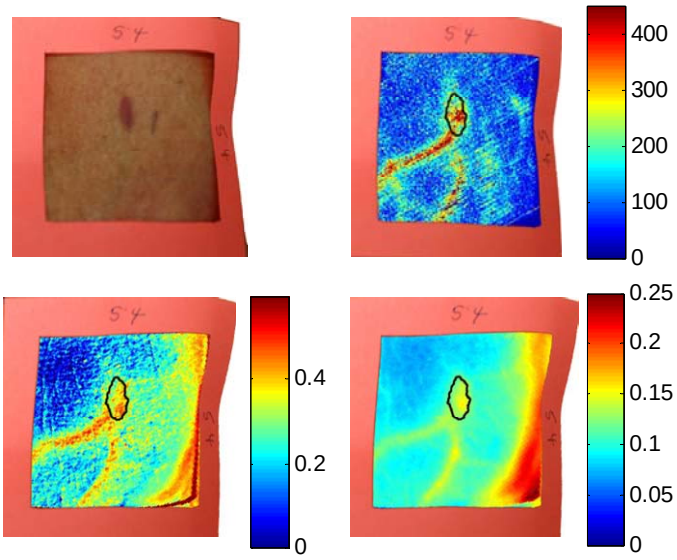

Figure 21. Images of KS subject on entry onto drug treatment protocol. (top left) digital image; (top right) LDI showing blood flux; (bottom left) reconstructed map of HbO_2; (bottom right) reconstructed map of fraction of V_{blood}. There is increased blood flux, blood volume, and HbO_2 in the lesion compared to the surrounding tissue.

One should note the presence of a vasculature network surrounding the tumor. The average oxygenation of veins in the bottom left image corresponds to the known value of approximately 47%. There is increased blood flux (top right), blood volume (bottom right) and fraction of HbO_2 (bottom left) in the lesion compared to the surrounding tissue.

To date, over 30 patients have been studied at entry onto treatment protocols of several experimental therapies. The overall clinical response of KS to this treatment regimen was assessed using the same criteria as described in Chapter 5.

Many patients that did not experience a positive response on one therapy tried a different one.

Figure 22 shows a set of comparative images of a KS patient undergoing an experimental drug therapy. It is important to note that as this patient returned for subsequent visits, the clinical assessment was stable disease. After three weeks of experimental treatment, increased blood flux and blood volume can be seen in the lesion compared to the surrounding tissue.

A set of comparative images of a KS patient collected at baseline (0 weeks) and at follow-up (19 weeks later) is shown in Figure 23. The clinical assessment of this patient, who was receiving retroviral therapy only (no experimental drug therapy), was progressive disease by week 13. The images in the left column show increased HbO_2 and tissue blood volume fractions and blood flux values in the lesion compared to the background at baseline. Note that a ballpoint pen was used to write a number next to the lesion (here a 4). This ink appears to have low HbO_2 values; however, the ink pixels were not used to calibrate the image, but the ink has strong absorption properties and behaves differently than tissue in the reconstruction. It is left in the image as a visual reference for the clinician, but its values can be disregarded.

Nineteen weeks later, the images in the right column show a lower HbO_2 fraction in the lesion compared to the background, but continue to show increased tissue blood fraction and blood flux in the lesion area compared to the background tissue. The laser Doppler images show increased blood circulation in the entire viewing area after 19 weeks. The tissue blood volume fractions were both

approximately 6% in the tissue surrounding the lesion. A square region of interest (ROI) was selected inside the lesion and compared to the reference region outside the lesion. A ROI of 25x25 pixels (625 pixels^2) was chosen inside the lesion (unless the lesion was smaller than this and then an area of 10x10 was chosen). The four 25x25 pixel ROIs chosen as the reference regions and averaged together are shown in the last row of Figure 23. Parameter averages were calculated for both areas. Table 5 shows the quantitative results of tissue HbO_2 and blood volume fractions from the subject in Figure 23.

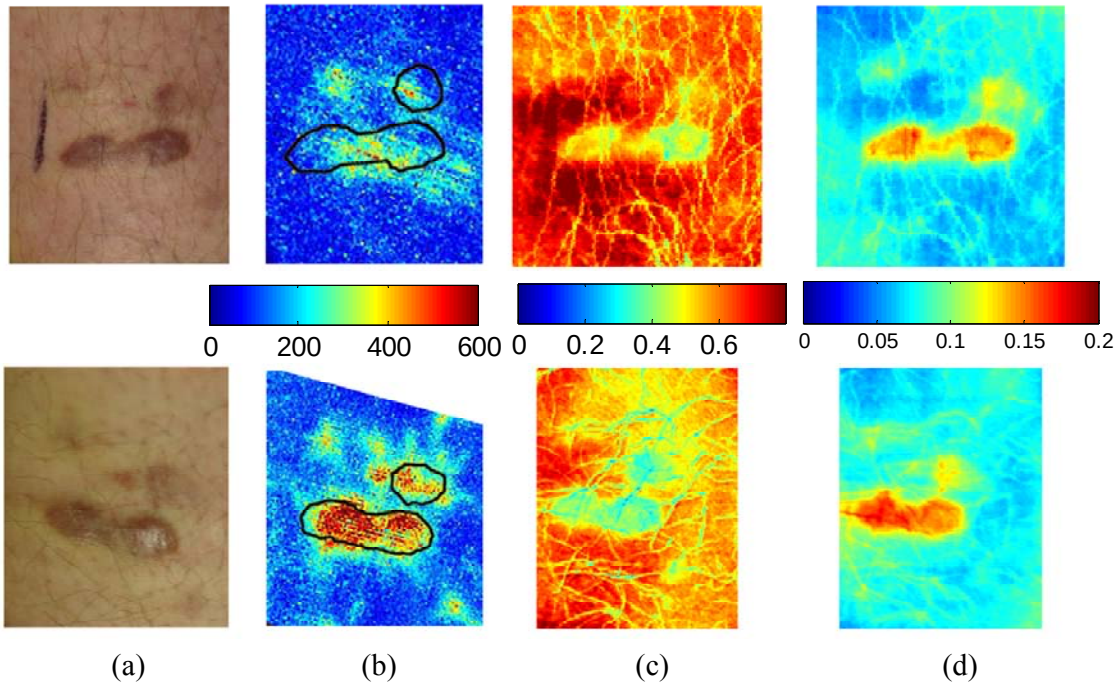

Figure 22. Images of KS subject (top row) on entry onto drug treatment protocol and (bottom row) after three weeks of experimental therapy. (a) digital image; (b) LDI showing blood flux; (c) reconstructed map of HbO_2; (d) reconstructed map of V_{blood}. The lesions appear hypoxic compared to the surrounding, but the laser Doppler and blood volume images show higher blood flux and volume in the lesions.

Results from this patient shows that as the disease progressed, the lesion became more hypoxic and the surrounding tissue became more oxygenated. Blood volume was fairly constant as the disease progressed. The blood flux, as shown in the laser Doppler images, shows a slight decrease inside the lesion as the disease progressed, but an increase of blood circulation in the area surrounding the lesion. A strong correlation between temperature, measured by thermal imaging, and blood velocity, as well as with blood volume, was previously found (Hassan, et al., 2004). Further analysis of the data we are collecting promises to further the understanding of tumor angiogenesis and the effects of experimental therapies by using multi-spectral imaging, LDI and thermal imaging.

Table 5. Quantitative oxygenated hemoglobin and blood volume results from reconstructed NIR spectroscopy images of a KS subject with progressive disease.

	HbO_2 Fraction		**Blood Fraction**		**Laser Doppler**	
	Baseline	*19 weeks*	*Baseline*	*19 weeks*	*Baseline*	*19 weeks*
Lesion (ROI mean)	0.38	0.27	0.17	0.15	830	769
Outside (ROI mean)	0.22	0.29	0.07	0.06	137	372

5.4 Conclusions

The multi-spectral imaging system reconstructs images with contrast based on spatial changes in the concentrations of analytes. The results show that quantitative spectroscopic imaging can be used for dermatological examinations. Objective information on skin health can be obtained noninvasively and without skin contact. Quantitative tissue oxygenation and blood volume data can be provided

independently, with detailed indications of variability with location, in the form of images.

The quantitative reconstructed values, or contrast, have shown utility in revealing spatial patterns of analyte concentration that correlate with KS tumor regions and can be used to show informative changes indicative of patient response to therapy. Consistent with their angiogenic nature, the KS lesions studied had greater blood volume than surrounding normal tissues. However, some appeared to be relatively hypoxic compared to the surrounding tissue, while others appeared to have increased blood oxygenation. KS involves a degree of inflammation, and it is possible that the areas of increased oxygenation reflect inflammation. It will be interesting to correlate these variations with other parameters of the KS lesions in future analyses. It should be noted that these techniques involve modeling based on certain assumptions and calculations, and it may be possible to refine the techniques further.

Overall, multi-spectral imaging is a noninvasive technique that can detect the progression of disease before these changes are visibly apparent. This technique is now also being considered for use in studies of other skin characteristics, including erythema, blanching, edema, and fibrosis. Near-infrared spectroscopic imaging has potential to be the technique of choice to supplement visual examination.

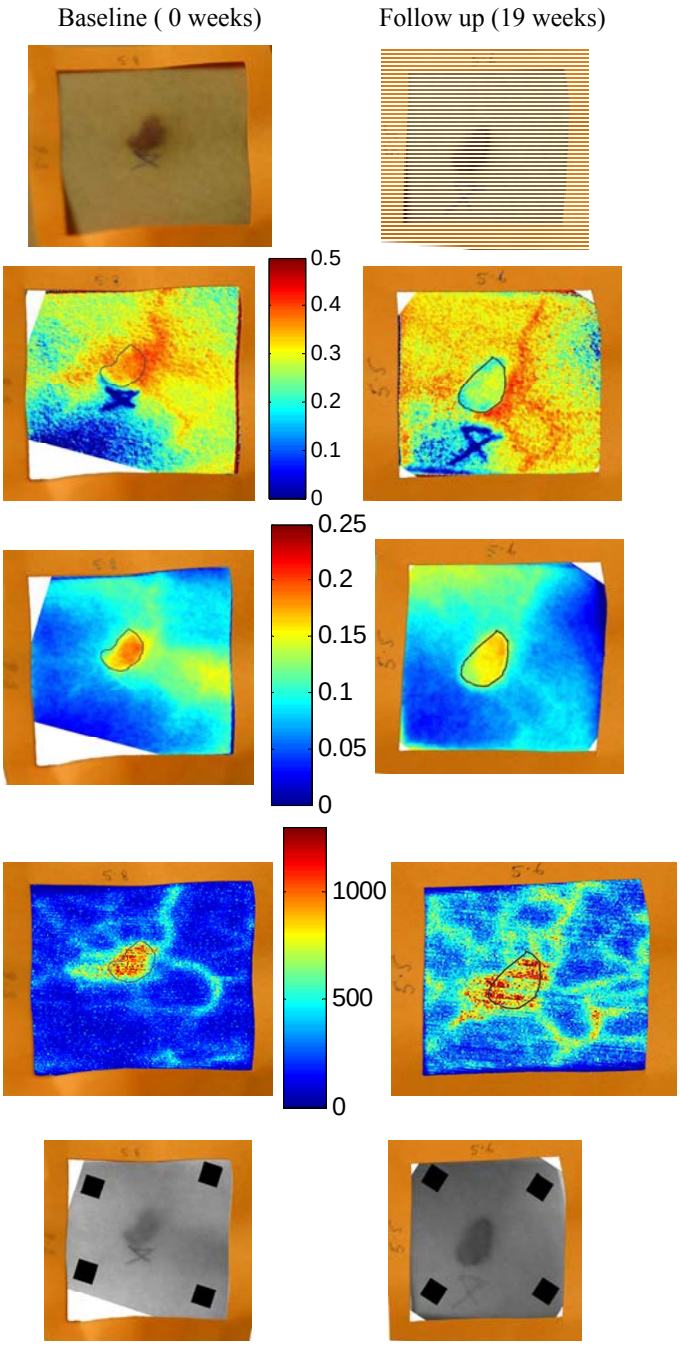

Figure 23. Images of KS subject receiving antiretroviral therapy (left column) upon entry onto protocol at 0 weeks and (right column) follow-up 19 weeks later. (top) digital image; (row one) reconstructed map of HbO_2; (row two) reconstructed map of V_{blood}; (row three) LDI; (row 4) 700 nm spectroscopic image showing the four ROIs used to average the oxygenated hemoglobin and blood volume outside the lesion. This patient had a clinical diagnosis of progressive disease before the follow-up visit. Decreased V_{oxy}, V_{blood}, and flux in the lesion are apparent at the follow-up visit. Increased overall vasculature and HbO_2can be seen in the laser Doppler and HbO_2 images at follow-up.

Chapter 6: Detection Limits of Multi-Spectral Optical Imaging Under the Skin Surface

6.1 Introduction

The integumentary system is the largest organ system of the body and is subdivided into two components: skin and epidermal derivatives (nails, hair, etc.) (Odland, 1991). It is well known that clinical examination of the skin is significant because its superficial color/appearance may indicate the existence of pathologic conditions such as jaundice, cyanosis, anemia, skin pigmented lesions, etc. The visual manifestations of different pathologies can be explained by the fact that ambient light may enter the skin and leave it after having traveled for a while inside the tissue. Upon exit from the skin, this light carries significant information about the optical/physiological parameters of the tissue. For this reason, a medical doctor with a well-trained eye is capable of observing the color of a patient's skin and then interpreting it as an indirect clinical sign of the underlying pathologies.

It is clear that in the present context it would be extremely difficult to replace the analytical and decisional power of an experienced medical doctor with an instrument. A machine cannot simultaneously take into account the numerous parameters and constraints integrated in the analytical process developed by a human being. However, an instrument may become extremely useful if it provides complementary information to what already exists. In fact, for a dermatologist, it is very difficult to precisely quantify features appearing on the skin surface. Moreover, the human eye is sensitive only to a restricted range of wavelengths and thus

interesting information carried by wavelengths not detectable by the human eye might be lost. The eye is also in principle only capable of detecting a mean effect induced by all the chromophores present in the skin and thus cannot decide if a change in intensity of detected light is specifically due to an anomalous concentration of hemoglobin, melanin, water, etc. or more complex situations (the eye, contrary to the ear, is not capable of analyzing the frequency of the detected signals). In this sense, knowledge of the exact chromophore content of the tissue would certainly help to better define the underlying pathology and physiology.

New instrumentation aimed at overcoming the above problems has been developed and tested for various skin conditions, including monitoring cutaneous edema or erythema (Stamatas, et al., 2006), automatically detecting melanoma (Tomatis, et al., 2005) and evaluating the response of vascular tumors to experimental therapies (Vogel, et al., 2007). In practice, the common basis of these technologies is the capability of generating images of skin at different wavelengths (light at different wavelengths is usually projected on the skin by a source and then detected again; e.g. by a CCD camera). This allows one to obtain spectral images – the mathematical analysis of which theoretically allows information concerning fundamental molecules contained in the skin such as hemoglobin, melanin, water, and lipids to be extracted and thus gives a signature of the status of the investigated tissue.

Algorithms utilized to extract physiological information from spectral images are based on the hypothesis that all photons traveling inside the tissue visit the same volume of tissue, independent of wavelength. However, the optical parameters such as the scattering and absorption coefficients may strongly depend on wavelength, it

becomes unclear if the above hypothesis is true or if this problem may be considered negligible. As a consequence, it is not known to what tissue depth these imaging techniques can investigate because they give only a surface projection of the underlying tissue structure. In this sense, a vascular skin tumor appears on the image as a geometrical shape with a different intensity than the background. The high scattering values of the skin make it impossible to know if the projected size was under- or over-estimated.

The aim of the present work was to investigate the above problems by using the Monte Carlo method as a virtual spectral imager to study: 1) the behavior of the photons at different wavelengths traveling inside human skin tissue and 2) the possible influence of this behavior on the resulting spectral images.

6.2 Materials and Methods

6.2.1 Optical Skin Phantom

The tissue geometry is represented by a 3D matrix (50x50x1504) of voxels (1000x1000x20 μm) which generates a phantom of size 50x50x30.08 mm (including tissue and surrounding air). The 3D matrix elements have positive integer values and a given integer relates to a specific tissue (e.g. stratum corneum, living epidermis, etc.) or air, which has a set of biological and optical parameters defining it. In this study, the optical skin phantom is an improved version of the well-tested seven layer Meglinski and Matcher model (Meglinski and Matcher, 2002; Meglinski and Matcher, 2003) with the added ability to insert inclusions of pathological tissue (or tissue different from the background). The Meglinski and Matcher model considers the epidermis to form only two distinct layers, the stratum corneum and living

epidermis. The dermis layer is divided into four regions to take into account the varying spatial distribution of blood content due to the presence of the vascular plexi. The fat layer is considered to be its own unique layer.

An air space of two voxels is present on all sides of the volume defining the skin region (thus the actual size of the skin tissue is 46x46x30 mm). The thicknesses of the different layers are defined in Table 6. Table 6 also includes the physiological parameters V_{blood}, V_{water}, V_{fat}, and V_{mel} that correspond to the volume fractions of blood, water, fat, and melanosomes in a given layer, respectively. It is important to note that V_{water}, V_{fat}, and V_{mel} represent the fractions after the blood volume has been subtracted from the tissue. Since the epidermis is usually considered a first approximation blood-free tissue, V_{mel} represents the volume fraction of melanosomes contained in this layer. Table 6 contains the V_{mel} values for a typical adult Caucasian (downloaded from the Oregon Medical Laser Center web site http://omlc.ogi.edu/). The parameters V_{oxy}, Hct, V_{Hbtot}, and V_{rbc} represent the oxygen saturation, hematocrit, volume fraction of erythrocytes, and volume fraction of hemoglobin in the erythrocytes, respectively. Table 6 reports additional optical parameters including the anisotropy factor g, refractive index n, and the scattering coefficient μ_s for each layer. These parameters are dependent on wavelength, λ [nm], but like the Meglinski and Matcher model, they have been considered constant for each given layer.

The optical absorption coefficients of the different layers are obtained as follows. For the stratum corneum, the absorption coefficient was calculated as:

$$\mu_{\mathrm{a}}^{\mathrm{corneum}}(\lambda) = ((0.1 - 0.3\times 10^{-4}\,\lambda) + 0.125\,\mu_{\mathrm{a}}^{\mathrm{skin}}(\lambda))(1 - V_{H_2O}) + V_{water}\,\mu_a^{water}(\lambda) \quad (20)$$

where $\mu_a^{water}(\lambda)$ [mm^{-1}] is the absorption coefficient of pure water and $\mu_a^{skin}(\lambda)$ [mm^{-1}] is the intrinsic absorption coefficient of skin free of any absorbers and expressed as:

$$\mu_a^{skin}(\lambda) = 7.84 \times 10^7 \lambda^{-3.255} \tag{21}$$

The absorption coefficient for the remaining layers can be expressed in a general form as:

$$\begin{aligned} \mu_a^{layer}(\lambda) &= (1 - V_{oxy})\gamma W_{blood}\mu_a^{deoxy}(\lambda) + V_{oxy}\gamma W_{blood}\mu_a^{oxy}(\lambda) \\ &+ (1 - \gamma W_{blood})V_{water}\mu_a^{water}(\lambda) + (1 - \gamma W_{blood})V_{fat}\mu_a^{fat}(\lambda) \\ &+ (1 - \gamma W_{blood})V_{mel}\mu_a^{mel}(\lambda) \\ &+ (1 - \gamma W_{blood})(1 - V_{water} - V_{fat} - V_{mel})\mu_a^{skin}(\lambda) \end{aligned} \tag{22}$$

where the total volume fraction of hemoglobin in blood is expressed as:

$$\gamma = V_{Hbtot} V_{rbc} Hct \tag{23}$$

and $\mu_a^{deoxy}(\lambda)$, $\mu_a^{oxy}(\lambda)$, and $\mu_a^{mel}(\lambda)$ are the absorption coefficients for Hb, HbO_2, and a single melanosome, respectively. The V_{water} and V_{fat} values for the hypodermis were obtained from Duck (Duck, 1990). The values for $\mu_a^{water}(\lambda)$ (human), $\mu_a^{deoxy}(\lambda)$ (human), $\mu_a^{oxy}(\lambda)$ (human), $\mu_a^{fat}(\lambda)$ (pig) and $\mu_a^{mel}(\lambda)$ (human) were downloaded from the Oregon Medical Laser Center web site (http://omlc.ogi.edu/), where the first four absorption coefficients were given as numerical lookup tables and the last:

$$\mu_a^{mel}(\lambda) = 1.7 \times 10^{11} \lambda^{-3.48} \tag{24}$$

The values for the scattering coefficients relative to each layer were more difficult to find in the literature; especially because they require an analytical expression that takes wavelength dependence into account. For this reason, an improved analytical description of the scattering parameters has been introduced only in one case, and

where it was not possible, the classical constant values from the Meglinski and Matcher model (Meglinski and Matcher, 2002; Meglinski and Matcher, 2003) were utilized.

Table 6. Typical physiological parameters defining the tissue layers utilized in the model.

Layer	Thick-ness [μm]	V_{blood}[1]	V_{oxy}[1]	Hct[1]	V_{Hbtot}[1]	V_{rbc}[1]	V_{water}[1]	V_{fat}	V_{mel}[2]	g[1]	n[1]	μ_s [mm^{-1}][1]
Stratum corneum	20	0.00	0.0	0.00	0.00	0.00	0.05	0.00	0	0.86	1.50	100
Living epidermis	80	0.00	0.0	0.00	0.00	0.00	0.20	0.00	0.02	0.80	1.34	45
Papillary dermis	160	0.04	0.6	0.45	0.99	0.25	0.50	0.00	0	0.90	1.40	30
Upper blood net dermis	100	0.30	0.6	0.45	0.99	0.25	0.60	0.00	0	0.95	1.34	35
Reticular dermis	1400	0.04	0.6	0.45	0.99	0.25	0.70	0.00	0	0.80	1.40	25
Deep blood net dermis	100	0.10	0.6	0.45	0.99	0.25	0.70	0.00	0	0.95	1.38	30
Hypo-dermis[3]	28140	0.05	0.6	0.45	0.99	0.25	0.70	0.56	0	0.75	1.44	see text

[1] Meglinski and Matcher, 2002
[2] Oregon Medical Laser Center web site (http://omlc.ogi.edu/)
[3] Duck, 1990

The reduced scattering coefficient is found by $\mu_s'(\lambda) = (1-g)\mu_s(\lambda)$. The reduced scattering coefficient for the hypodermis was given as (Bashkatov, et al., 2005) [mm^{-1}]:

$$\mu_s'^{hypodermis}(\lambda) = 1050.6\lambda^{-0.68} \qquad (25)$$

6.2.2 The Monte Carlo Method

The propagation of photons in the phantom has been simulated by the classical Monte Carlo (MC) method where the main characteristics are summarized in the present section. The algorithm was implemented on a cluster of nine computers (DELL™, OptiPlex GX620, USA) with CPUs running at 3.2 GHz. In fact, MC simulations of light transport are ideally implemented as distributed calculations (Kirkby and Delpy, 1997). One computer was utilized as a client, distributing the jobs to the remaining eight. The MC code was developed in MATLAB 7.4 language (The Mathworks, Inc., Natick, MA, USA) and the interaction between the computers was controlled by the MATLAB Distributed Computing Engine 3. This schedules and evaluates tasks on multiple remote MATLAB sessions, reducing execution time compared to running in a single MATLAB session. This approach allows a very fast prototyping of the MC code by taking advantage of the already built-in mathematical and graphical functions in MATLAB. It has been estimated that a gain of a time factor of ~7.5 can be obtained with eight machines compared to only one.

To improve the signal to noise ratio and the efficiency of the simulations, the implicit photon capture variance reduction technique was utilized (Wang, et al., 1995). The photon packet propagation was terminated when it reached the air (i.e. at the detection site) or by the roulette termination technique (Sobol, 1975). The trigger value engaging the roulette algorithm was fixed at $W<1\text{x}10^{-4}$ and the photon packet had a chance of 1/10 to survive with a new weight, $10W$, where W is photon weight. The starting weight value for a photon was $W=1$. The photon packet steps were generated by means of the variable step (s) size method (Prahl, et al., 1989). If s is

sampled in this manner, it is equivalent to saying that the photon is forced to be absorbed or scattered after each step (there must be interaction). The model describing the change in direction of a photon packet after a collision in biological tissue was represented by the Henyey-Greenstein scattering phase function (Henyey and Greenstein, 1941). Reflection at boundaries was taken into account using the Snell-Decartes' law and Fresnel's formulas. The air-tissue index mismatch was also taken into account when injecting the photons. Reflection on all boundaries was treated as an all-or-none problem, i.e. the photon packet was either completely reflected or completely transmitted based on a probability derived from Fresnel's law. The pseudo-random number generator was proposed by Witt (Witt, 1977) and implemented in this work by using a modified version of the Marsaglia's subtract with borrow algorithm (Marsaglia and Zaman, 1991) already implemented in the MATLAB language. During the distributed computations, the pseudo-random number generator of each computer of the cluster was randomly and independently initialized to ensure the generation of different random numbers in each computer.

6.2.3 Simulation of a Spectral Imager

The virtual spectral imager comprised of a 30 mm diameter uniform light source of a given wavelength centered at the center of the optical phantom projecting on the surface of the stratus corneum layer (cartesian coordinates: (25,25,0.04) mm; the 0.04 mm shift is due to the presence of the air border of two voxels). In practice, a uniform distribution of photons entering the tissue normal to the air/skin interface was generated (see Figure 24A).

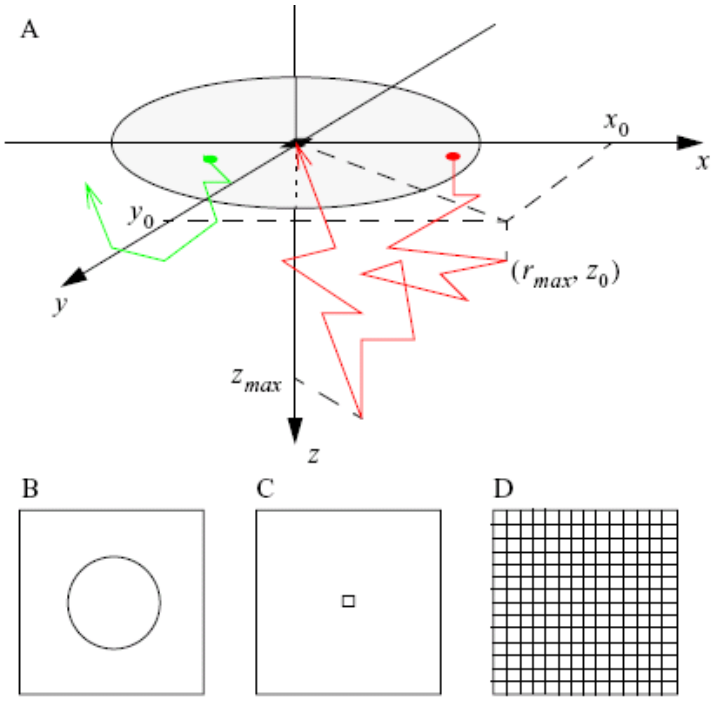

Figure 24. A) A typical path (red line) covered by a photon packet. The surface parallel to the (x,y)-plane defines the superior surface of the skin phantom (air/stratum corneum interface). The shaded circular region represents the uniform light source of 30 mm diameter projected normally on this surface that is situated at only 40 µm along the z axis (distance not visible on the figure due to the scale). The other boundaries of the skin phantom are not drawn to maintain the clarity of the figure. The photon packet starts inside this region (red spot) and arrives at the detector represented by the black pixel. The maximum depth, z_{max}, and the maximum horizontal distance (from the detector), $r_{max}(x_0 + y_0)^{1/2}$, at a depth z_0 reached by the packet appear also in the figure. During the propagation the photon packet can pass through different tissue layers (not represented in the figure). All of the photons do not reach the detector and they can also fall outside the circular region defined by the source (e.g. green line). B, C, D) These three figures represent the three detectors utilized in the present work. A unique large circular detection region, a single pixel and a grid of pixels (the figures are schematic and not in scale). The square represents the upper surface of the skin tissue (i.e. x-y plane). The light source remains always the same as represented in A.

A spectral imager typically has a CCD camera that captures the light at the skin's surface and reproduces it as an image. However, to be able to investigate the information content of these images and the optical properties of the phantom, three

types of detectors were utilized in the numerical simulations described below. Thus, depending on the problem investigated, the detector was simulated as a:

1) Large region corresponding exactly to the surface covered by the light source (i.e. detecting all photons reaching this surface as a whole, see Figure 24B);
2) Unique pixel centered at the center of the source (allowing one to study in a more fine way the information content of one pixel, see Figure 24C); or
3) Grid of pixels spanning the air/stratum corneum interface (i.e. analogous to the CCD detector; allowing one to study the image produced at the tissue surface, Figure 24D).

6.3 Simulation Descriptions

6.3.1 Skin Reflectance Spectrum and Color

The purpose of this experiment was to generate a reflectance spectrum ($R_c(\lambda)$) in the 440-1000 nm wavelength range to ensure the skin model had reasonable physiological and optical parameters. In this case, the detector geometry was defined as in Figure 24B (a 30 mm diameter disk). This source/detector configuration corresponds to the standard integrating sphere CIE geometry 0/D (i.e. normal illumination diffuse light collection). CIE is a short for Commission Internationale de l'Eclairage and is the French title of the international commission of light. The $R_c(\lambda)$ values were obtained by computing the ratio of the number of detected photons to the number of injected photons for 17 different wavelengths (from 440 to 700 nm by 20 nm steps and 800, 900, and 1000 nm). Both specular and diffusive components were

taken into account in the $R_c(\lambda)$ calculation. Each of the 17 simulations required N=1,000,000 photon packets to be generated.

6.3.2 3D Information Contained in One Detection Pixel

The aim of this simulation was to investigate the information contained in a typical spectral image pixel and estimate which skin layers and the maximum depth the detected photons visited. For this experiment the detector pixel was 0.5x0.5 mm^2 (Figure 24C). Since the source was very large (30 mm diameter, Figure 24A) compared to the detection pixel, a small shift of this pixel on the skin surface would not significantly change the results of the simulations. This pixel is representative of the others situated close by (the majority of the pixels situated in the illuminated region). The use of light polarizers, commonly included in the hardware of spectral imagers, has been indirectly taken into account by not detecting the specularly reflected photons at the air/stratum corneum boundary. For the purpose of this study, the influence of light polarization (e.g. due to the use of a laser source instead of a normal lamp with interference filters) on the photon scattering behavior inside the tissue has not been considered.

The photon packets were launched randomly as previously explained. For each photon packet (fraction) reaching the detector, the position of the packet, (x,y,z), at each step composing its path and the corresponding final weight were added in a 3D matrix, $N_\lambda(i_x, i_y, i_z)$. The matrix indexes were defined as:

$$i_x = \left\lfloor \frac{x}{\Delta x} \right\rfloor \ , \ i_y = \left\lfloor \frac{y}{\Delta y} \right\rfloor \ , \ i_z = \left\lfloor \frac{z}{\Delta z} \right\rfloor \qquad (26)$$

The parameter values for Δx, Δy, and Δz were [mm]:

$$\Delta x = \frac{51}{204} \quad , \quad \Delta y = \frac{51}{204} \quad , \quad \Delta z = \frac{5}{240} \qquad (27)$$

The mathematical symbol $\lfloor x \rfloor$ means "the largest integer less than or equal to x." More precisely, all the $N_\lambda(i_x, i_y, i_z)$ elements composing a given path have the same final weight value. The index λ is used to remember that the experiment depends on the wavelength. At the beginning of the simulation the matrix is represented by a null 3D matrix. The total weight of all the photon packets that have reached the detector at the end of the simulation was N_λ^{detect}. All photon packets were taken into account in the results and no exclusion criteria to speed up the code were utilized (e.g. too long propagation time, too large depth, etc.). For each MC simulation run, N=1,000,000. This protocol was repeated for λ=600, 700, 800, 900, and 1000 nm, corresponding to typical wavelengths used in spectral imaging when investigating tissue situated a few millimeters under the skin surface.

6.3.3 Detection of Pathological Inclusion

The aim of this experiment was to generate a set of images that simulated a real spectral imager monitoring the surface of skin that contained a pathological inclusion (tissue different from the background). For this reason, an inclusion of 10x10x0.5 mm was inserted under the skin surface of the phantom at two different depths: 20 μm (just under the stratum corneum, e.g. a vascular tumor) and at 520 μm (multiple layers). All optical and physiological parameters of the inclusion were exactly the same as the tissue background (shown in Table 6) and in the original layer structure, except V_{blood}=0.6 for the inclusion. The detector was a 2D grid covering the whole surface of the phantom with a pixel size of 0.25x0.25 mm (Figure 24D). This is

analog to the CCD camera of a real spectral imager. This 2D grid geometry corresponds also to the 2D matrix where the detected packet intensities were stored. The i_x and i_y matrix indices were computed as in Section 6.3.2; however, the position corresponding to the skin surface, i_z, was constant and did not appear in the 2D matrix. As was the case in Section 6.3.2, N=1,000,000 and λ=600, 700, 800, 900, and 1000 nm simulations were tested for each of the two inclusion depths.

6.4 Results and Discussion

6.4.1 Skin Reflectance Spectrum and Color

Figure 25 shows $R_c(\lambda)$ values for the skin phantom in a graph on the top left. To the right of the curve is the estimated skin color derived from the $R_c(\lambda)$ values. This color was obtained by computing the XYZ tristimulus values and then transforming them in the displayable and printable RGB color space (Westland and Ripamonti, 2004; Wyszecki and Stiles, 1967). More precisely, a piecewise cubic Hermite interpolation was applied to the values to obtain a higher λ resolution of 5 nm (continuous line in Figure 25). The interpolated $R_c(\lambda)$ was extrapolated to fill the gap between 400 and 440 nm ($R_c(\lambda)$= $R_c(440)$ for $400 \leq \lambda < 440$). The interpolation and extrapolation procedures were performed in accordance with CIE recommendations. Then, the CIE XYZ tristimulus values were computed using the following definitions:

$$X = k \sum_{\lambda=400}^{700} R_c(\lambda) x(\lambda) P(\lambda) \tag{28}$$

$$Y = k \sum_{\lambda=400}^{700} R_c(\lambda) y(\lambda) P(\lambda) \tag{29}$$

$$Z = k \sum_{\lambda=400}^{700} R_c(\lambda) z(\lambda) P(\lambda) \tag{30}$$

where

$$k = \frac{100}{\sum_{\lambda=400}^{700} y(\lambda) P(\lambda)} \tag{31}$$

and *x(λ), y(λ), and z(λ)* are the color-matching functions for the CIE 1931 2° standard observer. The function *P(λ)* describes the CIE D50 standard illuminant. The XYZ values were then transformed in the sRGB (standard computer monitor RGB values, IEC 61966-2-1) using the MATLAB OptProp toolbox (by Wagberg Jerker, More Research & DPC, Sweden).

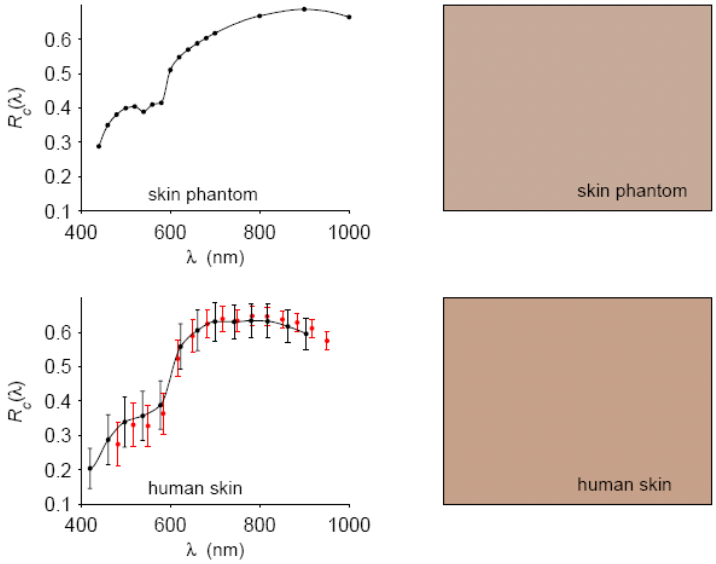

Figure 25. Reflectance spectra ($R_c(\lambda)$) for the numerical skin phantom (upper panel) and typical human skin (lower panel). The two sets of data (black and red dots) for real human skin were obtained from the literature (Lualdi, et al., 2001; Marchesini and Carrara, 2007). Bars represent the standard deviation. The two boxes to the right represent the skin color obtained by computing the tristimulus values from the reflectance spectra (black dot data) over the standard 400-700 nm range. The computer cluster time utilized to obtain the skin phantom $R_c(\lambda)$ data was 649 hours.

It is common to compare $R_c(\lambda)$ values and skin color for the phantom and real human skin (Urso, et al., 2007). Figure 25 shows a typical *in vivo* reflectance spectra on the bottom left. The variation of $R_c(\lambda)$ may be large for humans (Edwards and Duntley, 1939), but for this study it was enough that the numerical phantom represented the average of that curve. To check the results, two mean spectra of Caucasian subjects were obtained from previous work (Lualdi, et al., 2001; Marchesini and Carrara, 2007; Tomatis, et al., 2005) (black data is 260 measurements and red data is 1391 measurements). Both datasets were obtained during typical clinical pigmented skin lesion detection. Figure 25 shows that the skin color of the previous work and our phantom are very similar and the phantom $R_c(\lambda)$ values reasonably represent the previous work. Only the first set of data was used to calculate skin color. It is interesting to observe that even though the $R_c(\lambda)$ measurement techniques weren't the same, the two sets of data were quite similar. For both sets, the female/male ratio was nearly 3:2 and $R_c(\lambda)$ data were obtained 60% at trunk level, 35% on the legs, and 5% on head and neck, taking into account the extreme large inter- and intra-subject variability found in humans even if they belong to the same race (Edwards and Duntley, 1939).

It is interesting to note that the V_{mel} values (2%) and the $\mu_a^{mel}(\lambda)$ spectrum utilized in the present phantom were roughly estimated by Jacques (http://omlc.ogi.edu/, Jacques and McAuliffe 1991) to represent a light-skinned adult. It appears from the estimated color that this value reproduces as a more moderately pigmented adult, but considering the large variability of V_{mel} values (up to one order

of magnitude difference) and the difficulty to measure $\mu_a^{mel}(\lambda)$, the estimation made by Jacques was not far from reality and gives very reasonable results.

Even if the present phantom appears to be a suitable tool allowing one to study photon propagation in skin and the process of multi-spectral image generation, it must be noted that for more sophisticated simulations, more precise optical parameters should be used. For example, *n* values for biological tissue have a tendency to decrease with increasing wavelength (Bolin, et al., 1989; Friebel and Meinke, 2005). Taking into account this property would certainly improve the quality of the simulated $R_c(\lambda)$; but unfortunately, to our knowledge, these values have not yet been measured for the investigated human tissues.

6.4.2 3D Information Contained in One Detection Pixel

Figure 26 represents the number of photon packets (weights) that visited a given pixel before reaching the detector (expressed as a percentage of the number (weights) of packets reaching the detector):

$$N_\lambda^{\%}(i_x, i_y, i_z) = 100 \frac{N_\lambda(i_x, i_y, i_z)}{N_\lambda^{\det ect}} \qquad (32)$$

The values $N_\lambda^{\%}(i_x, i_y, i_z)$ represent a 3D matrix and Figure 26 shows a mean of three (*x,z*)-slices (i.e. three consecutive i_y values; see equation 26 for the conversion from i_x, i_y, *and* i_z to *x, y, and z*) giving a total slice thickness of 750 µm centered at *y*=25 mm (i.e. (*x,z*)-plane passing at the center of the detection pixel). Because a photon packet may visit the same voxel many times before reaching the detector, $N_\lambda^{\%}(i_x, i_y, i_z)$ may have values larger than 100%. The different panels appearing in Figure 26 correspond to the different wavelengths investigated in the simulations. For increased clarity, the

$N_\lambda^{\%}(i_x, i_y, i_z)$ values were plotted on a logarithmic scale to allow simultaneous viewing of the few pixels that have very high percentage values (near the detector) and the majority of the pixels that have low values. Pixels with zero or very low $N_\lambda^{\%}(i_x, i_y, i_z)$<0.1% values (threshold) are shown in black. The two horizontal white lines define the upper and lower limits of the dermis (all dermal layers were included). From Figure 26, it appears that the volume visited by the photons doesn't seem to strongly depend on wavelength.

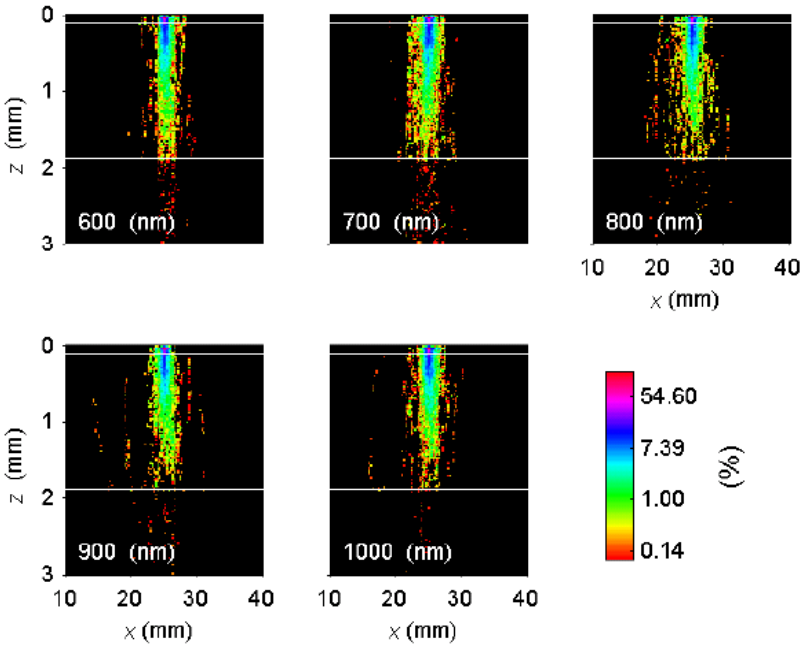

Figure 26. Percentage of photons that visit a given pixel at position (*x,z*) and that reach the detection pixel centered at *x*=0. The image represents an (*x,z*) cut of the phantom for *y*=0. The computer cluster time utilized to obtain the data appearing in the figure was 288 hours.

Moreover, 2 mm seems to be the limit of photon penetration for this theoretical instrumental setup – the photons mainly remain in the epidermis and dermis. It is interesting to notice that the voxels visited by the majority of the photons

appear to be situated vertically and symmetrically under the detection pixel. In practice, this means that an image formed at the skin surface should mainly carry information about the tissue situated directly under each pixel. Knowing that the information contained in the detection pixel mainly comes from tissue situated under its position, it is interesting to investigate the extension covered by the photons in the (*x,y*)-plane (at a fixed depth *z*).

Figure 27 shows an (*x,y*)-plane representing the $N_{\lambda}^{\%}(i_x, i_y, i_z)$ data for *z*≈375 µm (i.e. 375 µm under the skin surface), for the different λ values (position (*x,y*) = (25,25) mm is the center of the detector pixel). In this case the plane is a mean of three slices giving a total slice thickness of 60 µm. Similar figures are found if the depth is varied (only the disk size changes).

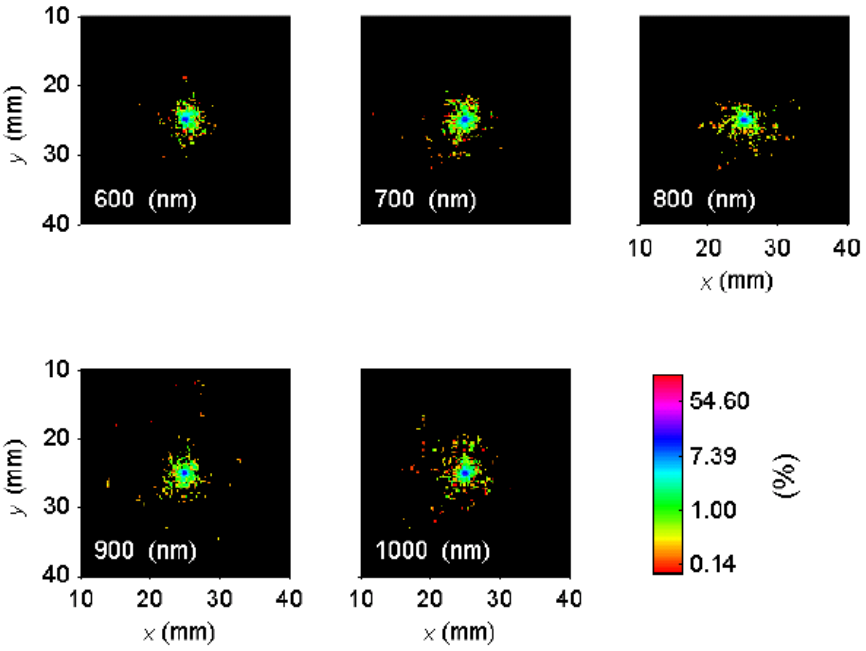

Figure 27. Percentage of photons that visit a given pixel at position (*x,y*) and *z*≈375 µm and that reach the detection pixel centered at (*x,y*)=(0,0). The image represents a (*x,y*) cut of the volume visited by the photons.

To better quantify the previous observations, two facts must be realized: the problem has a clear cylindrical symmetry and it appears that the highest $N_\lambda^{\%}(i_x,i_y,i_z)$ values are at the center (along the *z* axis) and they decrease when moving away from this position for any fixed *z* value. This means that if one chooses on an (*x,y*)-plane a set of $N_\lambda^{\%}(i_x,i_y,i_z)$ smaller than a given max value, one theoretically defines a disk (surface). This disk is obviously noisy; however, it is easy to estimate its surface and its mean radius. This radius defines the region (rotation of the radius around the axis) where the $N_\lambda^{\%}(i_x,i_y,i_z)<max$ values are situated, for a given *z* depth, under the skin surface. If we repeat the operation for all possible slices, an idea of the volume (rotation volume) visited by a percent of photon packets $N_\lambda^{\%}(i_x,i_y,i_z)<max$ can be obtained. In practice, the mean surface at a given depth, *z*, (and a given λ) is obtained by:

$$s_\lambda^{\max}(z_0)=\sum_{N_\lambda^{\%}(i_x,i_y,i_z)<\max}\Delta x\Delta y \qquad (33)$$

and the mean radius is expressed as:

$$r_{mean}(z)=\left(\frac{s_\lambda^{\max}(z)}{\pi}\right)^{1/2} \qquad (34)$$

These equations allow Figure 28 to be obtained from the $N_\lambda^{\%}(i_x,i_y,i_z)$ data. It clearly appears that the skin region visited by the highest percentage of photon packets is situated near the surface (black color). At a depth lower than 1 mm, the $N_\lambda^{\%}(i_x,i_y,i_z)$ values drastically decrease less than 5%. It is also interesting to note that the dermis/hypodermis interface (green line situated at ~2 mm) appears to be a photon barrier. In other words, if a pathological inclusion is located in the fat layer, it

will probably not be seen by the spectral imager. The differences due to wavelength are not very large. By rotating the different figures around the z axis, the mean volume visited by the photon could be obtained (i.e. the volume seen by the detection pixel).

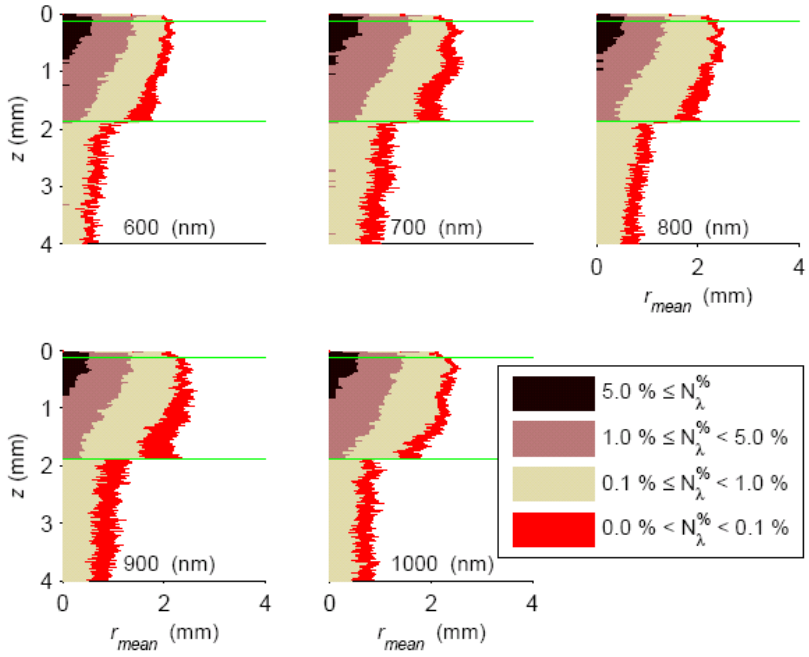

Figure 28. Percentage of photons that visit a given pixel at position (x,z) and that reach the detection pixel centered at x=0. The difference from Figure 26 is that in this case the regions defining the percentages are mean values obtained by exploiting the cylindrical symmetry of the problem. The interface created by the dermis and fat layers seems to act as a kind of firewall and causes a sudden decrease in the detected photons having visited the tissue beyond this depth.

The most exciting result in this simulated experiment is the fact that the information collected by a general pixel, positioned at the skin surface (i.e. detected by a CCD in a real spectral imager), mainly comes from a tissue region of interest that is situated just vertically under the pixel itself. In fact, this is not a trivial result, because as it is well known, in the case of a unique pair (point source, detection

pixel), the information comes from a banana-shaped region joining the source and detector and going to a depth that is approximately half the distance between the two points (Gandjbakhche and Weiss, 2000). In the present case, one has the equivalent of one detection pixel and an infinite number of point-like sources distributed over a disk centered on this pixel (configuration of Figures 24A and C). This means that one expects the detector to collect the information of an infinite number of banana-shaped trajectories where the origins (light sources) may also be situated very far from the detector (i.e. the borders of the disk, Figure 24A) and thus outside the vertical (*z* axis) of this pixel. In practice, this would create completely useless images. Fortunately, the present results show that the information coming far from the detection pixel is completely negligible and that the majority of the photons visit a region situated vertically just under the pixel.

6.4.3 Detection of Pathological Inclusion

Figure 29 reproduces the images of the phantom obtained with the virtual spectral imager with a 10x10x0.5 mm inclusion located 20 μm under the skin surface. The inclusion is perfectly visible at all wavelengths and appears to be the correct size. However, it must be noted that even if the hemoglobin content is higher in the inclusion compared to the background tissue, its intensity on the image is not decreased (i.e. higher light absorption), but is instead increased. The different contrasts between the background tissue and the inclusion show wavelength dependence in the images. This may be explained by the fact that the increased volume fraction of hemoglobin is compensated by an equal decrease in volume of melanosomes. In fact, the inclusion is situated just under the stratum corneum and its

thickness of 0.5 mm on top of the epidermis where the melanin is present. Hemoglobin has μ_a values lower than melanosomes and thus fewer photons are absorbed. As a consequence, more photons can reach the detector and increase the intensity of the image.

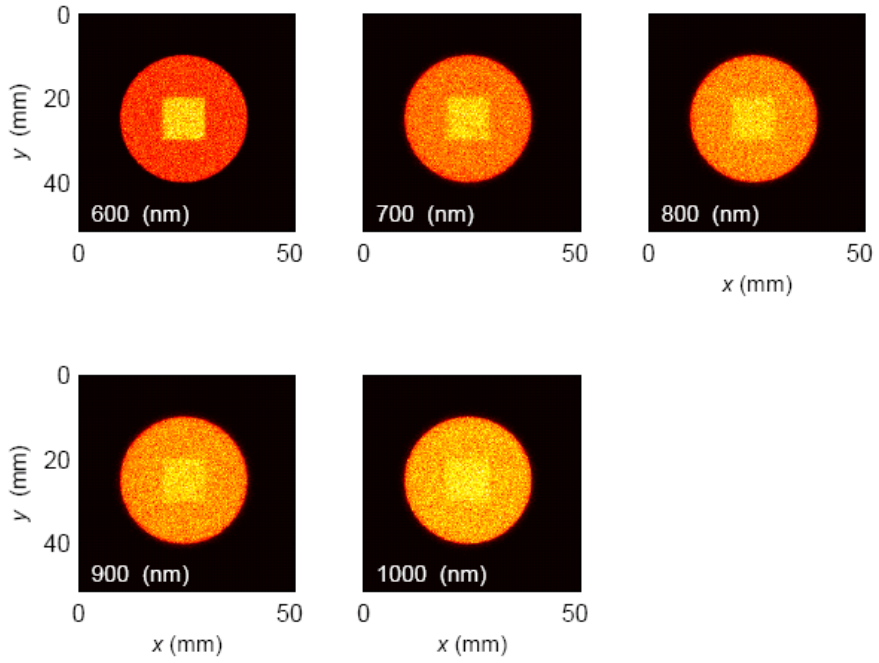

Figure 29. Images obtained at different wavelengths (λ) for a skin phantom containing an inclusion of 10x10x0.5 mm situated 20 µm under the skin surface (just under the stratum corneum). The computer cluster time utilized to obtain these data was 181 hours.

It is clear from Figure 30 that the contrast is lower (inclusion is less visible) for the inclusion at a depth of 520 µm. The two curves appearing on the same graph (circles and squares symbols) show that the image contrast (i.e. the percent of red surface compared to the brown on the bar graph) decreases for increasing wavelength for the 20 µm depth inclusion; however, it slightly increases for the inclusion at a depth of 520 µm. The 20 µm depth case may be explained because $\mu_a^{mel}(\lambda)$ is larger for short wavelengths and monotonically decreases with increasing wavelength and

thus also the effect of the contrast is lower at longer wavelengths. At the 520 μm depth, the inclusion cannot replace melanin because it is outside the epidermal region, and thus the effect may be due to the combined increase in hemoglobin and decrease in water, but in this case the intuitive interpretation is more difficult. The important conclusion here, is that one must be careful when interpreting spectral images because the same change in chromophore content may generate a completely different behavior on the image contrast depending on the type of tissue (layer) and where the change is situated (this is added to the influence of the depth).

To evaluate the change in image contrast occurring between the inclusion and the skin when varying wavelength and inclusion depth, the mean pixel intensities, $\overline{N}_{\lambda}^{\det ect}$, of these two regions were calculated. These values were obtained for the two phantom configurations (inclusions at depths of 20 and 520 μm). Figure 30 shows the computed $\overline{N}_{\lambda}^{\det ect}$ values as a function of wavelength and depth. The pixels were obviously chosen in the inclusion/skin zones where the values were constant. Note that the skin $\overline{N}_{\lambda}^{\det ect}$ value does not change when varying the inclusion depth. To facilitate the analysis in Figure 30, the percent difference in intensity between the skin background and the inclusion, $\Delta\overline{N}_{\lambda}^{\det ect}$, was calculated with the skin utilized as a reference (100%):

$$\Delta\overline{N}_{\lambda}^{\det ect} = 100\frac{\Delta\overline{N}_{\lambda}^{\det ect}(skin) - \Delta\overline{N}_{\lambda}^{\det ect}(inclusion)}{\Delta\overline{N}_{\lambda}^{\det ect}(skin)} \quad (35)$$

In the case of the phantom with an inclusion at a depth of 20 μm, $\Delta\overline{N}_{\lambda}^{\det ect}$ decreased with increasing wavelength, while it slightly increased in the case of the inclusion at a depth of 520 μm. The constraints imposed by the definition of the model must still be

considered. In fact, it is easy to deduce that the parameters V_{blood}, V_{water}, and γ must satisfy the following inequality:

$$V_{water} \geq V_{water}^{\min} = \frac{(1-\gamma)V_{blood}}{1-\gamma V_{blood}} \tag{36}$$

The chosen V_{blood} values utilized for this experiment were compatible with this equation.

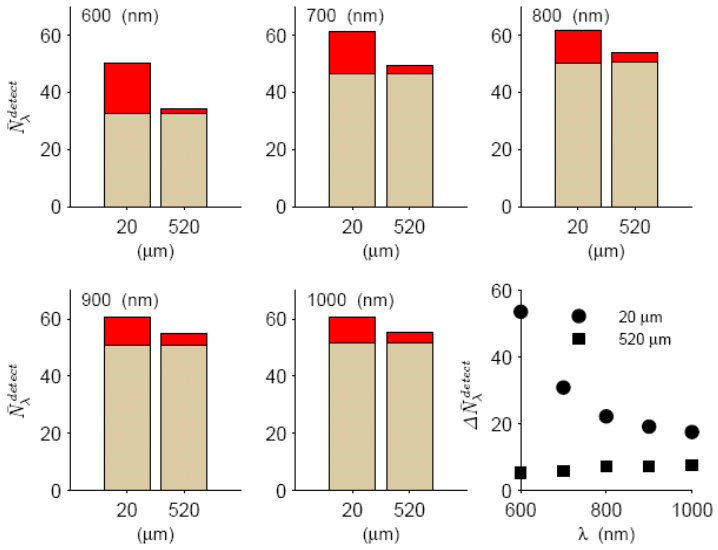

Figure 30. The stacked bars at 20 μm (and at different wavelengths) are derived from the data appearing in Figure 29 and correspond to the mean number of photons packets, $\overline{N}_\lambda^{\det ect}$, reaching a pixel situated in the region where the inclusion is visible (red) and to the same quantity but for a pixel over the skin (brown, lower values). The same representation is made for the same inclusion located at a depth of 520 μm. The circles and the squares represent percentage differences between the intensities, $\Delta\overline{N}_\lambda^{\det ect}$, of the skin and of the inclusion, for the 20 and 520 μm configurations (percent derived from the bar plots data). This gives an idea of the change in the image contrast of the inclusion compared to the skin when changing wavelength and inclusion depth.

The findings remain true in general for $\lambda \in [600,1000]$, but in the case of real skin tissue it is probably necessary to take into account other phenomena. In fact, in

the present model the μ_s' values of the different layers remained fixed, with or without an inclusion (with the exception of $\mu_s'^{hypodermis}(\lambda)$). However, a change in hemoglobin content will also probably vary μ_s' (Friebel, et al., 2006), but this is a very difficult measurement to assess experimentally and further studies are necessary.

6.4.4 Optical Skin Phantom

The optical phantom representing human skin allowed us to perform the necessary simulations, but a few things should be considered for future finer analyses. First, it was sufficient in the present work to consider a simple layered structure (with and without an inclusion). However, to be more realistic or personalize the phantom for a given subject, 3D images obtained by noninvasive techniques such as optical coherence tomography (OCT), microscopy, magnetic resonance imaging (MRI), or by invasive, but more precise, direct morphological analyses of biopsies (Pfefer, et al., 1999) could improve the results. Some researchers have also tried to take into account the influence of rough surfaces on photon propagation (e.g. epidermal ridges) (Meglinsky and Matcher, 2001). However, in this case it becomes very difficult to describe this geometry by a simple 3D matrix representation because computational artifacts due to boundary voxelization may occur. In some extreme cases, where the reflectance must be evaluated with precision, the presence of hair should also be considered (Poirier, 2003). From the above considerations, it appears that combining these morphological, physiological, and optical constraints into one unique code becomes a real technical undertaking that could be tremendously demanding on CPU time. However, this may certainly prove to be interesting future work.

Taking into account even the small morphological features certainly improves the model, but in this case it becomes necessary to know the related optical parameters of each defined tissue structure. Unfortunately, *g, n,* μ_a*, and* μ_s' values for human skin are scarcely reported and often only reported as mean values of mixed morphological structures. This is one reason why the epidermis has been reported as a unique mean layer in the Meglinski and Matcher model, whereas the real morphological substructure does not appear this way.

In this same context, one must also note that *g* and *n* should depend on wavelength but they are usually inserted in the biological human models as constant parameters due to the poor knowledge of their *in vivo* values (see Table 6). The same problem may be mentioned for μ_s'; however, in the present work, it was possible to consider the wavelength dependence in the case of the hypodermis because of the work completed by Bashkatov, et al. (2005).

More information is available regarding the absorption parameters, μ_a, because they represent pure chromophores that can be more easily studied *in vitro*. However, among the μ_a utilized for the skin phantom, one of them still remains problematic to determine, $\mu_a^{mel}(\lambda)$. There are many reasons why, but two in particular. The most obvious is due to the very large range of skin melanin concentrations found in humans (up to one order of magnitude differences). This is not only due to obvious racial differences, but also to inter-individual variations such as anatomical position (Edwards and Duntley, 1939), use of drugs, chemicals, the hormonal status of the subject (Costin and Hearing, 2007), aging (Ünver, et al., 2006), etc. The second reason is the fact that melanin is not freely distributed in the

tissue cells, but is instead tightly packed inside small vesicles called melanosomes (Hach, et al., 1993) and their quantification is difficult. Thus, from the physiological point of view, the skin melanin content (related to $\mu_a^{mel}(\lambda)$), depends on two intimately interconnected factors: skin concentration of melanosomes and the melanin content of the melanosomes. The melanin/melanosome couple form an interconnected system regulated by complex biochemical mechanisms (Hearing, 2005). To take that into account, even in a very simplified manner and to create a more realistic and flexible phantom, the melanosome tissue fraction, V_{mel}, was introduced as a parameter. The problem was then to define $\mu_a^{mel}(\lambda)$ because it was not clear if the free melanin had the same optical properties as the packet molecules inside the melanosomes. For this reason, $\mu_a^{mel}(\lambda)$ was considered a single melanosome instead of a melanin molecule. This approach was originally proposed in experiments by Jacques and McAuliffe (1991) and given a $\mu_a^{mel}(\lambda)$ value that holds for a typical melanosome and thus does not take into account the possible physiological changes of melanin content inside the melanosome (Borovansky, et al., 1991). The advantage is that it expresses $\mu_a^{mel}(\lambda)$ of the packed melanin and thus, theoretically, it directly takes into account the possible optical changes due to the influence of the spatially confined nature of the molecule. The use of a typical $\mu_a^{mel}(\lambda)$ parameter is also compatible with the fact that one tries to define a mean optical skin phantom. In this case it would be completely useless to use a different $\mu_a^{mel}(\lambda)$ for every subject. However, the use of the $\mu_a^{mel}(\lambda)$ melanosome value (Jacques and McAuliffe, 1991) has the drawback that it does not allow one to make the distinction between

eumelanins and phaeomelanins. Thus, for the present work, melanosome distribution was considered to be only uniformly distributed in the living epidermis and no finer representations were attempted, but could be (for example the case of senile lentigo where some melanin is observed also in the dermis (Ünver, et al., 2006)). Other chromophores present in the skin, such as β-carotene or bilirubin, were not considered, but should be for other applications such as the simulation of skin color in the case of jaundice, etc. (Krishnaswamy and Baranosky, 2004).

6.5 Conclusions

The present work has shown that the optical/biological information contained in a typical spectral image mainly reflects the properties of a small (conic like) volume of tissue situated vertically under each individual pixel. The consequence of this observation is that the objects appearing on the spectral images reasonably reproduce the correct geometrical shapes and size (like a non-deformed shadow) of underlying inclusions of pathological tissue. The negative consequence of this light propagation behavior is that the photons reaching the detectors (pixels) do not go very deep and thus the information contained in the spectral images comes from a depth that does not exceed ~2-3 mm. The number of photons that visit a given tissue voxel situated at a depth larger than approximately 2 mm represent less than the 1% of the total number of photons reaching the corresponding detection pixel (forming the image). The situation is even worse if one thinks that a photon can visit a voxel many times and thus some voxels may have a percent of visits that is higher than 100%. This means that in practice the 1% value just given above is certainly smaller in terms of the contribution to the electrical signal generated by the detector of a real spectral

imager. This way to represent the percentages has not been reported in the figures because it's more complex to understand. The interface defined by the dermis/hypodermis layers seems to behave as a partial firewall for the photons, making their access to deep skin regions difficult.

It has also been shown that a pathological inclusion (increased blood pool) situated at a depth of 520 μm with a thickness of 0.5 mm produces an image intensity contrast of ~5% (for λ=600 nm) when compared to the normal skin background (100%). Considering that the contrast for the same inclusion situated at a depth of 20 μm is ~55% (for λ=600 nm), this means that at a depth of 1 mm, this inclusion will be very difficult to detect with the imager at least for $\lambda \in [600,1000]$.

This highlights the fact that the image contrast strongly depends on the type of chromophore contained in the inclusion and that an increase of the concentration of a given molecule may produce different contrasts depending on the skin layer where this change occurs. This observation demonstrates that a simple interpretation of the images is very difficult. However, the relatively similar region spanned by the photons at different λ (not absolute intensity values but percentages, e.g. Figure 28) should permit others to develop suitable algorithms that allow them to mathematically extract the desired biological information.

The present study also shows that it is absolutely necessary to improve our knowledge of human tissue optical parameters by means of experimental measurements in order to realize reliable and more precise phantoms allowing researchers to test and develop new instrumentation and algorithms. With the present knowledge, the phantom proposed in the present work is unfortunately not too far

from their maximum capabilities (in terms of optical parameters) and better models are needed.

It may also be interesting to note that the results found for the spectral imager model may also be useful for other domains. In fact, recent developments in laser Doppler flowmetry for human skin use very similar illumination and detection techniques (Briers, 2001). The present results may also give some useful information concerning the interpretation of the laser Doppler signals.

Chapter 7: Conclusions

The overall objectives of this research described in Chapter 2 have been achieved. The following conclusions were drawn from the research:

1. Thermography showed statistically significant changes in the temperature difference between the lesion and surrounding skin before and after experimental therapy. LDI analysis showed there was a statistically significant change in blood flow in the lesion and surrounding skin after experimental therapy.
2. NIR multi-spectral imaging was able to show changes in HbO_2 and blood volume between the lesion and surrounding areas. The results after experimental therapy correlated well with the clinical assessment, but added quantitative information.
3. Monte-Carlo simulations showed that the optical/biological information contained in a typical spectral image mainly reflects the properties of a small (conic like) volume of tissue situated vertically under each individual pixel. The photons reaching the detectors (pixels) do not go very deep and thus the information contained in the spectral images comes from a depth that does not exceed ~2-3 mm.

Thermography, LDI, and multi-spectral imaging techniques can be used as quantitative methods to assess the response of skin to experimental therapies. Ultimately, these quantitative imaging methods can be applied to other tumors or lesions involving the skin or other easily accessible tissues.

Chapter 8: Suggestions for Further Study

Images from thermography, LDI, and NIR multi-spectral imaging are quantitative, easy to collect, and appear to be very sensitive in assessing progress of KS lesions upon administration of therapy. Based on the data in this dissertation, one or more of these techniques (probably a combination of them) will have utility in monitoring the vascular abnormalities in KS lesions and the changes with therapies. However, there are improvements that can be made to move these promising techniques to the bedside. Suggestions for further study include:

1. Continuing to collect images from the NIH clinical protocols using the three imaging techniques. Collecting additional images will allow analyses of response to treatment to be conducted for later dates (such as 46 week follow-ups).
2. Improving knowledge of human tissue optical parameters by conducting experimental measurements that will help create reliable and more precise phantoms allowing researchers to test and develop new instrumentation and algorithms.
3. Developing an additional algorithm to remove the hair from the multi-spectral images and improving the curvature removal algorithm.
4. Expanding the multi-spectral mathematical optical skin model to include the contributions from water and lipids (fat), thus allowing the longer wavelengths to be utilized and additional parameters to be solved for.
5. Utilizing a digital wavelength tuner so that any wavelength can be considered, not just the six pre-selected filters.

6. Designing and constructing an integrated system with all three imaging modalities in one portable system to assess tumor vascularity quantitatively at the patient's bedside. Currently, each imager requires floor space and a computer and takes images separately. The angle of image capture is different for each system; however, in the new system, image registration can be included in the system hardware so that time will not be needed to do image registration. Moreover, patients do not want to sit still while we take images with the thermography system, move it away, take images with the LDI, move it away, and then take images with the multi-spectral imager. The time to take these measurements can be much shorter if the images can be captured at the same time; this should be possible if all three imagers are on the same cart and are controlled by the same computer.
7. Exploring angiogenic parameters in other tumors and conditions using the three imaging techniques.

Bibliography

Anbar, M. 1998. Clinical thermal imaging today. *IEEE Eng Med Biol Mag*, 17:25-33.

Andersen, P. and P. Bjerring. 1990. Noninvasive computerized analysis of skin chromophores *in vivo* by reflectance spectroscopy. *Photodermatol Photoimmunol Photomed*, 7:249-257.

Anderson, R. R. and J. Parrish. 1981. The Optics of Human Skin. *J Investigative Dermatology*, 77:13-19.

Angelopoulou, E. 2001. Understanding the Color of Human Skin. In *Proceedings of the SPIE Conference on Human Vision and Electronic Imaging VI*, 243-251.

Antman, K. and Y. Chang. 2000. Kaposi's sarcoma. *New Engl J Med*, 342:1027-1038.

Archambeau, J. O., A. Ines, and L. F. Fajardo. 1985. Correlation of the Dermal Microvasculature Morphology with the Epidermal and the Endothelial Population Changes Produced by Single X Ray Fractions of 1649, 2231 and 2619 rad in Swine. *Int J Radiat Oncology Biol Phys*, 11:1639-1646.

Archambeau, J. O., R. Pezner, and T. Wasserman. 1995. Pathophysiology of Irradiated Skin and Breast. *Int J Radiat Oncology Biol Phys*, 31:1171-1185.

Arnfield, M. R., J. Tulip, and M. S. McPhee. 1988. Optical propogation in tissue with anisotropic scattering. *IEEE Trans Biomed Eng*, 35:372-381.

Attas, M., M. Hewko, J. Payette, T. Posthumus, M. Sowa, and H. Mantsch. 2001. Visualization of cutaneous hemoglobin oxygenation and skin hydration using near-infrared spectroscopic imaging. *Skin Research and Technology*, 7:238-245.

Bais, C., B. Santomasso, O. Coso, L. Arvanitakis, E. G. Raaka, J. S. Gutkind, A. S. Asch, E. Cesarman, M. C. Gershengorn, E. A. Mesri, and M. C. Gerhengorn. 1998. G-protein-coupled receptor of Kaposi's sarcoma-associated herpesvirus is a viral oncogene and angiogenesis activator. *Nature*, 391:86-89.

Bashkatov, A., E. Genina, V. Kochubey, and V. Tuchin. 2005. Optical properties of human skin, subcutaneous and mucous tissues in the wavelength range from 400 to 2000 nm. *J Phys D: Appl Phys*, 38 2543-2555.

Beral, V., T. A. Peterman, R. L. Berkelman, and H. W. Jaffe. 1990. Kaposi's sarcoma among persons with AIDS: a sexually transmitted infection? *Lancet*, 335:123-128.

Bolin, F., L. Preuss, R. Taylor, and R. Ference. 1989. Refractive index of some mammalian tissues using a fiber optic cladding method *J Appl Opt*, 28:2297-2303.

Bornmyr, S., H. Svensson, B. Lilja, and G. Sundkvist. 1997. Skin temperature changes and changes in skin blood flow monitored with laser Doppler flowmetry and imaging: a methodological study in normal humans. *Clin Physiol*, 17:71-81.

Borovansky, J., E. Vedralova, and P. Hach. 1991. An estimate of melanosome concentration in pigment tissues *Pigment Cell Res*, 4:222-224.

Boshoff, C., Y. Endo, P. D. Collins, Y. Takeuchi, J. D. Reeves, V. L. Schweickart, M. A. Siani, T. Sasaki, T. J. Williams, P. W. Gray, P. S. Moore, Y. Chang, and R. A. Weiss. 1997. Angiogenic and HIV-inhibitory functions of KSHV-encoded chemokines. *Science*, 278:290-294.

Briers, D. 2001. Laser Doppler, speckle and related techniques for blood perfusion mapping and imaging *Physiol Meas*, 22 R35-R66.

Bruls, W. A. and J. C. van der Leun. 1984. Forward Scattering Properties of Human Epidermal Layers. *Photochem Photobiol*, 40:231-242.

Canvin, J. M. G., S. Bernatsky, C. A. Hitchon, M. Jackson, M. G. Sowa, J. R. Mansfield, H. H. Eysel, H. H. Mantsch, and H. S. El-Gabalawy. 2003. Infrared spectroscopy: shedding light on synovitis in patients with rheumatoid arthritis. *Rheumatology*, 42:76-82.

Carmeliet, P. and R. K. Jain. 2000. Angiogenesis in cancer and other diseases. *Nature*, 407:249-257.

Chang, Y., E. Cesarman, M. S. Pessin, F. Lee, J. Culpepper, D. M. Knowles, and P. S. Moore. 1994. Identification of herpesvirus-like DNA sequences in AIDS-associated Kaposi's sarcoma. *Science*, 266:1865-1869.

Colier, W., I. Meeuwsen, H. Degens, and B. Oeseburg. 1995. Determination of oxygen consumption in muscle during exercise using near infrared spectroscopy. *Acta Anaesthesiol Scand*, 1995:151-155.

Comerota, A., R. Throm, P. Kelly, and M. Jaff. 2003. Tissue (muscle) oxygen saturation (StO2): a new measure of symptomatic lower-extremity aterial disease. *J Vasc Surg*, 38:724-729.

Conover, D. L., B. M. Fenton, T. H. Foster, and E. L. Hull. 2000. An evaluation of near infrared spectroscopy and cryospectrophotometry estimates of haemoglobin oxygen saturation in a rodent mammary tumour model. *Physics in Medicine & Biology*, 45:2685-2700.

Costin, G. and V. Hearing. 2007. Human skin pigmentation: melanocytes modulate skin color in response to stress. *FASEB J*, 21:976-994.

Dawson, J., D. Barker, D. Ellis, E. Grassam, J. Cotterill, G. Fisher, and J. Feather. 1980. A theoretical and experimental study of light absorption and scattering by in vivo skin. *Phys Med Biol*, 25:695-709.

Delpy, D. T., M. Cope, P. Vanderzee, S. Arridge, S. Wray, and J. Wyatt. 1988. Estimation of Optical Pathlength through Tissue from Direct Time of Flight Measurement. *Physics in Medicine and Biology*, 33:1433-1442.

Demos, S. and R. Alfano. 1997. Optical Polarization Imaging. *Applied Optics*, 36:150-155.

Douven, L. F. A. and G. W. Lucassen. 2000. Retrieval of optical properties of skin from measurement and modelling the diffuse reflectance. In *Laser-Tissue Interaction XI: Photochemical, Photothermal, and Photomechanical*, 312-323.

Draper, J. and J. Boag. 1971. Skin Temperature Distributions Over Veins and Tumours. *Phys Med Biol*, 16:645-654.

Duck, F. 1990. Physical properties of tissue: a comprehensive reference book. London: Academic Press.

Edwards, E. and Q. Duntley. 1939. The pigments and color of living human skin *Am J Anat*, 65:1-33.

Egley, C. C., J. W. Seeds, and R. C. Cefalo. 1987. Single-Probe Spectrophotometry in the Assessment of Fetal Oxygenation. *Obstet Gynecol*, 70:726-728.

Ensoli, B., G. Barillari, and R. C. Gallo. 1992. Cytokines and growth factors in the pathogenesis of AIDS-associated Kaposi's sarcoma. *Immunol Rev*, 127:147-155.

Feather, J., D. Ellis, and G. Leslie. 1988. A portable reflectometer for the rapid quantification of cutaneous haemoglobin and melanin. *Phys Med Biol*, 33:711-722.

Ferguson-Pell, M. and S. Hagisawa. 1995. An empirical technique to compensate for melanin when monitoring skin microcirculation using reflectance spectrophotometry. *Med Eng Phys*, 17:104-110.

Ferrara, K., C. Merritt, and P. Burns. 2000. Evaluation of Tumor Angiogenesis with US: Imaging, Doppler, and Contrast Agents. *Acad Radiol*, 7:824-839.

Firbank, M., M. Oda, and D. T. Delpy. 1995. An improved design for a stable and reproducible material for use in near-infrared spectroscopy and imaging. *Phys Med Biol*, 40:955-961.

FLIR (2002). Thermography. [Online]. Available WWW:http://www.flirthermography.com.

Folkman, J. 2002. Role of angiogenesis in tumor growth and metastasis. *Semin Oncol*, 29:15-18.

Fredriksson, A. and S. Stone-Elander. 2003. PET Screening of Anticancer Drugs. A Faster Route to Drug/Target Evaluations In Vivo. *Methods Mol Med*, 85:279-294.

Freeman, R. G., E. G. Cockerell, J. Armstrong, and J. M. Knox. 1962. Sunlight as a factor influencing the thickness of epidermis. *J Investigative Dermatology*, 39:295-298.

Friebel, M. and M. Meinke. 2005. Determination of the complex refractive index of highly concentrated hemoglobin solutions using transmittance and reflectance measurements. *J Biomed Opt*, 10:064019.

Friebel, M., A. Roggan, G. Muller, and M. Meinke. 2006. Determination of optical properties of human blood in the spectral range 250 to 1100 nm using Monte Carlo simulations with hematocrit-dependent effective scattering phase functions. *J Biomed Opt*, 11:34021.

Gandjbakhche, A. H., Weiss, G. H. 1995. Random walk and diffusion-like models of photon migration in turbid media. *Progress in Optics*, XXXIV:335-402.

Gandjbakhche, A. and G. Weiss. 2000. Descriptive parameter for photon trajectories in a turbid medium. *Phys Rev*, E61:6958-6962.

Ge, Z., K. T. Schomacker, and N. S. Nishioka. 1998. Identification of colonic dysplasia and neoplasia by diffuse reflectance spectroscopy and pattern recognition techniques. *Appl Spectrosc*, 52:833-839.

Giannotti, G., S. Cohn, M. Brown, J. Varela, M. McKenny, and J. Wiseberg. 2000. Utility of near-infrared spectroscopy in the diagnosis of lower extremity compartment syndrome. *J Trauma*, 48:396-401.

Gill, E., G. Palmer, and N. Ramanujam. 2003. Steady-state fluorescence imaging of neoplasia. *Methods Enzymol*, 361:452-481.

Goertz, D., D. Christopher, and J. Yu. 2000. High-frequency Color Flow Imaging of the Microcirculation. *Ultrasound Med Biol*, 26:63-71.

Goldzieher, J., I. Roberts, W. Rawls, and M. Goldzieher. 1951. "Chemical" Analysis of the Intact Skin by Reflectance Spectrophotometry. *AMA Archives of Dermatology and Syphilology*, 64:533-548.

Graaff, R., A. C. M. Dassel, W. G. Zijlstra, F. F. M. de Mul, and J. G. Aarnoudse. 1996. How Tissue Optics Influences Reflectance Pulse Oximetry. *Oxygen Transport to Tissue XVII*. New York: Plenum Press.

Hach, P., J. Borovansky, and E. Vedralova. 1993. Melanosome - a sophisticated organelle *Sborník Lekarsky*, 94:113-123.

Hajizadeh-Saffar, M., J. Feather, and J. Dawson. 1990. An investigation of factors affecting the accuracy of *in vivo* measurements of skin pigments by reflectance spectroscopy. *Phys Med Biol*, 35:1301-1315.

Hassan, M., R. F. Little, A. Vogel, K. Aleman, K. Wyvill, R. Yarchoan, and A. Gandjbakhche. 2004. Quantitative Assessment of Tumor Vasculature and Response to Therapy in Kaposi's Sarcoma Using Functional Noninvasive Imaging. *Technology in Cancer Research & Treatment*, 3:451-457.

Hattery, D., M. Hassan, S. Demos, and A. Gandjbakhche. 2002. Hyperspectral Imaging of Kaposi's Sarcoma for Disease Assessment and Treatment Monitoring. *31st Applied Imagery Pattern Recognition Workshop*.

Head, J. F. and R. L. Elliott. 2002. Infrared imaging: making progress in fulfilling its medical promise. *IEEE Eng Med Biol Mag*, 21:80-85.

Hearing, V. 2005. Biogenesis of pigment granules: a sensitive way to regulate melanocyte function. *J Dermatol Sci*, 37:3-14.

Henyey, L. and J. Greenstein. 1941. Diffuse radiation in the galaxy. *Astrophys J*, 93:70-83.

Hopewell, J. W. 1990. The skin: its structure and response to ionizing radiation. *Int J Radiat Biol*, 57:751-773.

Hopper, K., K. Singapuri, and A. Finkel. 2000. Body CT and Oncologic Imaging. *Radiology*, 215:27-40.

Ikeda, M. and A. Matsushita. 1980. Reflectance of rat brain structures mapped by an optical fiber technique. *J Neurosci Methods*, 2:9-17.

Jacques, S. and D. McAuliffe. 1991. The melanosome: threshold temperature for explosive vaporization and internal absorption coefficient during pulsed laser irradiation. *Photochem Photobiol*, 53:769-775.

Jacques, S., J. Roman, and K. Lee. 2000. Imaging superficial tissues with polarized light. *Lasers in Surgery and Medicine*, 26:119-129.

Jacques, S. L. 1996. Origins of Tissue Optical Properties in the UVA, Visible, and NIR Regions. In *OSA TOPS on Advances in Optical Imaging and Photon Migration*, 364-371.

Jacques, S. L. (1998). Skin Optics. [Online]. Available WWW:http://omlc.ogi.edu/news/jan98/skinoptics.html.

Jain, R. K. 1988. Determinants of tumor blood flow: a review. *Cancer Res*, 48:2641-2658.

Jerusalem, G., R. Hustinx, and Y. Beguin. 2002. The Value of Postron Emission Tomography (PET) Imaging in Disease Staging and Therapy Assessment. *Ann Oncol*, 13:227-234.

Jobsis, F. F. 1977. Noninvasive infrared monitoring of cerebral and myocardial oxygen sufficiency and circulatory parameters. *Science*, 198:1264.

Kelch, C. a. R. J. S. (1998). Infrared Thermography for PPM. [Online]. Available WWW:http://www.mt-online.com/current/05-99amt01.html.

Kerker, M. 1969. The Scattering of Light and Other Electromagnetic Radiation. New York: Academic.

Kienle, A., L. Lilge, M. S. Patterson, R. Hibst, R. Steiner, and B. C. Wilson. 1996. Spatially resolved absolute diffuse reflectance measurements for noninvasive determination of the optical scattering and absorption coefficients of biological tissue. *Appl Opt*, 35:2304-2341.

Kirkby, D. and D. Delpy. 1997. Parallel operation of Monte Carlo simulations on a diverse network of computers. *Phys Med Biol*, 42:1203-1208.

Knoefel, W. T., N. Kollias, D. W. Rattner, N. S. Nishioka, and A. L. Warshaw. 1996. Reflectance spectroscopy of pancreatic microcirculation. *J Appl Physiol*, 80:116-123.

Kollias, N. 1986. On the assessment of melanin in human skin in vivo. *Photochem Photobiol*, 43:49-54.

Kollias, N. and A. Baqer. 1988. Quantitative assessment of UV-induced pigmentation and erythema. *Photodermatol*, 5:53-60.

Kollias, N., R. Gillies, J. A. Muccini, R. Uyeyama, S. Phillips, and L. Drake. 1995. A single parameter, oxygenated hemoglobin, can be used to quantify experimental irritant-induced inflammation. *Journal of Investigative Dermatology*, 104:421-424.

Kooijman, H. M., M. T. E. Hopman, W. N. J. M. C. colier, J. A. van der Vliet, and B. Oeseburg. 1997. Near Infrared Spectroscopy for Noninvasive Assessment of Claudication. *Journal of Surgical Research*, 72:1-7.

Kragelj, R., T. Jarm, T. Erjavec, M. Presern-Strukelj, and D. Miklavcic. 2001. Parameters of Postocclusive Reactive Hyperemia Measured by Near Infrared Spectroscopy in Patients with Peripheral Vascular Disease and in Healthy Volunteers. *Annals of Biomedical Engineering*, 29:311-320.

Kragelj, R., T. Jarm, and D. Miklavcic. 2000. Reproducibility of Parameters of Postocclusive Reactive Hyperemia Measured by Near Infrared Spectroscopy and Transcutaneous Oximetry. *Annals of Biomedical Engineering*, 28:168-173.

Kragsterman, B., H. Parsson, and D. Bergquist. 2004. Local haemodynamic changes during carotid endarterectomy--the influence on cerebral oxygenation. *Eur J Vasc Endovasc Surg*, 2004:4.

Krishnaswamy, A. and G. Baranosky. 2004. A biophysical-based spectral model of light interaction with human skin. *Eurographics*, 23:331-340.

Krown, S. E., M. A. Testa, and J. Huang. 1997. AIDS-related Kaposi's sarcoma: prospective validation of the AIDS Clinical Trials Group staging classification. AIDS Clinical Trials Group Oncology Committee. *J Clin Oncol*, 15:3085-3092.

Laufer, J., C. Elwell, D. Delpy, and P. Beard. 2005. *In vitro* measurements of absolute blood oxygen saturation using pulsed near-infrared photoacoustic spectroscopy: accuracy and resolution. *Phys Med Biol*, 50:4409-4428.

Leu, A. J., A. Yanar, J. Jost, U. Hoffmann, U. K. Franzeck, and A. Bollinger. 1994. Microvascular dynamics in normal skin versus skin overlying Kaposi's sarcoma. *Microvasc Res*, 47:140-144.

Levenberg, K. 1944. A Method for the Solution of Certain Non-Linear Problems in Least Squares. *Quart Appl Math*, 2:164-168.

Little, R. F., K. Aleman, F. Merced, K. Wyvill, A. Catanzaro, F. Maldarelli, S. M. Steinberg, and R. Yarchoan. 2003. Doxorubicin and interleukin-12 followed by interleukin-12 maintenance therapy in advanced AIDS-related Kaposi's sarcoma. In *10th Conference on Retroiviruses and Opportunistic Infections*, Abstract 816. Boston.

Little, R. F., K. M. Wyvill, J. M. Pluda, L. Welles, V. Marshall, W. D. Figg, F. M. Newcomb, G. Tosato, E. Feigal, S. M. Steinberg, D. Whitby, J. J. Goedert, and R. Yarchoan. 2000. Activity of thalidomide in AIDS-related Kaposi's sarcoma. *J Clin Oncol*, 18:2593-2602.

Love, T. J. 1980. Thermography as an indicator of blood perfusion. *Ann N Y Acad Sci*, 335:429-437.

Lualdi, M., A. Colombo, B. Farina, S. Tomatis, and R. Marchesini. 2001. A phantom with tissue-like optical properties in the visible and near infrared for use in photomedicine. *Lasers Surg Med*, 28:237-243.

Lucas, N. S. 1931. The permeability of human epidermis to ultra-violet irradiation. *Biochem J*, 25:57-70.

Mancini, D. M., L. Bolinger, H. Li, K. Kendrick, B. Chance, and J. R. Wilson. 1994. Validation of near-infrared spectroscopy in humans. *J Appl Physiol*, 77:2740-2747.

Mansfield, C., E. Attas, and R. Gall. 2005. Evaluation of static thermal and near-infrared hyperspectral imaging for the diagnosis of acute maxillary rhinosinusitis. *J Otolaryngol*, 34:99-108.

Marchesini, R., M. Brambilla, C. Clemente, M. Maniezzo, A. E. Sichirollo, A. Testori, D. R. Venturoli, and N. Cascinelli. 1991. *In vivo* spectrophotometric evaluation of neoplastic and non-neoplastic skin pigmented lesions. I. Reflectance measurements. *Photochem Photobiol*, 53:77-84.

Marchesini, R. and M. Carrara. 2007. L'maging spettrofotometrico de lesioni cutanee pigmentate. Alla ricerca non invasiva delle caratteristiche biofisiche di una lesione. *hitech dermo*, 3:43-50.

Marquardt, D. 1963. An Algorithm for Least-Squares Estimation of Nonlinear Parameters. *SIAM J Appl Math*, 11:431-441.

Marsaglia, C. and A. Zaman. 1991. A new class of ramdom number generators. *Ann Appl Prob*, 4:462-480.

Matas, A., M. Sowa, G. Taylor, and H. H. Mantsch. 2002. Melanin as a confounding factor in near infrared spectroscopy of skin. *Vibrational Spectroscopy*, 28:45-52.

Maxwell-Cade, C. 1968. Principles and practice of clinical thermography. *Radiography*, 34:23-34.

McDonald, D. M. and P. L. Choyke. 2003. Imaging of angiogenesis: from microscope to clinic. *Nat Med*, 9:713-725.

Meglinski, I. and S. Matcher. 2002. Quantitative assessment of skin layers absorption and skin reflectance spectra simulation in the visible and near-infrared spectral regions. *Physiol Meas*, 23:741-753.

Meglinski, I. and S. Matcher. 2003. Computer simulation of the skin reflectance spectra. *Comput Methods Programs Biomed*, 70:179-186.

Meglinsky, I. and S. J. Matcher. 2001. Modelling the sampling volume for skin blood oxygenation. *Medical & Biological Engineering & Computing*, 39:44-49.

Mercie, P., I. Devianne, J. F. Viallard, I. Faure, I. Pellegrin, B. Leng, M. Dupon, P. Barbeau, H. Fleury, and J. L. Pellegrin. 1999. Vascular endothelial growth factor (VEGF165) plasma level increase with immunodepression in AIDS patients with Kaposi's sarcoma. *Microvasc Res*, 57:208-210.

Merla, A., L. Di Donato, S. Di Luzio, and G.L. Romani. 2002. Quantifying the Relevance and Stage of Disease with the Tau Image Technique: A Complimentary Diagnostic Imaging Technique Based on Infrared Functional Imaging. *IEEE Engineering in Medicine and Biology*, 21:86-91.

Mille, T., M. Tachimiri, C. Klersy, G. Ticozzelli, G. Bellinzona, and I. Blangetti. 2004. Near infrared spectroscopy monitoring during carotid endarterectomy: which threshold value is critical? *Eur J Vasc Endovasc Surg*, 27:646-650.

Moore, P. S., C. Boshoff, R. A. Weiss, and Y. Chang. 1996. Molecular mimicry of human cytokine and cytokine response pathway genes by KSHV. *Science*, 274:1739-1744.

Mourant, J. R., I. J. Bigio, J. Boyer, R. L. Conn, T. Johnson, and T. Shimada. 1995. Spectroscopic diagnosis of bladder cancer with elastic light scattering. *Lasers Surg Med*, 17:350-357.

Mourant, J. R., I. J. Bigio, J. Boyer, R. L. Conn, T. M. Johnson, and J. Lacey. 1996. Elastic scattering spectroscopy as a diagnostic for differentiating pathologies in the gastrointestinal tract: preliminary testing. *J Biomed Opt*, 1:192-199.

Mourant, J. R., J. P. Freyer, A. H. Hielscher, A. A. Eick, D. Shen, and T. M. Johnson. 1998. Mechanisms of light scattering from biological cells relevant to noninvasive optical-tissue diagnostics. *Appl Opt*, 37:3586-3593.

Ng, C. S.-L. and L. Li. 2001. A Multi-Layered Reflection Model of Natural Human Skin. *Computer Graphics International 2001*, 249-256.

Nielsen, K. P., L. Zhao, P. Juzenas, J. Stamnes, K. Stamnes, and J. Moan. 2004. Reflectance Spectra of Pigmented and Nonpigmented Skin in the UV Spectral Region. *Photochem Photobiol*, 80 450-455.

Nishidate, I., Y. Aizu, and H. Mishina. 2003. Estimation of Absorbing Components in a Local Layer Embedded in the Turbid Media on the Basis of Visible and Near-Infrared (VIS-NIR) Reflectance Spectra. *Optical Review*, 10:427-435.

Odland, G. 1991. Chapter 1 Structure of the skin. In *Physiology, biochemistry, and molecular biology of the skin*. New York: Oxford Universiy Press.

Ono, K., M. Kanda, J. Hiramoto, K. Yotsuya, and N. Sato. 1991. Fiber optic reflectance spectrophotometry system for *in vivo* tissue diagnosis. *Applied Optics*, 30:98-105.

Payette, J., E. Kohlenberg, L. Leonardi, A. Pabbies, P. Kerr, K.-Z. Liu, and M. G. Sowa. 2005. Assessment of Skin Flaps Using Optically Based Methods for Measuring Blood Flow and Oxygenation. *Plastic and Reconstructive Surgery*, 115:539-546.

Pfefer, T., J. Barton, D. Smithies, T. Milner, J. Nelson, M. van Gemert, and A. Welch. 1999. Modeling laser treatment of port wine stains with a computer-reconstructed biopsy. *Lasers Surg Med*, 24:151-166.

Poirier, G. 2003. Human skin modelling and rendering. PhD. University of Waterloo.

Polanyi, M. L. and R. M. Hehir. 1962. *In Vivo* Oximeter with Fast Dynamic Response. *The Review of Scientific Instruments*, 33:1050-1054.

Prahl, S., M. Keijzer, S. Jacques, and A. Welch. 1989. A Monte Carlo code of light propagation in tissue. *Proc SPIE IS*, 5:102-111.

Rajadhyaksha, M., M. Grossman, D. Esterowitz, R. H. Webb, and R. R. Anderson. 1995. *In Vivo* Confocal Scanning Laser Microscopy of Human Skin: Melanin Provides Strong Contrast. *J Investigative Dermatology*, 104:946-952.

Reinertson, R. P. and V. R. Wheatley. 1959. Studies on the chemical composition of human epidermal lipids. *J Investigative Dermatology*, 32:49-59.

Rendell, M., E. Anderson, W. Schleuter, J. Mailliard, D. Honigs, and R. Rosenthal. 2003. Determination of hemoglobin levels in the finger using near infrared spectroscopy. *Clin Lab Haem*, 25:93-97.

Rivard, A., J. E. Fabre, M. Silver, D. Chen, T. Murohara, M. Kearney, M. Magner, T. Asahara, and J. M. Isner. 1999. Age-dependent impairment of angiogenesis. *Circulation*, 99:111-120.

Rockoff, S. 1977. The Evolving Role of Computerized Tomography in Radiation Oncology. *Cancer*, 39:694-696.

Roggan, A., M. Friebel, K. Dorschel, A. Hahn, and G. Muller. 1999. Optical properties of circulating human blood in the wavelength range 400-2500 nm. *J Biomed Opt*, 4:36-46.

Ryatt, K., J. Feather, J. Dawson, and J. Cotterill. 1983. The usefulness of reflectance spectrophotometric measurements during psoralens and ultraviolet A therapy for psoriasis. *J Amer Acad Derm*, 9:558-562.

Saidi, I. S. 1992. Transcutaneous optical measurement of hyperbilirubinemia in neonates. PhD. Rice University.

Sato, N., T. Kamada, S. Motoaki, K. Sunao, A. Hiroshi, and B. Hagihara. 1979. Measurement of hemoperfusion and oxygen sufficiency in gastric mucosa *in vivo.* Evidence of mucosal hypoxia as the cause of hemorrhagic shock-induced gastric mucosal lesion in rats. *Gastroenterology*, 76:814-819.

Scheuermann-Freestone, M., P. Madsen, D. Manners, A. Blamire, R. Buckingham, and P. Styles. 2003. Abnormal cardiac and skeletal muscle energy metabolism in patients with type 2 diabetes. *Circulation*, 107:3040-3046.

Schmitt, J. and G. Kumar. 1998. Optical scattering properties of soft tissue: a discrte particle model. *Appl Opt*, 37:2788-2797.

Schmitt, J. M. 1991. Simple photon diffusion analysis of the effects of multiple scattering on pulse oximetry. *IEEE Trans Biomed Eng*, 38:1194-1203.

Shah, N., A. Cerussi, C. Eker, J. Espinoza, J. Butler, J. Fishkin, R. Hornung, and B. Tromberg. 2001. Noninvasive functional optical spectroscopy of human breast tissue. *Proc Natl Acad Sci USA*, 98:4420-4425.

Sinichkin, Y. P., S. P. Uts, and E. Pilipenko. 1996. Spectroscopy of Human Skin *in vivo*: 1. Reflection Spectra. *Optics and Spectroscopy*, 80:228-234.

Sobol, I. 1975. The Monte Carlo method Moscow: Mir Publishers.

Sodhi, A., S. Montaner, V. Patel, M. Zohar, C. Bais, E. A. Mesri, and J. S. Gutkind. 2000. The Kaposi's sarcoma-associated herpes virus G protein-coupled receptor up-regulates vascular endothelial growth factor expression and secretion through mitogen-activated protein kinase and p38 pathways acting on hypoxia-inducible factor 1alpha. *Cancer Res*, 60:4873-4880.

Sorensen, J., M. Bengtsson, E. L. Malmqvist, G. Nilsson, and F. Sjoberg. 1996. Laser Doppler perfusion imager (LDPI)--for the assessment of skin blood flow changes following sympathetic blocks. *Acta Anaesthesiol Scand*, 40:1145-1148.

Spearman, C. 1904. The proof and measurement of association between two things. *American Journal of Psychology*, 15:72-101.

Stam, J. 2001. An illumination model for a skin layer bounded by rough surfaces. In *12th Eurographics Rendering Workshop*, 39-52.

Stamatas, G., M. Southall, and N. Kollias. 2006. In vivo monitoring of cutaneous edema using spectral imaging in the visible and near infrared. *J Invest Dermatol*, 126:1753-1760.

Stamnes, K. and P. Conklin. 1984. A new multi-layer discrete ordinate approach to radiative transfer in vertically inhomogeneous atmospheres. *J Quant Spectrosc Radiat Transfer*, 31:273-282.

Stoner, H. B., P. Barker, G. S. Riding, D. E. Hazlehurst, L. Taylor, and R. W. Marcuson. 1991. Relationships between skin temperature and perfusion in the arm and leg. *Clin Physiol*, 11:27-40.

Stranc, M. F., M. G. Sowa, B. Abdulrauf, and H. H. Mantsch. 1998. Assessment of tissue viability using near-infrared spectroscopy. *British Journal of Plastic Surgery*, 51:210-217.

Svaasand, L. O., L. T. Norvang, E. J. Fiskerstrand, E. K. S. Stopps, M. W. Berns, and J. S. Nelson. 1995. Tissue Parameters Determining the Visual Appearance of Normal Skin and Port-wine Stains. *Lasers in Medical Science*, 10:55-65.

Svanberg, K., I. Wang, S. Colleen, I. Idvall, C. Ingvar, R. Rydell, D. Jocham, H. Diddens, S. Bown, G. Gregory, S. Montán, S. Andersson-Engels, and S. Svanberg. 1998. Clinical multi-colour fluorescence imaging of malignant tumours--initial experience. *Acta Radiol*, 39:2-9.

Takatani, S. and J. Ling. 1994. Optical oximetry sensors for whole blood and tissue. *IEEE Eng Med Biol Mag*, 3:347-357.

Taylor, D. and S. Simonson. 1996. Use of near-infrared spectroscopy to monitor tissue oxygenation. *New Horiz*, 4:420-425.

Taylor, J., P. Tofts, and R. Port. 1999. MR Imaging of Tumor Microcirculation: Promise for the New Millenium. *J Magn Reson Imaging*, 10:903-907.

Thomson, M. L. 1955. Relative efficiency of pigment and horny layer thickness in protecting the skin of Europeans and Africans against solar ultraviolet radiation. *J Physiol*, 127:236-246.

Tomatis, S., M. Carrara, A. Bono, C. Bartoli, M. Lualdi, G. Tragni, A. Colombo, and R. Marchesini. 2005. Automated melanoma detection with a novel multispectral imaging system: results of a prospective study. *Phys Med Biol*, 50:1675-1687.

Ünver, N., P. Freyschmidt-Paul, S. Hörster, H. Wenck, F. Stäb, T. Blatt, and H. Elsässer. 2006. Alterations in the epidermal-dermal melanin axis and factor XIIIa melanophages in senile lentigo and ageing skin *Br J Dermatol*, 155:119-128.

Urso, P., M. Lualdi, A. Colombo, M. Carrara, S. Tomatis, and R. Marchesini. 2007. Skin and cutaneous melanocytic lesion simulation in biomedical optics with multilayered phantoms *Phys Med Biol*, 52:N229-239.

Usuki, K., T. Kanekura, K. Aradono, and T. Kanzaki. 1998. Effects of nicotine on peripheral cutaneous blood flow and skin temperature. *J Dermatol Sci*, 16:173-181.

van der Zee, P., M. Cope, S. R. Arridge, M. Essenpreis, L. A. Potter, A. D. Edwards, J. S. Wyatt, D. C. McCormick, S. C. Roth, E. O. R. Reynolds, and D. T. Delpy. 1992. Experimentally measured optical pathlengths for the adult head, calf and forearm and the head of the newborn infant as a function of inter optode spacing. New York: Plenum Press.

van Gemert, M. J. C. and J. P. H. Henning. 1981. A Model Approach to Laser Coagulation of Dermal Vascular Lesions. *Arch Dermatol Res*, 270:429-439.

Van Gemert, M. J. C., S. L. Jacques, H. J. C. M. Sterenberg, and W. M. Star. 1989. Skin Optics. *IEEE Trans*, 36:1146.

Verstraete, K., Y. De Deene, and H. Roels. 1994. Benign and Malignant Musculoskeletal Lesions: Dynamic Contrast-enhanced MR Imaging - Parametric "First-pass" Imaging Depict Tissue Vascularization and Perfusion. *Radiology*, 192:835-843.

Viator, J., J. Komadina, L. Svaasand, G. Aguilar, B. Choi, and J. S. Nelson. 2004. A Comparative Study of Photoacoustic and Reflectance Methods for Determination of Epidermal Melanin Content. *J Investigative Dermatology*, 122:1432-1439.

Vogel, A., V. Chernomordik, J. Riley, M. Hassan, F. Amyot, B. Dasgeb, S. Demos, R. Pursley, R. Little, R. Yarchoan, Y. Tao, and A. Gandjbakhche. 2007. Using Non-Invasive Multi-Spectral Imaging to Quantitatively Assess Tissue Vasculature. *Journal of Biomedical Optics*, 12:051604.

Wagnieres, G., S. Cheng, M. Zellweger, N. Utke, D. Braichotte, J. P. Ballini, and H. van den Bergh. 1997. An optical phantom with tissue-like properties in the visible for use in PDT and fluorescence spectroscopy. *Phy Med Biol*, 42:1415-1426.

Wan, S., R. R. Anderson, and J. Parrish. 1981. Analytical Modeling for the Optical Properties of the Skin with *In Vitro* and *In Vivo* Applications. *Photochem Photobiol*, 34:493-499.

Wang, L., S. Jacques, and L. Zheng. 1995. MCML--Monte Carlo modeling of light transport in multi-layered tissues. *Comput Methods Programs Biomed*, 47:131-146.

Ward, K., R. Ivatury, R. Barbee, J. Terner, R. Pittman, I. Fioho, and B. Spiess. 2006. Near infrared spectroscopy for evaluation of the trauma patient: a technology review. *Resuscitation*, 68:27-44.

Wardell, K., A. Jakobsson, and G. E. Nilsson. 1993. Laser Doppler perfusion imaging by dynamic light scattering. *IEEE Trans Biomed Eng*, 40:309-316.

Weigand, D. A., C. Haygood, and J. R. Gaylor. 1974. Cell layers and density of negro and caucasian stratum corneum. *J Investigative Dermatology*, 62:563-568.

Westland, S. and C. Ripamonti. 2004. Computational colour science using MATLAB West Sussex: John Wiley & Sons.

Wilcoxon, F. 1945. Individual comparisons by ranking methods. *Biometrics*, 1:80-83.

Williams, I., A. Mortimer, and C. McCollum. 1996. Recent developments in cerebral monitoring--near-infrared light spectroscopy. *Eur J Vasc Endovasc Surg*, 12:263-271.

Witt, A. 1977. Multiple scattering in reflection nebulae: I A Monte Carlo approach *Astrophys J*, 35:S1-S6.

Wyatt, J. S., M. Cope, D. T. Delpy, P. van der Zee, S. Arridge, A. D. Edwards, and E. O. R. Reynolds. 1990. Measurement of Optical Path Length for Cerebral Near-Infrared Spectroscopy in Newborn Infants. *Dev Neurosci*, 12:140-144.

Wyszecki, G. and W. Stiles. 1967. Color science: concepts and methods, quantitative data and formulas. New York: John Wiley & Sons.

Yarchoan, R. 1999a. Therapy for Kaposi's sarcoma: recent advances and experimental approaches. *J Acquir Immune Defic Syndr*, 21:S66-73.

Yarchoan, R. 1999b. Therapy for Kaposi's sarcoma: recent advances and experimental approaches. *J Acquir Immune Defic Syndr*, 21 Suppl 1:S66-73.

Zhang, R., W. Verkruysse, B. Choi, J. Viator, B. Jung, L. O. Svaasand, G. Aguilar, and J. S. Nelson. 2005. Determination of human skin optical properties from spectrophotometric measurements based on optimization by genetic algorithms. *J Biomed Opt*, 10:024030.

Zonios, G., L. T. Perelman, V. Backman, R. Mancharan, M. Fitzmaurice, J. Van Dam, and M. S. Feld. 1999. Diffuse reflectance spectroscopy of human adenomatous colon polyps *in vivo*. *Appl Opt*, 38:6628-6637.

Zonios, G. I., R. M. Cothren, J. T. Arendt, J. Wu, J. Van Dam, J. M. Crawford, R. Manoharan, and M. S. Feld. 1996. Morphological model of human colon tissue fluorescence. *IEEE Trans Biomed Eng*, 43:113-122.